Towards Quantum Simulations with Strontium in Cavity-enhanced Optical Lattices

Ji hyun (Annie) Park

München 2021

Towards Quantum Simulations with Strontium in Cavity-enhanced Optical Lattices

Dissertation an der Fakultät für Physik
Ludwig-Maximilians-Universität München

vorgelegt von

Ji hyun (Annie) Park

geboren in Seoul, Korea

München, den 9. November 2021

Tag der mündlichen Prüfung: 21. Dec 2021

Erstgutachter: Prof. Immanuel Bloch

Zweitgutachter: Prof. Thomas Udem

Weitere Prüfungskommissionsmitglieder: Prof. Thomas Birner, Prof. Stefan Filipp

Zusammenfassung

Eine Vielzahl der modernen Quantentechnologien basieren auf der Wechselwirkung zwischen Licht und Atomen. Durch die Kombination grundlegender Werkzeuge wie Laserkühlung und optische Dipolfallen haben diese Technologien den Punkt erreicht, an dem einzelne Atome gefangen werden und in hoch kontrollierter Weise miteinander wechselwirken können. Ein wichtiges Beispiel ist das optische Gitter, in dem sich durch Interferenz von Laserstrahlen ein Potential bildet, das viele Atome in einer regelmäßigen Anordnung einfängt. Die gefangenen Atome können gleichzeitig angesprochen werden, was in Quantenmetrologie zur Anwendung kommt. Dabei werden optische Gitter für die Realisierung der präzisesten Atomuhren verwendet. In der analogen Quantensimulation ahmen Atome in optischen Gittern Elektronen in kondensierter Materie nach. Inspiriert durch den Erfolg dieser Anwendungen wurden viele Vorschläge für weitere Verwendungen optischer Gitter gemacht. Beispiele sind die Quantensimulation verschiedener physikalischer Systeme in Nanophotonik oder Quantenchemie und für skalierbare Quantencomputer. Um diese spannenden Vorschläge zu realisieren, sind jedoch eine Reihe neuer Werkzeuge und technischer Fortschritte notwendig.

Diese Arbeit beschreibt den Aufbau eines analogen Quantensimulators basierend auf ultrakalten Strontium (Sr) Atomen, die in optischen Gittern gefangen sind. Diese Erdalkaliatome haben einzigartige Vorteile für die Quantensimulation. Der erste Vorteil von Sr ist seine heliumähnliche Struktur der Elektronen mit vielfältigen elektronischen Übergängen, die sowohl breit als auch schmal sein können. Wir demonstrieren ein verbessertes Schema zur Laserkühlung basierend auf diesen beiden Arten von Übergängen. Mit unserem Schema erzeugen wir magnetooptische Fallen für bosonische und fermionische Isotope von Sr mit hohen Phasenraumdichten. Unsere Methode ist einfach zu implementieren und schneller sowie auch robuster als herkömmliche Kühlmethoden, was zu kürzeren Präparationszeiten führt. Der zweite Vorteil von Sr ist die Existenz eines doppelt verbotenen Uhrenübergangs zwischen dem Singulett-Grundzustand und einem metastabilen Triplettzustand, den sogenannten Uhrenzuständen. Im Gegensatz zu Hyperfeinzuständen, die in Atomuhren auf Basis von Alkaliatomen verwendet werden, können diese Uhrenzustände selektiv bei sogenannten Tune-Out-Wellenlängen gefangen werden, bei denen die beiden Zustände stark unabhängige optische Potentiale erfahren. Mit einer neuartigen Methode bestimmen wir präzise die Tune-Out-Wellenlänge für den Sr-Grundzustand und zeigen eine Unterdrückung des Grundzustandsgitterpotentials um fast vier Größenordnungen gegenüber dem Potential des angeregten Zustands. Wir verwenden dieses zustandsabhängige Gitter auch, um die Lebensdauer angeregter Zustände genau zu messen und große Diskrepanzen in den Atomdaten aufzudecken, die verwendet werden, um den größten systematischen Effekt optischer Sr-Gitteruhren zu kalibrieren.

Neben der Nutzung der einzigartigen Eigenschaften von Strontium demonstrieren wir auch eine neue Architektur basierend auf optischen Resonatoren zur Vergrößerung zweidimensionaler optischer Gitter. Bei herkömmlichen Aufbauten mit Freistrahloptik ist die

Anzahl der Plätze in einem optischen Gitter durch die verfügbare Laserleistung begrenzt. Die endliche radiale Ausdehnung des Strahls führt zu einer Variation der Gittertiefe weg von der Strahlmitte. Um diese Einschränkung zu überwinden, haben wir eine neuartige Architektur entwickelt, bei der die Laserleistung in zwei orthogonalen Gitterrichtungen durch die Verwendung optischer Resonatoren verstärkt wird. Diese Verstärkung führt zu einer um eine Größenordnung größeren Anzahl von nutzbaren Gitterplätzen im Vergleich zu Freistrahlgittern. Entscheidend ist, dass diese Verstärkung bei jeder gewünschten Wellenlänge erfolgen kann, einschließlich der Sr Tune-Out-Wellenlänge, bei der die Laserleistung besonders begrenzt ist. Wir charakterisieren das durch den Resonator verstärkte Gitter mit hochauflösender Uhrenspektroskopie, um die Einhüllende des Gitterpotentials sowie die Probentemperatur lokal zu messen. Auf diese Weise sind wir in der Lage, die Gittertiefe und -homogenität zu charakterisieren, aber auch Grundband- und Gitterlebensdauern zu messen und zu zeigen, dass sie mit den Lebensdauern in Freistrahlgittern vergleichbar sind.

Insgesamt ist das in dieser Dissertation beschriebene Experiment eines der ersten Experimente weltweit, das darauf abzielt, die besonderen Eigenschaften von Sr für optische gitterbasierte Quantensimulatoren zu nutzen. Über unseren spezifischen Anwendungsfall hinaus glauben wir, dass die von uns entwickelten Werkzeuge einen breiten Einfluss auf die Quantenmetrologie, Simulation und Quantencomputer mit neutralen Atomen in optischen Gittern haben.

Abstract

The interactions between light and atoms form the basis for a wide variety of modern quantum technologies. By combining fundamental tools such as laser cooling and optical dipole traps, these technologies have reached the point where individual atoms can be captured and made to interact with each other in a highly controllable manner. A key example is the optical lattice, in which laser beams interfere to form a potential that traps many atoms in a regular array. These atoms can be simultaneously interrogated, leading to applications in quantum metrology, where optical lattices are used to realize the most accurate atomic clocks, and analog quantum simulation, where atoms in the lattice mimic electrons in condensed matter systems. Inspired by the success of these applications, many proposals for further applications of optical lattices have been made, such as for quantum simulation of different physical systems including nanophotonics and quantum chemistry, and for scalable quantum computation. However, to realize these exciting proposals, a number of new tools and technical advancements are necessary.

This thesis describes the construction of an analog quantum simulator based on ultracold strontium (Sr) atoms trapped in optical lattices. These alkali earth atoms have unique advantages for quantum simulation. The first advantage of Sr is its helium-like electronic structure with a diverse set of electronic transitions, both broad and narrow. We demonstrate an improved laser cooling scheme based on these two kinds of transitions. With our scheme, we create magneto-optical traps for bosonic and fermionic isotopes of Sr with high phase-space densities. Our method is simple to implement and is faster and more robust than traditional cooling methods, resulting in reduced sample preparation times. The second advantage of Sr is the existence of a doubly-forbidden clock transition between the singlet ground state and a metastable triplet state called the clock states. As opposed to hyperfine states that are used in atomic clocks based on alkali atoms, these clock states can be selectively trapped at so-called tune-out wavelengths where the two states experience highly independent optical potentials. Using a novel method, we precisely determine the tune-out wavelength for the Sr ground state and demonstrate a surpression of the ground state lattice potential by almost four orders of magnitude compared to the excited state potential. We also use this state-dependent lattice to accurately measure excitated state lifetimes, revealing large discrepancies in the atomic data used to calibrate the largest systematic effect of Sr optical lattice clocks.

Besides leveraging the unique properties of strontium, we also demonstrate a new cavity-based architecture for scaling up two-dimensional optical lattices. In conventional free-space setups, the number of sites in an optical lattice is limited by the available laser power, since the finite transverse extent of the beam induces a variation in the lattice depth away from the beam center. To overcome this limitation, we developed a novel architecture where laser power is amplified in two orthogonal lattice directions using optical cavities. This amplification results in an order of magnitude larger number of usable lattice sites compared to free-space lattices. Crucially, this amplification can occur at any

desired wavelength, including the Sr tuneout wavelength where laser power is especially limited. We characterize the cavity-enhanced lattice using high resolution clock spectroscopy to locally measure the lattice potential envelope and the sample temperature. In this way, we are able to characterize the lattice depth and homogeneity, and also measure ground-band and lattice lifetimes and show that they are comparable to lifetimes in free-space lattices.

Overall, the experiment described in this thesis is one of the first experiments worldwide aiming to take advantage of the special properties of Sr for optical lattice-based quantum simulators. Beyond our specific use case, we believe that the tools that we will have developed have broad impact on quantum metrology, simulation, and computation with neutral atoms in optical lattices.

Contents

List of Tables

List of Figures

Chapter 1

Introduction

Optical forces from laser light are a foundational technology for modern quantum science and are used for quantum simulation [1], quantum computation [2], and metrology [3, 4]. These applications use two different types of forces that laser light exerts on neutral atoms: a dissipative scattering force and a conservative dipole force. The former can be applied to cool atoms, which enhances the wave-like behavior of these atoms as their thermal de-Broglie wavelength becomes comparable to the inter-particle distances among the atoms. This cooling has been used as the first step in the creation [5, 6] of Bose-Einstein condensates (BECs), quantum mechanical bosonic gases in which the atoms macroscopically occupy the lowest quantum state. Once the atoms are cooled, they can also be trapped and stored for a long time in an optical trap created by the conservative dipole force. When such traps make use of interference between multiple laser beams, they create conservative potential landscapes with a well-defined periodicity, forming artificial crystals called optical lattices [7]. These lattices can be viewed as arrays of nearly identical microtraps that can hold ultracold atoms, and serve as an ideal platform for neutral atom-based quantum technologies.

When the lattices are loaded with ultracold atoms, the individual atoms on a given site interact, and lowering the laser intensity allows quantum tunneling between neighboring sites. Such systems naturally model real materials where electrons interact and tunnel in crystal lattices, capturing many important condensed matter models such as the Hubbard model [8, 1]. The onsite-interaction and tunneling parameters are highly controllable in these systems and either bosonic or fermionic atoms can be used, allowing the observation of different quantum many-body phenomena arising due to the particle statistics. The first landmark experiment [9] was the observation of a quantum phase transition of bosonic particles from a strongly interacting regime, where atoms arrange themselves so that a single atom occupies a lattice site, to a weakly interacting regime, where each atom is spread out over many sites. This phase transition is called the Mott insulator to superfluid transition, known to be relevant for the phase diagram of liquid helium, and was observed by tuning the ratio of tunneling and on-site interactions of a ^{87}Rb BEC loaded into a three-dimensional optical lattice. Moreover, subsequent experiments demonstrating fermionic Mott insulators [10, 11] and the detection of antiferromagnetic spin correlations [12, 13] have made important steps towards understanding high-temperature superconductivity, a long-standing problem in condensed-matter physics [14].

The aforementioned successes in cooling, trapping, and engineering complex many-body states using neutral atoms in optical lattices have encouraged researchers to envision expanding the scope of these platforms for scalable quantum computation [15, 16, 2] and quantum simulations of other physical systems such as quantum emitters in nanophotonics [17–20]. For all these applications, precise control over at least two different internal states, either electronic, hyperfine, or even nuclear spin states, is essential. In quantum computing, these two states would be denoted by $|0\rangle$ and $|1\rangle$ in analogy to classical computing and together they would form the basic unit of computation, the qubit. In nanophotonics, the aforementioned states would simulate the behavior of a quantum emitter and a photon. Early attempts at realizing this precise control used alkali atoms such as rubidium, due to their relatively simple electronic structure. In such atoms, electronic excited states have short lifetimes of tens of nanoseconds, which is too short for many quantum applications, so an experimentally relevant two-level system needs to be based on the hyperfine states of an electronic ground state. This limitation hinders the flexibility of independent control over the two states because both states interact with laser light in a similar fashion and also result in unavoidable decoherence effects [21]. One possible proposal to solve this problem is replacing alkali with alkaline-earth(-like) atoms that have two electrons in their outer shell and use their electronic *clock* states as the required two-level system.

Because of their two valence electrons, alkali-earth(-like) atoms such as strontium and ytterbium have an exceptionally narrow optical transition, with linewidths on the order of the millihertz. The electronic ground (g) and long-lived excited (e) states connected by this narrow *clock* transition are called clock states due to their wide use in optical clocks [22, 3, 23]. In particular, optical lattice clocks based on strontium have reached state-of-the-art frequency fractional instability below 10^{-18} by averaging the signal from thousands of atoms loaded in optical lattices for one hour [24]. In these experiments, the optical lattices operate at a so-called magic wavelength [25, 26] where both clock states experience identical light potentials. Therefore, the energy differences between the clock states are unchanged regardless of the variation of lattice depth, allowing homogeneous interrogation of atoms throughout the entire lattice. This trick serves as an ideal example where the internal electronic degrees of freedom are completely decoupled from the external motional degrees of freedom. Magic wavelengths also exist for the hyperfine states of alkali metal atoms; however, using such lattices results in high scattering rates and low coherence times since the magic wavelength typically lies between transitions to excited fine structure energy levels. An additional desirable feature of strontium atoms is the ability to create highly state-dependent optical lattices specific to the two clock states. This unique feature has been unexplored experimentally before the work described in this thesis despite being highlighted in many recent theoretical proposals [21, 27–29]. In particular, these two states can be trapped completely independently by optical traps at so-called tune-out wavelengths [30], where one of the states experiences a vanishing optical trap potential. This idea has made the clock states the ideal optical qubits or resources for entangling gates for scalable quantum information processing [21, 27–

29] and a resource for quantum simulations of nanophotonics [17, 31–33] and quantum chemistry [34] that require high-fidelity state-dependent control.

Beyond the advantages from the clock states, strontium atoms' rich electronic state structure consisting of singlet and triplet manifolds give rise to other optical transitions with linewidths in the megahertz and kilohertz regimes. These transitions together can be used to develop efficient laser-cooling schemes. The broad transition is used to efficiently cool initially hot atoms with its large scattering force, and the narrow-line is subsequently used to cool the atoms close to the quantum mechanical limit of $230\ \mathrm{nK}$. The existence of the narrow line allows the creation of a atomic cloud with a high phase-space-density of 10^{-2} [35] which is three orders of magnitude higher than in a conventional magneto-optical trap (MOT) using alkali atoms [36]. This low temperature reduces the duration of subsequent evaporative cooling [37] (a cooling technique that discards the hot atoms), and even allows all-optical cooling to a degenerate quantum gas when loaded in a dipole trap [38]. All the above advantages reduce the sample preparation times [37].

Combining the aforementioned advantages of strontium, this thesis reports on the construction of a new quantum simulator with a high repetition rate that employs highly state-dependent lattices for the strontium clock states. We have (1) improved a narrow-line laser cooling technique for the fast and robust cooling of strontium atoms [39] (2) measured the tune-out wavelength using a new robust spectroscopic method, and (3) demonstrated a state-dependent lattice at this wavelength that traps the excited clock state with a high contrast ratio and long lifetime [40]. We demonstrate that this state-dependent lattice can suppress the lattice depth of g more than 4 orders of magnitude compared to that of e given that the laser's frequency can be stabilized within $10\ \mathrm{MHz}$. In addition, we use the precisely measured tune-out wavelength to determine atomic lifetimes. In doing so, we find large discrepancies to the atomic data that are used to calibrate systematic effects in Sr optical lattice clocks, thus calling for a thorough experimental reinvestigation of the relevant atomic lifetimes.

Apart from employing the distinct properties of strontium atoms, we also tackle a long-standing problem in neutral-atom quantum technology in general: increasing the number of usable optical lattice sites. Since laser beams create optical lattices with finite laser power, the lattice sites are no longer identical on length scales that are comparable to the finite transverse extent of the beams because of the variation in lattice potential depth. This inhomogeneity limits the number of usable lattice sites. Our solution uses optical cavities to create lattice beams with enhanced optical power and large mode diameters. With this solution, we increase the number of available lattice sites by more than an order of magnitude compared to state-of-the-art free-space lattices [41, 42]. Currently, most far-off-resonant optical lattices are created using high-power and low-noise Nd:YAG lasers. Since these lasers are only available at infrared wavelengths, our solution opens new possibilities to create large and deep lattices at any desired wavelength supported by the cavity mirror coatings. In short, our ultracold strontium machine combines clock

technology, state-dependent control, and cavity-enhanced optical lattices. Moreover, the apparatus is designed for the near-future implementation of quantum gas microscopy for single-site imaging and addressing of strontium atoms on the clock transition.

The tools developed in this thesis open up possibilities for quantum simulations of strongly coupled light matter interfaces [17, 31–33]. For these simulations, coherent tunneling over hundreds of lattice sites is desirable [32] which necessitates large two-dimensional optical lattices. These simulations also require the creation of state-dependent lattices that trap the clock states with a high contrast ratio and long lifetime, which is challenging due to the particularly limited laser power at the necessary wavelengths. We solve both challenges using cavity-enhanced optical lattices. Beyond this specific application, our cavity solves the problem of scaling atom arrays for optical lattice clocks and quantum computers to tens of thousands of qubits without any changes to the underlying architecture.

The thesis is structured as follows:

- Chapter 2 provides a brief summary of the basics of light-matter interactions, strontium energy levels, and the working principle of state-dependent lattices, cavity-enhanced lattices, and quantum gas microscopes.
- Chapter 3 describes the experimental setup used for laser-cooling strontium atoms and our improved narrow-line laser cooling technique.
- Chapter 4 contains the measurement of the ground state $^1S_0$ tune-out wavelength and demonstration of state-dependent lattices of strontium clock states.
- Chapter 5 focuses on the experimental implementation of monolithic crossed cavities and their characterization.
- Chapter 6 provides the summary and future directions of the work.

The results of the above work have been published in:

4. **A. J. Park**, J. Trautmann, N. Šantić, V. Klüsener, A. Heinz, I. Bloch, and S. Blatt. Cavity-enhanced optical lattices for scaling neutral atom quantum technologies, arXiv:2110.08073, (2021) [42].

3. A. Heinz, J. Trautmann, N. Šantić, **A. J. Park**, I. Bloch, and S. Blatt. Crossed optical cavities with large mode diameters, Optics letters **46**, 250, (2021) [41].

2. **A. Heinz***, **A. J. Park***, N. Šantić, J. Trautmann, S. G. Porsev, M. S. Safronova, I. Bloch, and S. Blatt. State-dependent optical lattices for the strontium optical qubit, Phys. Rev. Lett. **124,** 203201 (2020) [40].

   *These authors contributed equally to this manuscript.

1. S. Snigirev, **A. J. Park**, A. Heinz, I. Bloch, and S. Blatt. Fast and dense magneto-optical traps for strontium, Phys. Rev. A **99,** 063421 (2019) [39].

Chapter 3 contains passages from 1 with permission from the American Physical Society ©2019. Chapter 4 contains passages from 2 with permission from the American Physical Society ©2020.

Chapter 2

Optical toolbox for the new ultracold strontium machine

In this chapter, we introduce the basic tools that we use to build our new ultracold strontium machine. The toolbox that we develop fundamentally relies on the interaction of light with individual atoms (Section 2.1). When these interactions are combined with the distinct properties of strontium atoms (Section 2.2), efficient laser cooling, different state-dependent lattices, and optical qubits with a long lifetime can be realized. By trapping strontium atoms in state-dependent lattices (Section 2.3) created in optical cavities with a large power enhancement and mode diameter (Section 2.5), we solve the limited laser power issue and create an order of magnitude larger optical lattices. By combining all these tools, we open up new possibilities for quantum simulations of nanophotonics and quantum chemistry and for engineering controlled collisional phase gates (Section 2.7).

2.1 Light-atom interaction

We briefly present the basic light-matter interactions and define symbols and terminologies used throughout this thesis. Here, we consider the simplest case of a two-level atom with internal ground (g) and excited (e) states separated by energy $\hbar\omega_{eg}$ and its interaction with a monochromatic electromagnetic field. We treat the light field classically using the form,

$$\boldsymbol{E}(r,z,t) = \frac{1}{2}(E(r,z)\exp(-i\omega t)\hat{\mathbf{e}} + c.c.), \tag{2.1}$$

with an optical angular frequency $\omega = kc$, where $k = 2\pi/\lambda$ is the wavenumber for wavelength λ, c is the speed of light, and $\hat{\mathbf{e}}$ is the polarization unit vector. This semi-classical picture is sufficient to understand most of the atom-light interactions discussed in this thesis; however, we will later extend these concepts to multi-level systems focusing on the strontium atom's energy level structure.

Radiation pressure force

The topic of radiation force from a laser beam is discussed in many standard textbooks. Here, we closely follow Ref. [43] and summarize their formalism. When a stationary atom experiences an electromagnetic field of the form Eqn. (2.1), it absorbs and spontaneously re-emits photons, which results in a dissipative force due to the momentum transfer of

the absorbed and spontaneously emitted photons. This scattering force is given by

$$\boldsymbol{F}_{\text{sc}} = \frac{\Gamma}{2}\frac{\hbar\boldsymbol{k}s_0}{1+s_0+(2\Delta/\Gamma)^2}, \tag{2.2}$$

where $\hbar\boldsymbol{k}$ is the momentum of the photon with a wavevector $\boldsymbol{k} = 2\pi\hat{\boldsymbol{k}}/\lambda$ where $\hbar = 2\pi h$ is the reduced Planck constant. Here, $\Delta = \omega - \omega_{eg}$ is the detuning of the laser's angular frequency ω from the atomic resonance frequency ω_{eg}, Γ is the decay rate of the atomic transition, and s_0 is the saturation parameter defined as $s_0 = I/I_{\text{sat}}$, where I is the light intensity, and the saturation intensity is $\pi h\Gamma c/(3\lambda^3)$. This force constitutes the basis of laser cooling.

To slow down an atom moving with velocity $\boldsymbol{v}$, light fields from two opposite directions can be applied to the atom to generate scattering forces in two opposite directions:

$$\boldsymbol{F}_{\text{sc}} = \frac{\hbar\boldsymbol{k}\Gamma}{2}\left[\frac{s_0}{1+s_0+[2(\Delta-\boldsymbol{k}\cdot\boldsymbol{v})/\Gamma]^2} - \frac{s_0}{1+s_0+[2(\Delta+\boldsymbol{k}\cdot\boldsymbol{v})/\Gamma]^2}\right] \approx -\beta\boldsymbol{v} \tag{2.3}$$

where $\boldsymbol{k}\cdot\boldsymbol{v}$ is the Doppler shift. In the last step of Eqn. (2.3), we have made a linear approximation for small velocities, showing that the force acts opposite to the atom's motion and thereby reduces the atom's kinetic energy. However, since this approximation is valid only for small velocities, the cooling efficiency is limited to a range of velocities that is bounded by the capture velocity $v_{\text{cap}} \sim \Delta/k$ (which occurs where the magnitude of the force is maximum). This concept of capture velocity is important for cooling strontium atoms and partly leads to employing different cooling schemes in sequence. The cooling scheme described in Eqn. (2.3) is called optical molasses and can be extended to two (2D) and three (3D) dimensions, thus allowing laser-cooling in all spatial directions.

The above cooling technique can also be extended to produce a position-dependent part of the force, thereby trapping the atoms and cooling them. In this case, we consider a two-level atom with a total angular momentum of $J_g = 0$ and $J_e = 1$ for g and e, respectively, placed in a linear magnetic field gradient b as well as the two light fields from opposite directions. This linear gradient splits the excited states into three Zeeman substates $m_{J_e} = 0, \pm 1$ that are separated by the energy difference $\Delta E = \mu_B g_{J_e} m_{J_e} b z'$, where $\mu_B \simeq 1.4\ \text{MHz/G}$ is the Bohr magneton, g_{J_e} is the Landé g-factor associated with J_e, and z' is the spatial coordinate along which the gradient is applied. When the two incident light beams have σ^- and σ^+ polarizations, these beams excite g to $m_{J_e} = -1$ and $m_{J_e} = +1$, respectively. In this scenario, the resonant conditions of the radiative force, which are $\Delta \pm \boldsymbol{k}\cdot\boldsymbol{v}$ in Eqn. (2.3), are modified to

$$\Delta \pm \boldsymbol{k}\cdot\boldsymbol{v} \pm \mu_B g_{J_e} m_{J_e} b z'/\hbar. \tag{2.4}$$

For this reason, the force gains a position-dependent part and enables trapping and cooling in all spatial directions when extended to three dimensions. This technique is called magneto-optical trap (MOT), which is the core step in preparing ultracold atoms. In ex-

periments, a magnetic gradient is produced by a quadrupole magnetic field created by a pair of anti-Helmholtz coils. At the center of the coil configuration, this magnetic field approximately produces a linear field gradient that is twice stronger in the axial direction compared to the transverse direction. For this reason, we will see in Section 2.2 that the atoms cooled and trapped by a MOT occupy an ellipsoidal region.

To understand the cooling limit of optical molasses, we need to consider the additional stochastic forces acting on the atoms caused by the spontaneous rescattering of photons into random directions. This undirected scattering leads to a random walk of atoms in momentum space, and consequently, heats the atoms. A limiting temperature is reached when this heating rate equals the cooling rate resulting in the Doppler temperature $T_D = \hbar\Gamma/(2k_B)$, where k_B is the Boltzmann constant. In this limit, cooling on a transition with larger Γ transfers a larger force, leading to more efficient cooling. However, large Γ also results in higher limiting temperatures. The second fundamental limit is given by the recoil temperature $T_R = \hbar^2k^2/(2k_Bm)$, which is set by the recoil energy $E_R = \hbar^2k^2/2m$ on an atom with mass m transferred by its last emitted photon. In most cases, the Doppler temperature limit is higher than the recoil limit, and other sub-Doppler cooling techniques [44–48] are employed to reach a temperature closer to the recoil limit. However, as will be shown later in Section 2.2, because of the transition's narrow linewidth, the second stage MOT of strontium atoms is limited by the recoil rather than the Doppler temperature, requiring quantum mechanical treatment to describe the cooling process [49]. Furthermore, in Chapter 3, we will present our modified narrow-line cooling technique based on adiabatic passage on the narrow transition that leads to fast and dense preparation of ultracold strontium atoms.

Far-off-resonant traps

In contrast to the dissipative force we discussed above, there is also a conservative force that gives rise to optical traps where atoms can be trapped for long times. Here, we closely follow the derivation presented in Ref. [50]. The light field induces a dipole moment d that oscillates at the same frequency as the light field, and the interaction between this induced dipole moment and the light field creates the conservative trap. This induced dipole moment is given by $\boldsymbol{d(r,t)} = 1/2(d(r)\exp(-i\omega t)\hat{\mathbf{e}} + c.c.)$ with the amplitude of the dipole moment $d(r,z) = \alpha(\omega)E(r,z)$ where $\alpha(\omega)$ is called the complex dynamic dipole polarizability. The time-averaged interaction potential V_{dip} of the induced dipole moment with the electric field E is

$$V_{\text{dip}}(r,z) = -\frac{1}{2}\langle \boldsymbol{d(r,t)} \cdot \boldsymbol{E(r,z,t)} \rangle = -\frac{1}{2\epsilon_0 c}\text{Re}[\alpha(\omega)]I(r,z), \tag{2.5}$$

where a factor 1/2 takes into account that the dipole moment is induced instead of being permanent, and we used $I(r,z) = c\epsilon_0|E(r,z)|^2/2$ in the last step, where ϵ_0 is the vacuum permittivity. Here, we note that the quickly oscillating terms at 2ω average out due to time averaging denoted by the angular brackets. This potential V_{dip} is called ac-Stark

shift and its spatial variation exerts a conservative force on the atom, which is given by $F_{\text{dip}}(r,z) = \nabla V_{\text{dip}}(r,z) = -\frac{1}{2\epsilon_0 c}\text{Re}[\alpha(\omega)]\nabla I(r,z)$. From the above expression, we can see that depending on the sign of $\text{Re}[\alpha(\omega)]$, the atom is either attracted to the maximum or minimum of $I(r,z)$.

As we have seen above, $\alpha(\omega)$ is central to characterizing an optical trap. Treating an atom as a Lorentz oscillator [50], $\alpha(\omega)$ is given by

$$\alpha(\omega) = 6\pi\epsilon_0 c^3 \frac{\Gamma}{\omega_{eg}^2(\omega_{eg}^2 - \omega^2 - i\Gamma\frac{\omega^3}{\omega_{eg}^2})}. \tag{2.6}$$

For a multi-level atom, the expression above needs to be summed over all dipole-allowed transitions connected to the state of the interest, and a full transition matrix between the involved states has to be considered. Therefore, the complex polarizability $\alpha(\omega)$ is both state- and laser polarization-dependent. In Chapter 4, we will decompose $\alpha(\omega)$ into a spherical tensor basis to understand the light- and atom-polarization dependence on $\alpha(\omega)$ better. Although Eqn. (2.6) only describes the simplest case, it still captures many important features of the polarizability. To look at these features more explicitly, let us expand and simplify Eqn. (2.6):

$$\begin{aligned}
\alpha(\omega) &= \frac{6\pi\epsilon_0 c^3\Gamma}{\omega_{eg}^2}\left[\frac{\omega_{eg}^2 - \omega^2}{(\omega_{eg}^2-\omega^2)^2 + (\Gamma\omega^3/\omega_{eg}^2)^2} + i\frac{\Gamma\omega^3/\omega_{eg}^2}{(\omega_{eg}^2-\omega^2)^2 + (\Gamma\omega^3/\omega_{eg}^2)^2}\right] \\
&\approx \frac{6\pi\epsilon_0 c^3\Gamma}{\omega_{eg}^2}\left[\frac{1}{(\omega_{eg}^2 - \omega^2)} + i\frac{\Gamma\omega^3/\omega_{eg}^2}{(\omega_{eg}^2-\omega^2)^2}\right] && (2.7) \\
&= \frac{6\pi\epsilon_0 c^3\Gamma}{\omega_{eg}^2}\left[\frac{1}{2\omega_{eg}}\left(\frac{1}{\omega_{eg}-\omega} + \frac{1}{\omega_{eg}+\omega}\right) + i\frac{\Gamma\omega^3}{4\omega_{eg}^4}\left(\frac{1}{\omega_{eg}-\omega} + \frac{1}{\omega_{eg}+\omega}\right)^2\right] && (2.8) \\
&\approx \frac{3\pi\epsilon_0 c^3\Gamma}{\omega_{eg}^3}\left[\frac{-1}{\Delta} + i\frac{\Gamma}{2\Delta^2}\right] && (2.9) \\
&= \text{Re}[\alpha(\omega)] - i\frac{\Gamma}{2\Delta}\text{Re}[\alpha(\omega)]. && (2.10)
\end{aligned}$$

In Eqn. (2.7), we have neglected the term $\Gamma\omega^3/\omega_{eg}^2$ in the denominators for simplicity, since $\Gamma \ll \omega_{eg}, \omega$. After expanding Eqn. (2.7), we obtain Eqn (2.8) which has the form that is most commonly found in the literature, including Ref. [50]. To get Eqn. (2.9), we make an additional rotating wave approximation, assuming that the laser is tuned close to resonance $|\Delta| = |\omega - \omega_{eg}| \ll \omega_{eg}$. In this case, we neglect the counter-rotating term and obtain $\omega/\omega_{eg} \approx 1$.

Using Eqn. (2.9), let us highlight important features of $\text{Re}[\alpha(\omega)]$ that $\propto V_{\text{dip}}$ (Eqn. (2.5)). First of all, the polarizability increases as the laser frequency ω is tuned closer the resonance frequency ω_{eg} ($\Delta \sim 0$) and when Γ is larger. This feature will become important later to get an intuitive picture of the polarizabilities of the strontium clock states. Sec-

ond, we can see that $\mathrm{Re}[\alpha(\omega)]$ is positive when the laser frequency is red-detuned ($\Delta < 0$) from the resonance and negative for the blue-detuned case ($\Delta > 0$). This polarity leads to a red-detuned trap that attracts the atoms towards the maximum intensity, and a blue-detuned trap that repels the atoms away from the maximum. Although the behaviour of the real part of $\alpha(\omega)$ changes when many optical transitions contribute, the above statement generally holds near the resonance frequency. From these features, it may seem that detuning closer to the resonance is advantageous to make a deeper potential. However, traps close to resonance heat atoms due to a higher scattering rate Γ_{sc}, which is given by

$$\Gamma_{\mathrm{sc}} = -\frac{\mathrm{Im}[\alpha(\omega)]I(r,z)}{\hbar\epsilon_0 c} \tag{2.11}$$

$$\approx \frac{\Gamma}{\Delta}\frac{V_{\mathrm{dip}}(r,z)}{\hbar}. \tag{2.12}$$

In the last step, we used Eqn. (2.10) and Eqn. (2.5) to obtain Eqn. (2.12). Therefore, a trade-off between lattice depth and scattering rate has to be met for a given laser power. Due to its inverse scaling with detuning, the incoherent scattering in far-off resonant traps is highly suppressed, so these traps are widely used to store atoms at low temperatures. Thus, for most applications, this scattering is not the main decoherence mechanism, although exceptions exist, such as experiments that require preparing many-body states at very low energy [51, 52] scales or trapping atoms in extremely deep optical lattices [53]. In later sections, we will take a closer look at the polarizability of the ground and excited states of strontium atoms to engineer state-dependent lattices. By doing so, we will see that the simple relationship between Γ_{sc} and V_{dip} in Eqn. 2.12 does not hold anymore for a multi-level atom, i.e. even when V_{dip} is zero due to the vanishing $\mathrm{Re}[\alpha(\omega)]$, the atom can still scatter photons in the lattice due to the light intensity.

Dipole trap

Throughout this thesis, we will only consider red-detuned dipole traps. Therefore, this section summarizes the important trap parameters for the red detuned trap made with a laser beam with $E(r,z) = E_0\frac{w_0}{w(z)}\exp\left[-\frac{r^2}{w^2(z)} - i\left(kz + \frac{kr^2}{2R(z)} - \psi(z)\right)\right]$ where $w(z) = w_0\sqrt{1+z/z_R}$ is the $1/e^2$ beam waist with the Rayleigh range $z_R = \pi w_0^2/\lambda$ and a minimum beam waist w_0 at the focus $z = 0$, and r and z are the radial and axial coordinate, respectively. Moreover, $R(z) = z[1 + (z_R/z)^2]$ is the radius of curvature and $\psi(z) = \arctan(z/z_R)$ is the Guoy phase. Such a beam has a Gaussian intensity profile of

$$I(r,z) = \frac{E_0^2}{2c\epsilon_0}\frac{w_0^2}{w^2(z)}\exp\left(-\frac{2r^2}{w^2(z)}\right) = \frac{2P}{\pi w^2(z)}\exp\left(-\frac{2r^2}{w^2(z)}\right), \tag{2.13}$$

where $P = \frac{\pi w_0^2 I_0}{2}$ is the power of the beam with peak intensity $I_0 = E_0^2/(2c\epsilon_0)$. Such a trap forms a dipole trap that is cylindrically symmetric. Using Eqn. (2.5) and approximating

the trap potential at the center, we arrive at

$$V_{\text{dip}}(r,z) \approx \frac{\text{Re}(\alpha)P}{\pi c\epsilon_0 w_0^2}\left[1-2\left(\frac{r}{w_0}\right)^2-\left(\frac{z}{z_R}\right)^2\right]. \tag{2.14}$$

This above expression results in a harmonic trap with radial (ω_r) and axial trap (ω_t) frequencies are

$$\omega_r = \sqrt{\frac{4V_0}{mw_0^2}}, \qquad \omega_t = \sqrt{\frac{2V_0}{mz_R^2}}, \tag{2.15}$$

where $V_0 = \text{Re}(\alpha)P/(\pi c\epsilon_0 w_0^2)$ is the trap depth. In reality, gravity also plays a role. Therefore, the effect of gravity should be taken into account, which reduces the trap depth. In this thesis, we will make it clear by stating *gravity compensated* if the depth includes gravity.

Optical lattices

Here, we derive important trap parameters for optical lattices. For simplicity, we will first consider a plane wave of the form $E(r,z) = E_0\text{exp}(ikz)$ that is retro-reflected, giving rise to an intensity profile

$$I(x) = \frac{1}{2}c\epsilon_0|E_0\text{exp}(ikz) + E_0\text{exp}(-ikz)|^2 = 4I_0\text{cos}^2(kz). \tag{2.16}$$

Using Eqn. (2.5) once more, we see that such an intensity pattern creates an infinitely extended periodic potential with a periodicity of $\lambda/2$ with $V_0 = 2I_0\text{Re}[\alpha(\omega)]/(\epsilon_0 c)$. For a deep lattice, we can approximate each well as a harmonic trap potential and extract the lattice trap frequency

$$\omega_t = 2\pi\nu_t = \sqrt{\frac{2k^2}{m}V_0} = \omega_{\text{rec}}\sqrt{\frac{4V_0}{E_{\text{rec}}}}, \tag{2.17}$$

where $E_{\text{rec}} = \hbar\omega_{\text{rec}} = \hbar^2k^2/(2m) = h^2/(2m\lambda^2)$ is the lattice recoil energy given by the lattice wavelength λ.

As we have seen, a more realistic model for a laser beam is a fundamental transverse electromagnetic mode (TEM_{00}) with a Gaussian intensity profile which prevents the generation of an infinitely extended lattice. As we have seen in Eqn. (2.13) and Eqn. (2.14), the radial part of the intensity profile leads to a harmonic confinement of the form $m\omega^2r^2/2$ on top of the lattice. We will see in Section 2.5 that this harmonic confinement limits the number of usable lattice sites for both quantum simulators and optical lattice clocks.

2.1.1 Two level system - Optical qubit

We have seen how the laser force can be used to cool and trap atoms. Here, we want to focus on a coherent manipulation of the electronic states of an atom using a near resonant light field, which is the basis of how we drive the strontium clock states. We once again follow the discussion in Ref. [43] and consider the simplest case, a plane wave of the form $E(r,z) = E_0\exp(ikz)$. Neglecting spontaneous scattering, one can solve the time-dependent Schrödinger equation with the Hamiltonian of the form $\hbar\omega_{eg}\left|e\right\rangle\left\langle e\right| - \boldsymbol{d(r,t)\cdot E(r,z,t)}$ to calculate the time dynamics of g and e driven by near-resonant light. Assuming the atom is initialized in g, the above calculation results in an oscillatory behavior of the probability for finding the atom in e,

$$P_e(t) = \frac{\Omega^2}{\Omega_{\text{eff}}^2}\sin^2(\Omega_{\text{eff}}t/2). \tag{2.18}$$

Here, $\Omega = \mathbf{d}\cdot\mathbf{E}/\hbar$ is the Rabi frequency that characterizes the interaction strength and $\Omega_{\text{eff}} = \sqrt{|\Omega|^2 + \Delta^2}$ is the effective Rabi frequency. When the laser is resonant, $\Omega_{\text{eff}} = \Omega$ and the oscillation becomes the slowest. A frequent parameter used to characterize this interaction strength is $t_\pi = \pi/\Omega$ which is defined as the time required for the P_e to reach 1 under the resonant condition.

The more realistic picture including spontaneous emission which can be done by using a density matrix formalism and adding the decay due to spontaneous scattering Γ phenomenologically. This method results in two equations describing the dynamics of the ground (ρ_{gg}) and excited (ρ_{ee}) state populations and another two describing the coherences ρ_{ge} and ρ_{eg}:

$$\begin{aligned}
\frac{d\rho_{gg}}{dt} &= +\Gamma\rho_{ee} + \frac{i}{2}(\Omega^*\tilde{\rho}_{eg} - \Omega\tilde{\rho}_{ge}) \\
\frac{d\rho_{ee}}{dt} &= -\Gamma\rho_{ee} + \frac{i}{2}(\Omega\tilde{\rho}_{ge} - \Omega^*\tilde{\rho}_{eg}) \\
\frac{d\tilde{\rho}_{ge}}{dt} &= -\left(\frac{\Gamma}{2} + i\Delta\right)\tilde{\rho}_{ge} + \frac{i}{2}\Omega^*(\rho_{ee} - \rho_{gg}) \\
\frac{d\tilde{\rho}_{eg}}{dt} &= -\left(\frac{\Gamma}{2} - i\Delta\right)\tilde{\rho}_{eg} + \frac{i}{2}\Omega(\rho_{gg} - \rho_{ee})
\end{aligned} \tag{2.19}$$

where $\tilde{\rho}_{ij} \equiv \rho_{ij}\exp(-i\Delta t)$ and * denotes the complex conjugate. Other decoherence mechanisms due to elastic collisions, a finite laser linewidth, and Doppler effects can also be included phenomenologically.

Solving the steady state of Eqn. (2.19), one obtains a steady state excited state population of

$$\rho_{ee} = \frac{s_0/2}{1 + s_0 + (2\Delta/\Gamma)^2}. \tag{2.20}$$

When $s_0 \gg 1$, ρ_{ee} approaches 1/2 and the absorption spectrum obtains the power-broadened linewidth of the transition $\Gamma' = \Gamma\sqrt{1+s_0}$. Equation (2.19) brings us back to the radiation pressure force (Section 2.1) and reveals the origin of Eqn. (2.2). In steady state, the excitation and decay rates balance, and the resulting the total scattering rate $\Gamma_{sc} = \Gamma\rho_{ee}$. Then, the resulting force is simply the momentum per photon $\hbar k \times \Gamma_{sc}$.

When the effects of decoherence occur at slower timescales than the interaction dynamics, the population dynamics will resemble that of Eqn. (2.18). Therefore, the quality of Rabi oscillations provides a good indication of how well-decoupled a two-level system is from decoherence. In many cases, the spontaneous scattering fundamentally limits treating atomic states connected by an optical transition as an ideal two-level system or an optical qubit. However, this obstacle is removed for the strontium clock states which has an ultra-narrow linewidth Γ of $1.35(3)$ mHz [54] ($\tau \sim 150$ s). Despite this advantage, we will see later there are other decoherence mechanisms that hinder their quality as an optical qubit such as inelastic collisions. However, many of these obstacles can be removed by technical advances or by providing better experimental platforms for strontium. For instance, decoherence due to inelastic collisions can be solved by loading strontium atoms in a 3D optical lattice with an occupancy of a single atom per site.

2.2 Strontium

In this section, we highlight the distinct properties of strontium atoms and apply the basic light-atom interactions, discussed above, to strontium atoms. By doing so, we find that strontium offers distinct advantages for laser-cooling and engineering state-selective control. As we highlight these features, we will also provide more insight into our ultracold strontium machine.

				Scattering length a $[a_0]$			
Isotope	Abundance	Nuclear spin	Statistics	^{84}Sr	^{86}Sr	^{88}Sr	^{87}Sr
^{84}Sr	0.56 %	0	Bosonic	123			
^{86}Sr	9.86 %	0	Bosonic	32	800		
^{88}Sr	82.5 8%	0	Bosonic	1700	97	-2	
^{87}Sr	7.00 %	9/2	Fermionic	-57	162	55	96

Table 2.1 Basic properties of naturally occurring strontium isotopes. The ground state scattering length data is taken from Ref. [37].

Strontium is an alkaline earth metal and has four naturally occurring isotopes with different abundances as shown in Table 2.1. Of the four, three are bosonic isotopes with a nuclear spin of $I = 0$, and one is fermionic with a nuclear spin of $I = 9/2$. Looking at their electronic structures, strontium has two valence electrons that can form either a singlet or a triplet state as a pair, depending on the orientation of their spins. The electronic

ground state is the singlet state $^1S_0$ and is connected to the upper singlet $^1P_1$ and triplet excited states ^3P_J with $J = 0, 1, 2$ via dipole-allowed transitions as shown in Fig. 2.1 for ^{87}Sr. These transitions come with a variety of different transition strengths because the intercombination lines, i.e. the $^1S_0$-^3P_J transitions, are much weaker compared to the $^1S_0$-$^1P_1$ transition due to the selection rules. These lines are spin forbidden, and the $^1S_0$-$^3P_{0,2}$ transitions are additionally forbidden by the angular momentum selection rule. However, the LS coupling regime relaxes for many-electron atoms, allowing the $^1S_0$-$^3P_1$ transition to occur with a narrow linewidth. Moreover, hyperfine mixing in ^{87}Sr allows a direct single photon transition to $^3P_1$ from $^1S_0$, where this transition has a millihertz linewidth (a similar can occur in ^{88}Sr with an external magnetic field.) For this reason, the dipole-allowed transitions from $^1S_0$ feature linewidths in the megahertz (blue MOT), kilohertz (red MOT), and millihertz regimes (clock and slicing), as labeled in Fig. 2.1.

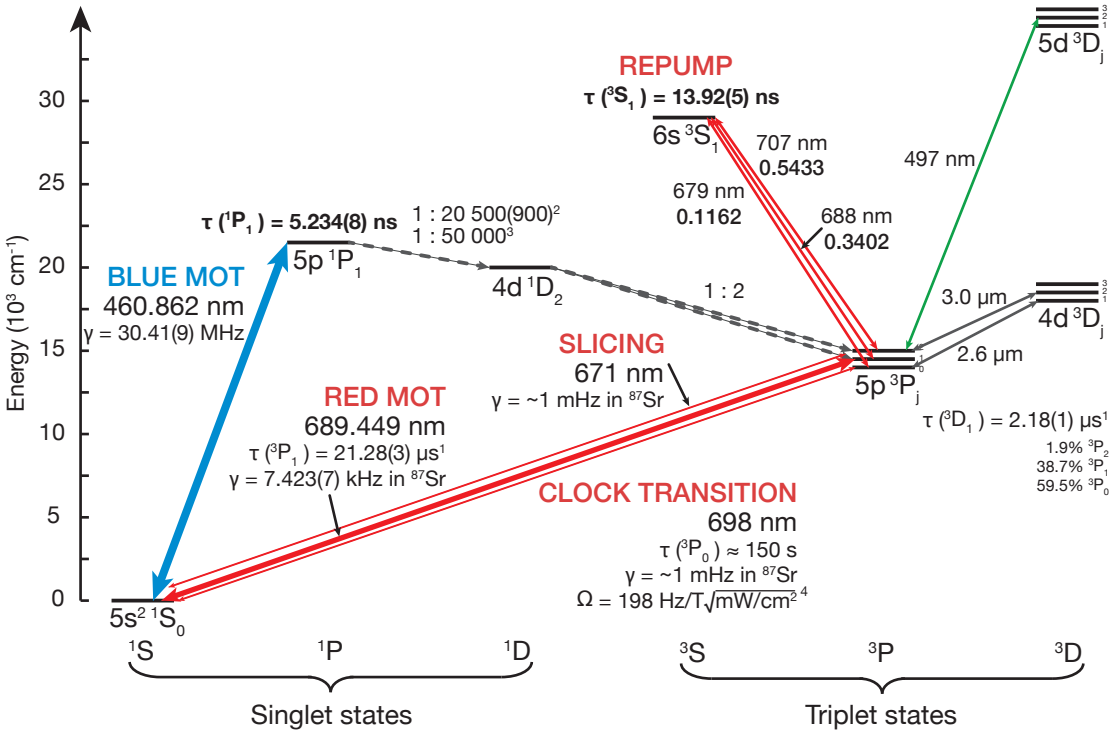

Figure 2.1 Strontium energy level diagram (adapted from Ref. [55]). The important transitions for our ultracold quantum simulator are highlighted with the appropriate labels. The indicated spectroscopic data is taken from Refs. [1]: [56], [2]: [57], [3]: [58], [4]: [59]. The lifetimes in bold are obtained from this work discussed in Chapter 4.

The advantages of laser cooling strontium atoms come from the variety of available transition strengths. Here, we are interested in the two main cooling transitions: the broad blue $^1S_0$-$^1P_1$ transition with a linewidth Γ of $2\pi\times\ 30.41(5)$ MHz and the narrow red $^1S_0$-$^3P_1$ transition with $\Gamma = 2\pi\times\ 7.423(7)$ kHz. For simplicity, let us first discuss laser

cooling of the bosonic isotopes that have vanishing nuclear spins, since the hyperfine structures of the fermionic isotope introduce further complications. As we have seen in Eqn. (2.2), a broader transition allows a larger momentum transfer during laser-cooling. Therefore, the blue transition is used for initial laser-cooling and slowing of atoms effusing from a hot oven at $\sim 500\,^{\circ}\mathrm{C}$ to the $\sim 30\ \mathrm{m/s}$ capture velocity of the blue MOT operating on the blue transition.

While operating the blue MOT, the $^1\mathrm{P}_1$ atoms decay into $^1\mathrm{D}_2$ with a branching ratio of 1:20000 [57] and subsequently decay further into $^3\mathrm{P}_{1,2}$ states with a branching ratio of 2:1, as illustrated in Fig. 2.1. Therefore, the atoms lost from the blue MOT cycle due to this decay channel need to be brought back into the cycle. Fortunately, the atoms decayed into $^3\mathrm{P}_1$ return to the ground $^1\mathrm{S}_0$ state at a rate given by the natural decay rate $\Gamma_{^3\mathrm{P}_1} = 2\pi\times\ 7.4\ \mathrm{kHz}$ ($\tau_{^3\mathrm{P}_1}$=21 μs). However, the $^3\mathrm{P}_2$ state is metastable with a lifetime of $520\ \mathrm{s}$ [60], and the $^3\mathrm{P}_2$ Zeeman substates with $m(^3\mathrm{P}_2)$=1,2 can be trapped in the magnetic trap created by the quadrupole field of the blue MOT. The atoms accumulated in this $^3\mathrm{P}_2$ magnetic trap can be stored for a long time that is limited only by the collisions with the background gas [61]. This vacuum-limited lifetime can be several minutes, depending on the pressure of the vacuum chamber. For this reason, these accumulated atoms need to be *repumped* back to $^1\mathrm{S}_0$ via optical pumping to go back to the blue MOT cycle. There are many choices for the possible repump trajectories that are detailed in Ref. [61]. One option, which is used in this thesis, is to repump the atoms via the $^3\mathrm{P}_2$-$^3\mathrm{S}_1$ and $^3\mathrm{P}_0$-$^3\mathrm{S}_1$ transitions. To achieve this, we use $707\ \mathrm{nm}$ and $679\ \mathrm{nm}$ lasers resonant with each transition, respectively. In this repumping scheme, $^3\mathrm{P}_2$ is excited to $^3\mathrm{S}_1$ via the $707\ \mathrm{nm}$ laser beam, and the excited $^3\mathrm{S}_1$ state decays back into the triple manifolds, $^3\mathrm{P}_0$, $^3\mathrm{P}_1$, and $^3\mathrm{P}_2$ according to the branching ratios specified in Fig. 2.1. The $^3\mathrm{P}_0$ clock state is also metastable with a lifetime of $\sim 150\ \mathrm{s}$. For this reason, the role of the $679\ \mathrm{nm}$ beam is to excite $^3\mathrm{P}_0$ back to $^3\mathrm{S}_1$, preventing the loss of atoms via this decay channel to $^3\mathrm{P}_0$. The blue MOT cycle is closed by operating the MOT with the repumping beams, and this MOT is called a *bright* steady-state blue MOT.

As noted above, the atoms can also be accumulated in the $^3\mathrm{P}_2$ magnetic trap. In this case, the *dim* blue MOT operates in the absence of the repump beams to allow the atoms to occupy the $^3\mathrm{P}_2$ magnetic trap. The repump beams are used later to bring the accumulated atoms back from the $^3\mathrm{P}_2$ states to $^1\mathrm{S}_0$. Either method, accumulating atoms in the bright steady-state blue MOT or in the $^3\mathrm{P}_2$ magnetic trap, is widely used in strontium experiments. Nevertheless, the vacuum-limited lifetime of the $^3\mathrm{P}_2$ states in the magnetic trap allows for prolonged atom loading time, which is critical for isotopes with low abundance such as ^{84}Sr [62].

The final temperature after the blue MOT, regardless of whether the atoms are accumulated in the bright steady-state blue MOT or the $^3\mathrm{P}_2$ magnetic trap, is limited by the Doppler temperature, which is $0.7\ \mathrm{mK}$. To cool the atoms further, the MOT is switched over from using the broad blue $^1\mathrm{S}_0$-$^1\mathrm{P}_1$ transition to the narrow red $^1\mathrm{S}_0$-$^3\mathrm{P}_1$ transition,

which has a linewidth $\sim$4000$\times$ narrower. Laser cooling using this narrow transition results in a Doppler temperature of $180\ \mathrm{nK}$, which is lower than the recoil temperature of $230\ \mathrm{nK}$, enabling cooling down to the fundamental limit of laser cooling. However, because of the large gap between the linewidths of the blue and red transitions, the capture velocity of the standard red MOT is far smaller than the final velocity of atoms in the blue MOT. This discrepancy results in losing most of the atoms during the transfer between the two stages of the MOT. The solution to this problem is to artificially broaden the capture velocity of the red MOT by modulating the laser frequency and reducing the magnetic gradient by an order of magnitude.

This initial red MOT stage, where the laser spectrum is artificially broadened via frequency modulation, is called the broadband red MOT [49, 37, 63]. During this stage, sinusoidal modulation or rapid scanning of the laser's frequency using an acousto-optic modulator (AOM) creates sidebands that typically span a detuning range between $-150\ \mathrm{kHz}$ to $-8\ \mathrm{MHz}$ with a spacing of $20\ \mathrm{kHz}$. It can be seen that each comb performs laser cooling at a detuning given by the comb's frequency with its respective power broadened linewidth Γ. Here, each comb has an intensity I of roughly I/N_{comb}, where N_{comb} is the number of comb lines. Each comb interacts with the atoms within the capture radius r_{cap} that is roughly given by the position where the amplitude of the radiative force is maximum. This maximum point occurs when the detuning balances the Zeeman shift (Eqn. (2.4)), $r_{\mathrm{cap}} = \Delta/(\mu_B g_J(^3\mathrm{P}_1)(\partial B/\partial z'))$ with $g_J(^3\mathrm{P}_1) = 1.5$. Considering all three spatial directions, this region is an ellipsoid due to the stronger axial magnetic field gradient of the quadrupole MOT field configuration. When $\Gamma' = \Gamma\sqrt{1+s_0} > \Delta$ for each comb, the cooling achieved by a comb resembles the standard broadband Doppler cooling, and the atoms occupy the whole ellipsoid [49, 37]. In contrast, for the case when $\Gamma' < \Delta$, each comb produces a box potential that is tilted along gravity, causing the atoms to sag at the bottom of the ellipsoid [49, 37]. In particular, when $\Gamma' \sim \Gamma$, the radiative force is only 16$\times$ larger than gravity ($\hbar k\Gamma/(2mg)$); thus the effect of gravity cannot be neglected. In many cases, each comb of the broadband stage operates in the second regime $\Gamma' < \Delta$, and due to the overlapping ellipsoids from many comb lines, the atoms occupy the entire volume of the largest ellipsoid given by the comb with the largest detuning.

As a next step, the laser's frequency modulation is turned off to compress the red MOT, and the detuning is tuned close to the resonance. At the same time, the beam intensity dramatically is reduced as well. This stage is called the single-frequency red MOT. Careful tuning of the detuning, power, and magnetic field gradients is required to obtain high phase-space density. In this single frequency MOT, a phase-space-density cloud of 10^{-2} [35] has been created, which is three orders of magnitude larger than a conventional MOT using alkali atoms [36]. The single-frequency red MOT has its characteristic pancake shape because the atoms sag towards the bottoms of the ellipsoid, as discussed above. Another interesting thermal-mechanical property is that when $\Gamma \sim \Delta$, the cooling mechanism requires a full quantum treatment since $\Gamma \sim \omega_{\mathrm{rec}}$. In this case, the temperature approaches the recoil limit of $230\ \mathrm{nK}$. The three distinct thermal-mechanical

laser-cooling dynamics occurring at $\Gamma' > \Delta$,$\Gamma' < \Delta$, and $\Gamma \sim \Delta$, are studied in detail in Ref. [49].

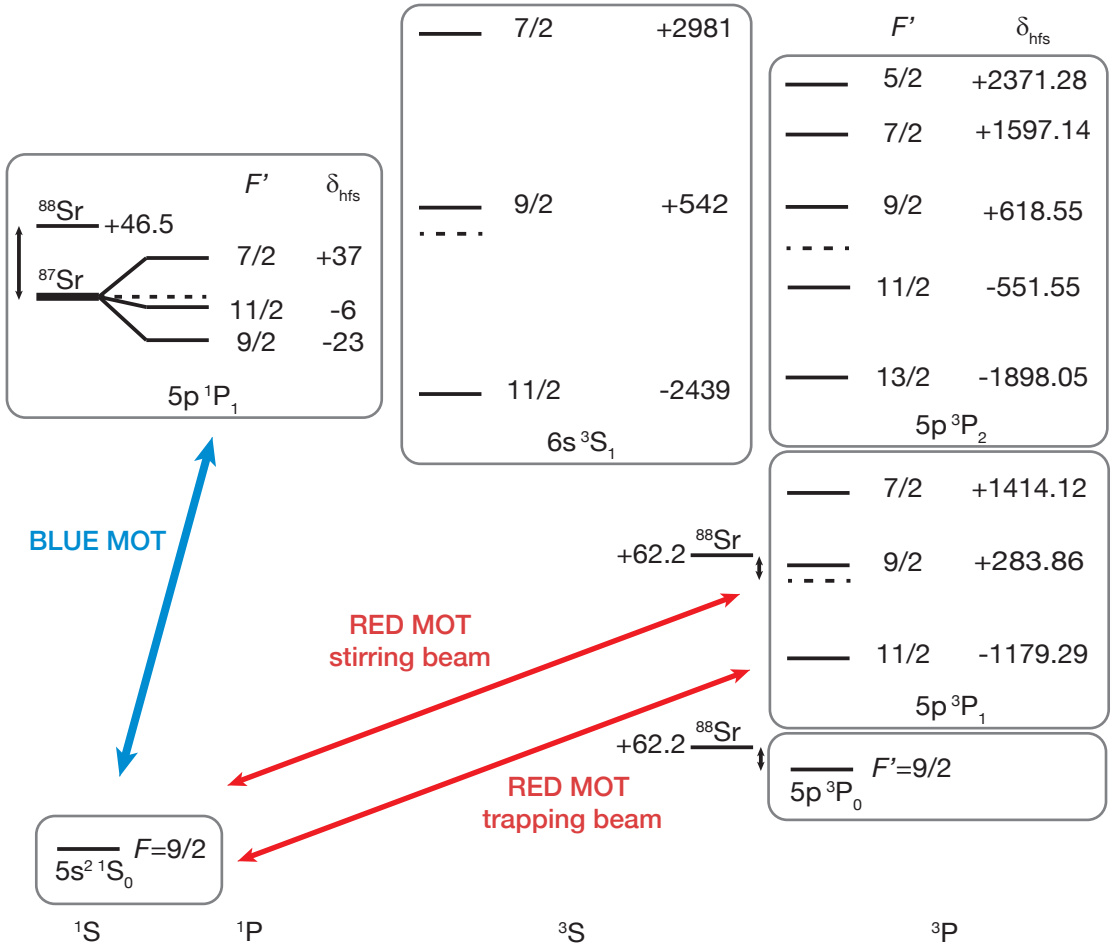

Figure 2.2 The ^{87}Sr hyperfine level structures (adapted from [61]). The hyperfine splittings $\delta_{\text{hfs}} = \Delta/(2\pi)$ are calculated with reference to a state assuming $I = 0$, which is denoted by the dashed lines. The splittings are expressed in MHz.

Let us shift our focus to laser cooling the fermionic isotope ^{87}Sr. Due to the non-vanishing nuclear spin $I = 9/2$, the states with non-zero angular momentum J (^{1}P$_1$, ^{3}P$_1$, and ^{3}P$_2$) split into multiple hyperfine states as shown in Fig. 2.2. Moreover, the ground state ^{1}S$_0$ splits into ten magnetic substates (m_F), and the hyperfine states of the excited states also split into $2F' + 1$ magnetic substates ($m_{F'}$), where F' specifies the hyperfine state of the excited electronic states. These hyperfine structures make the cooling procedure more complicated.

For the blue MOT, the hyperfine states of ^{1}P$_1$ are not resolved due to the broad linewidth

of the blue transition. Ideally, the MOT should operate using the ^{1}S$_0$ ($F = 9/2$)-^{3}P$_1$ ($F' = 11/2$) transition; however, this unresolved spectrum results in unfavorable excitation to the $F' = 7/2$ and $F' = 9/2$ states. There has been a rough estimate that the fermionic blue MOT performs worse in terms of the accumulated atom number compared to the bosonic MOT [61], but there has not been a detailed study. Moreover, the repumping scheme discussed above becomes more complicated as well due to the hyperfine splitting of the ^{3}P$_2$ state. Because of this reason, the $707\ \mathrm{nm}$ repump beam is typically frequency modulated to address larger frequency ranges. Despite these complications, in practice, operating the fermionic blue MOT is similar to operating the bosonic blue MOT, other than the need to shift the laser frequencies appropriately to address the fermionic isotope.

In contrast, the fermionic red MOT [64, 65, 37] changes more dramatically than the bosonic red MOT. The ^{3}P$_1$ state splits into three hyperfine states of $F' = 11/2$, 9/2, and 7/2. Because of the narrow linewidth and large hyperfine splittings, the transitions to each hyperfine state of ^{3}P$_1$ from ^{1}S$_0$ are resolved. Therefore, the red MOT can selectively operate on the ^{1}S$_0$ ($F = 9/2$) - ^{3}P$_1$ ($F' = 11/2$) transition without any unwanted excitations to the other ^{3}P$_1$ hyperfine states. However, due to a large difference in the Landé g-factors ($g_{F'}(^3\mathrm{P}_1\ F' = 11/2)/g_F(^1\mathrm{S}_0) \gg 1$) between the ^{1}S$_0$ (F=9/2) and ^{3}P$_1$ ($F' = 11/2$), the red MOT beams in a given magnetic field can be resonant, red-detuned or blue-detuned depending on the ground m_F state, leading to some transitions being repelled by or attracted to the trap's center. The solution to this problem is to use an additional beam to *stir* [64] the populations of m_F states. Therefore, the red MOT for ^{87}Sr operates using two colors, one *stirring* light on the ^{1}S$_0$ ($F = 9/2$) - ^{3}P$_1$ ($F' = 9/2$) transition and the other used as the *trapping* light, which uses the ^{1}S$_0$ ($F = 9/2$) - ^{3}P$_1$ ($F' = 11/2$) transition. The stirring light efficiently mixes the population of the magnetic states via optical pumping, and the trapping light operates the MOT. The fermionic red MOT also operates in two stages, broadband and single-frequency MOTs, and cools the atoms to $\sim 1\ \mu\mathrm{K}$. However, unlike the bosonic isotope, the atoms occupy the whole volume of the ellipsoid, even in the single-frequency MOT stage, because the resonant conditions for each m_F - $m_{F'}$ states are different.

So far, we have described the operation of a conventional red MOT. Recently, narrow-line optical molasses based on the rapid adiabatic passage [66–69] gained much attention due to their efficiency and robustness. We have modified our red MOT based on this new technique for both bosonic and ferminoic isotopes, and describe it in Chapter 3.

Because of the low temperature of the atomic cloud after the red MOT, atomic clouds with a phase-space density of 0.3 [37] have been created by carefully loading the laser-cooled cloud into a dipole trap. This phase-space density is only an order of magnitude lower than the critical density required for a BEC. Due to this advantage, the BEC or degenerate Fermi gas can be produced without large atom loss and with a reduced cycle time using strontium atoms, even after the lossy evaporative cooling step. All naturally

occurring strontium isotopes have been brought to quantum degeneracy [37, 61], and in particular, ^{84}Sr has been brought to quantum degeneracy using all-optical cooling [38] methods without the evaporative cooling step. As we will see later in Section 2.4, the narrow linewidth of the $^1S_0$-$^3P_1$ transition also enables cooling of the atoms loaded in the motional ground state of optical lattices [70] because the sideband spectrum in the optical lattices is well-resolved. This technique is called direct sideband cooling and is part of our sample preparation step (Chapter 5).

Next, we turn to the ultra-narrow clock transition $^1S_0$ (g) -$^3P_0$ (e). Although this transition is doubly forbidden, a small hyperfine mixing in ^{87}Sr allows direct single-photon excitation of the clock transition [71] with a linewidth of $1.35(3)$ mHz [54]. In the bosonic isotope ^{88}Sr, the hyperfine structure is absent, and so is the mixing. One way to access the transition is to apply an external magnetic field that creates the required state-mixing [72]. Given a fixed intensity, one needs to apply $\sim$1800 G to achieve the same Rabi frequency as in ^{87}Sr. A moderate magnetic field as low as $\sim$20 G has been used to induce the transition; however, this approach results in a strongly attenuated Rabi frequency compared to ^{87}Sr. Despite this additional requirement, the ^{88}Sr clock transition is also widely used because of the isotope's high natural abundance and simple structure. To take full advantage of the narrow clock transition, the laser-cooled atoms need to be loaded into optical lattices that confine the atoms tightly. Without this tight confinement, the clock excitation is hampered by Doppler broadening [73], which can be as large as 50 kHz if we consider a temperature of $\sim\mu$K for the laser-cooled sample. Because of the ultra-narrow clock transition and the tight confinement, ultracold strontium atoms loaded into deep magic optical lattices can be interrogated for a long time with reduced Doppler-related and ac-Stark light shift-related uncertainties. More importantly, each lattice site confining atoms can be treated as an independent quantum system; thus the signals from hundreds of lattice sites can be averaged, improving the signal-to-noise ratio of the clock interrogation. The above platform gives rise to optical lattice clocks, which have reached state-of-the-art frequency fractional instability below 10^{-18}, a value obtained by averaging the signal for one hour [24]. Both fermionic and bosonic strontium optical lattice clocks are widely used for their distinct advantages. Using the fermionic isotopes at ultralow temperatures can reduce collisional clock shifts because of the Pauli exclusion principle and allows easier excitation of the clock states, which does not require an external magnetic field. In contrast, the use of ^{88}Sr allows easier laser cooling and a higher signal-to-noise ratio due to the isotope's large natural abundance. Therefore, ^{88}Sr lattice clocks are particularly attractive for transportable lattice clock setups.

In this thesis, we also use the strontium clock states in optical lattices but for very different purposes. We will make use of both high and low intensity lattice regimes. In general, we will realize a quantum simulator at a low intensity lattice regime where atoms tunnel between neighboring lattice sites and the lattice depth will be raised for detection, preventing any quantum tunneling. In this deep lattice, we will make atoms fluorescent by applying a resonant light, then pick up the resulting fluorescence by us-

ing a high-resolution microscope to reconstruct the atom's density profile in each lattice site. This technique is called *quantum gas microscopy* [74, 75]. We are also interested in addressing both fermionic and bosonic species to enlarge the scope of simulations provided by their different particles statistics and scattering properties. Crucially, we will use state-selective traps to individually control $^1S_0$ (g) and $^3P_1$ (e). Unlike optical lattice clocks, which operate with optical lattices at a magic wavelength to completely decouple the internal electronic degrees of freedom from the external motional degrees of freedom, we operate our lattices at the so-called *tuneout* wavelength to maximally couple the internal and external degrees of freedom for highly state-sensitive traps. The generation of such state-selective traps yields longer atom lifetimes at a fixed lattice depth for strontium than for alkali metal atoms. We discuss this comparison in detail in the next section, Section 2.3. Moreover, the first proof-of-principle experimental demonstration of such lattices for strontium is introduced in Chapter 4.

Another interesting property of the fermionic clock states is decoupling of the clock states' nuclear spins I from the electron spins due to the vanishing electronic angular momentum J, i.e $\boldsymbol{I} \cdot \boldsymbol{J} = 0$ [76, 77]. For this reason, the fermionic clock allows an unique quantum computing architecture where the information is stored in the nuclear spin states and the state manipulation is done using electronic qubits. We will briefly discuss one of such proposals that use state-dependent lattices for entangling gates in Section 2.7.

Lastly, let us discuss $^3P_2$, the state that was already briefly introduced for the discussion of the blue MOT. Similar to the clock transition, the $^1S_0$-$^3P_2$ transition is doubly forbidden in the pure LS coupling picture. However, a small hyperfine mixing in ^{87}Sr allows a dipole transition between $^1S_0$ (F=9/2) and $^3P_2$ (F'=7/2,9/2,11/2) with a linewidth of $1\ \mathrm{mHz}$ [78], and the $^1S_0$ (F=9/2)-$^3P_2$ (F'=5/2,13/2) transitions are not dipole-allowed but can be accessed as a magnetic quadrupole transition (M2) [79, 80]. In the bosonic isotope, $^1S_0$-$^3P_2$ are also allowed as M2 [79, 81], and the transition strengths depend on the polarization of the light and magnetic field [81, 79]. Compared to the clock states, $^3P_2$ ($m_{J'} \neq 0$) features both narrow linewidth and enhanced sensitivity to an external magnetic field. These properties make $^3P_2$ ideal for single-site addressing, thus $^3P_2$ can be used to read-out information in quantum computation. For our machine, this transition is ideally suited for preparing atoms in a single layer of a 3D optical lattice, which is a necessary preparatory step for quantum gas microscopy. This step, which we colloquially referred to as *slicing*, is currently being implemented in the laboratory and will be detailed in the subsequent Ph.D. thesis.

2.3 Strontium in state-dependent optical lattices

In this section, we compare the dynamic polarizability $\alpha(\omega)$ of rubidium and strontium. This comparison will show why strontium permits a more versatile generation of state-

dependent optical traps where atoms can be trapped with long lifetime. For a rubidium atom, whose energy-level structure is shown in Fig. 2.3(a) top, we take the two hyperfine states of ^{87}Rb, $^2S_{1/2}$ $(F = 1)$ and $^2S_{1/2}$ $(F = 2)$ that are separated by the energy $\hbar\Delta_{\text{hfs}}$ with $\Delta_{\text{hfs}} = 6.8$ GHz, as the ground g' and excited e' states, respectively, to construct an optical qubit. It is common to consider the upper hyperfine state of $^2S_{1/2}$ as e' instead of electronic excited states, $^5P_{3/2}$ or $^5P_{1/2}$, because the electronic excited states have a short lifetime of tens of nanoseconds, making them unsuitable for many quantum applications. For strontium, we take the two electronic clock states: $|g\rangle = |^1\text{S}_0, J = 0\rangle$ and $|e\rangle = |^3\text{P}_0, J = 0\rangle$ of ^{88}Sr. *The notation above will be used throughout the rest of the thesis: g and e refer to $^1S_0$ and $^3P_0$ of strontium, respectively.* Although we consider ^{88}Sr for this comparison because the calculation of $\alpha(\omega)$ for ^{87}Sr becomes more complicated due to the hyperfine states (detailed in Chapter 4), the same comparison holds for ^{87}Sr.

Before we look at the energy level structures of the two atoms in detail, let us review the concept of dynamical polarizability $\alpha(\omega)$, which was introduced in Section 2.1. This polarizability is one of the core parameters that determine optical trap depth, and we provided its expression for a two-level system in Eqn. (2.6). Here, we extend this expression to a multi-level atom and highlight the important differences compared to the two-level case. For a multi-level atom in a state k, all dipole-allowed transitions to higher states l should be considered, leading to

$$\alpha(\omega) = 6\pi\epsilon_0 c^3 \sum_l \frac{\Gamma_{lk}}{\omega_{lk}^2(\omega_{lk}^2 - \omega^2 - iA_l\frac{\omega^3}{\omega_{lk}^2})} \tag{2.21}$$

$$\approx 3\pi\epsilon_0 c^3 \sum_l \frac{\Gamma_{lk}}{\omega_{lk}^3}\left[\frac{-1}{\Delta_{lk}} + i\frac{A_l}{2\Delta_{lk}^2}\right] \tag{2.22}$$

$$= \sum_l \left(\text{Re}[\alpha_l(\omega)] - i\frac{A_l}{2\Delta_{kl}}\text{Re}[\alpha_l(\omega)]\right). \tag{2.23}$$

Here, $\Delta_{lk} = \omega - \omega_{lk}$ where ω_{lk} is the resonance frequency of the transition between l and k, and $\alpha_l(\omega)$ is the polarizability contribution from the state l. Compared to $\alpha(\omega)$ of a two-level system (Eqn. (2.6)), Eqn.(2.21) has two modified terms: a partial decay rate Γ_{lk} and a total decay rate $A_l = 1/\tau_l$. Since l can decay into multiple states, Γ_{lk} takes into account a probability of l decaying to k, and this probability depends on the laser polarization as well as the electronic and nuclear angular momenta of the involved states. We will look at these dependencies in more detail in Chapter 4. By complex expanding and approximating Eqn. (2.21) as discussed for the two-level case, we see that $\text{Re}[\alpha_l(\omega)] \propto \Gamma_{lk}$ and $\text{Im}[\alpha_l(\omega)] \propto \Gamma_{lk}A_l$ in Eqn. (2.22). Thus, $V_{\text{dip}} \propto \sum_l \Gamma_{lk} I(r)$ and $\Gamma_{\text{sc}} \propto \sum_l \Gamma_{lk}A_l I(r)$ according to Eqn. (2.5) and Eqn. (2.11), respectively. This observation follows from the fact that the excited state population gets driven by Γ_{lk}, but the rate at which it scatters is given by the total decay rate A_l. In addition, previously, we observed a simple relationship $\Gamma_{\text{sc}} \sim V_{\text{dip}}$ (Eqn. (2.12)) for a two-level system. However, as shown in Eqn. (2.23), this simple relationship does not hold for a multi-level atom because of the prefactor A_l/Δ_{kl}

in the imaginary term.

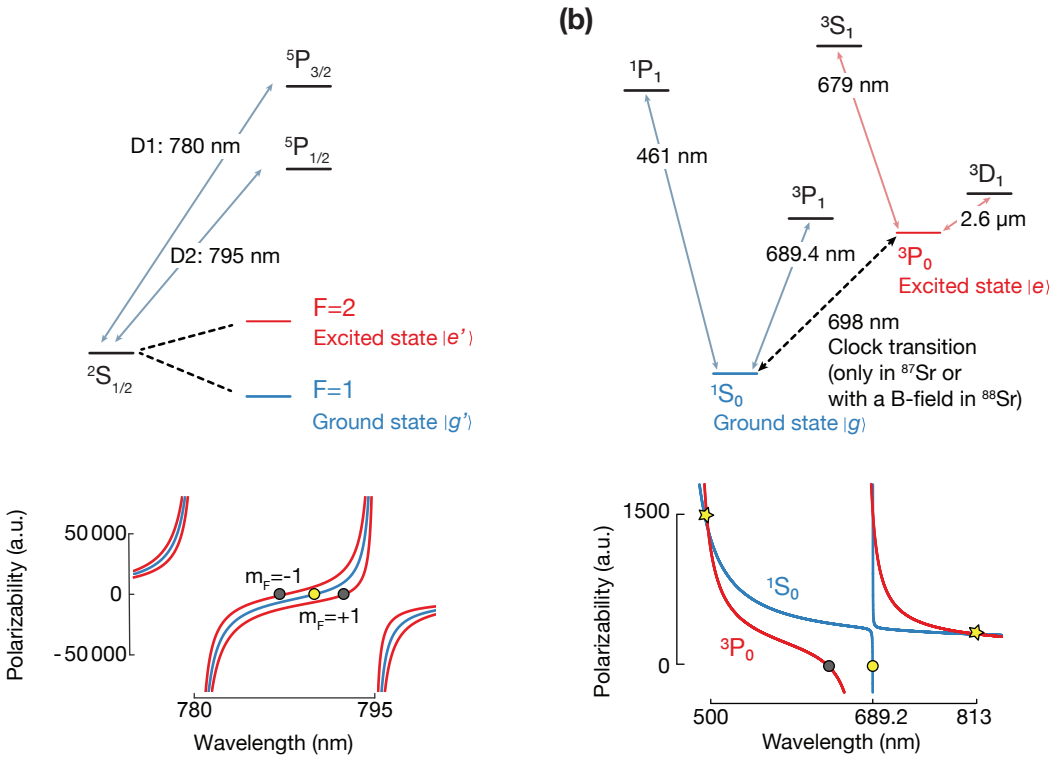

Figure 2.3 Polarizability comparison between ^{87}Rb and ^{88}Sr. (a). Simplified ^{87}Rb level diagram [top] and Re($[\alpha(\omega)]$) of $|g'\rangle = \left|^2S_{1/2}, F = 1, m_F = 0\right\rangle$ (blue) and $|e'\rangle = \left|^2S_{1/2}, F = 2, m_F = \pm 1\right\rangle$ (red) are shown below in units of a.u. (1 a.u.=$4\pi\epsilon_0 a_0^3$). (b) Simplified Sr level diagram, and Re$[\alpha(\omega)]$ of $|g\rangle = \left|^1\mathrm{S}_0\right\rangle$ [blue] and $|e\rangle = \left|^3\mathrm{P}_0\right\rangle$ [red] are shown below. At the "magic wavelength" [star], g and e experience the same polarizability, thus the same trap depth. At the "tune-out wavelength" of g (g'), g (g') is free to move and e (e') is tightly trapped [yellow circle], and at the e (e') "tune-out wavelength", e (e') is free to move [gray circle].

Let us first calculate Re$[\alpha(\omega)]$ of a rubidium atom. Looking at its energy structure in Fig. 2.3(a) top, we observe that both g' and e' of ^{87}Rb are connected to the same excited electronic states $^5P_{1/2}$ and $^5P_{3/2}$ via the dipole-allowed transitions that are referred to as the D_1 and D_2 lines, respectively. For this reason, apart from the small differences in Γ_{lk} and in the detuning due to Δ_{hfs}, the numbers that go into calculating $\alpha(\omega)$ for g' and e' are similar. To construct an optimal state-dependent trap, we consider a case where the difference between the two $\alpha(\omega)$ is maximized: ^{87}Rb trapped in circularly polarized light (σ^+). The circular polarization lifts the degeneracy of the magnetic sub-states and maximizes the difference in Γ_{lk} between $m = 0$, and ± 1. The calculations of Γ_{lk} for the different magnetic substates are described in Ref. [50], and we use their results to calculate Re$[\alpha(\omega)]$ of g' and e' as a function of wavelength, as shown in Fig 2.3(a). To

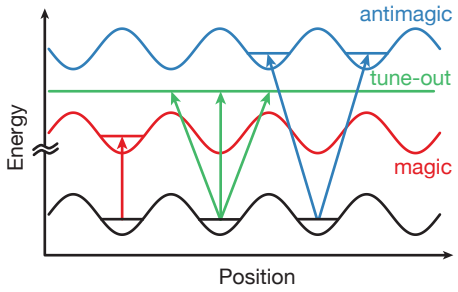

Figure 2.4 Illustration of different types of optical lattices generated with magic, tune-out, and anti-magic wavelengths (from Ref. [82]). The potential shown in black is a reference potential for g, and blue, green, and red are the possible potentials for e or vice versa.

calculate Re$[\alpha(\omega)]$, we made an approximation that $\Delta \gg \Delta_{\mathrm{hfs}}$. As we expected, the plots show similar qualitative behaviors for $m = 0, \pm 1$ states because they all couple to the same excited electronic states.

For the ^{88}Sr clock states, as shown in Fig. 2.3(b) top, g and e are coupled to *completely different families of the excited electronic states*. The main contributions to $\alpha(\omega)$ of g are the ^{1}S$_0$-^{1}P$_1$ and ^{1}S$_0$-^{3}P$_1$ transitions. In contrast, the main transitions that contribute to $\alpha(\omega)$ of e are ^{3}P$_0$-^{3}D$_1$, ^{3}P$_0$-^{3}S$_1$, and other upper states that are not shown in Fig. 2.3(b). For this reason, Re$[\alpha(\omega)]$ of the clock states shown in Fig 2.3(b) bottom illustrate qualitatively different behaviors between the two.

In Fig 2.3(b), we highlight several special wavelengths: the magic and tune-out wavelengths that are indicated with stars and circles, respectively. At magic wavelengths, the two clock states have matching Re$[\alpha(\omega)]$; thus, the optical traps generated at these wavelengths produce identical trap depths for the two. Although such wavelengths exist at both 497 nm and 813 nm, the latter is used more widely because of its flatter slope as a function of wavelength, which leads to the insensitivity of a trap depth to the trap's frequency drifts. At tune-out wavelengths, Re$[\alpha(\omega)]$ of one of the states completely vanishes. As a result, one can generate a highly selective trap that traps only one specific state with non-vanishing Re$[\alpha(\omega)]$. For strontium atoms, the tune-out wavelengths of ^{1}S$_0$ and ^{3}P$_0$ occur at 689 nm and 633 nm, respectively. Using these properties, various different types of optical lattices can be generated as illustrated in Fig. 2.4. In the figure, we also show "anti-magic" lattices where the clock states are trapped at alternating lattice nodes at the same trap depths ($\alpha_g(\omega) = -\alpha_e(\omega)$). For the strontium clock states such traps can be generated at wavelengths of 650 nm or 400 nm.

We have seen qualitatively why strontium is the better choice compared to rubidium for constructing state-dependent lattices. However, the special wavelengths such as magic and tune-out ones also exist for rubidium [83, 84] (the magic wavelength for rubidium is not shown in Fig 2.3(a) as it requires considering a case with different laser polarization).

Now, let us answer an important question: how much better is a state-dependent trap for ^{88}Sr than the one for ^{87}Rb? To answer this question, we consider a scenario where the ground state is trapped in a completely state-dependent lattice generated at a tune-out wavelength of the excited state. We will consider the above scenario for both ^{87}Rb and ^{88}Sr and compare the trapped ground state's scattering rates Γ_{sc} for both cases at the same trap depth.

Since $\Gamma_{\text{sc}} \propto \text{Im}[\alpha(\omega)]I(r,z)$, we first compare the intensity $I(r,z)$ required to generate the same trap depth for the two cases. For ^{87}Rb, the excited state tune-out wavelength $\lambda_{e'}$ lies at 792 nm or 788 nm if we treat e' as $F = 2$ (m=$+1$) or $F = 2$ (m=-1), respectively (Fig. 2.3(a)). Let us take $m = -1$ as e' because $\lambda_{e'}$ is slightly further detuned from the D_1 and D_2 lines that lie at 780 nm and 795 nm, respectively, which would reduce Γ_{sc}. For ^{88}Sr, the e tune-out wavelength λ_e occurs at 633 nm. At the wavelengths $\lambda_{e'}$ and λ_e, Re$[\alpha(\omega_{e',e})]$ of g' and g are ~ -6000 a.u. and ~ 450 a.u. with a.u=$4\pi\epsilon_0 a_0^3$, respectively. For this reason, an order of magnitude more intensity is required for the case of ^{88}Sr.

Now let us take a look at the other term, Im$[\alpha(\omega)]$, that also contributes to Γ_{sc}. This term scales as $(\Gamma_{lk}A_l/\Delta_{lk})^2$ for each of the transitions, according to Eqn. (2.22). The total decay rate A_l of $^5P_{3/2}$ and $^5P_{3/2}$ of ^{87}Rb is $\sim 2\pi\times 6$ MHz for both states, and Γ_{lk} is modified from A_l by the relative transition strengths given by $\frac{2}{3}(1+g_F m_F)$ and $\frac{1}{3}(1-2g_F m_F)$ for the D_1 and D_2 lines, respectively [50]. Here, $g_F = -1/2$ and $1/2$ for $F = 1$ and 2, respectively. Because these relative transition strengths result in only small corrections for the estimates of our interest, we neglect these factors for simplicity and treat $\Gamma_{lk} \sim A_l$. Then, calculating $(A_l/\Delta_{lk})^2$ results in $\sim 3\times 10^{-12}$ from each D_1 and D_2 transition. For ^{88}Sr, the two contributing transitions to Γ_{sc} of g are the ^{1}S$_0$-^{1}P$_1$ and ^{1}S$_0$-^{3}P$_1$ transitions, as shown in Fig. 2.3(b) top. Even without doing the calculation, we can already see that these two transitions are much further away from λ_e. It can also be shown that $\Gamma_{lk} = A_l$ for the two contributing transitions (detailed in Chapter 4). Then, calculating the same factors $(A_l/\Delta_{lk})^2$ for the above two transitions, we obtain $\sim 3\times 10^{-14}$ and $\sim 4\times 10^{-20}$ for the ^{1}S$_0$-^{1}P$_1$ and ^{1}S$_0$-^{3}P$_1$ transitions, respectively. The results show that we can safely assume that most scattering results from the ^{1}S$_0$-^{1}P$_1$ transition, and its associated $(\Gamma_{lk}A_l/\Delta_{lk})^2$ factor is about two orders of magnitude smaller than that for the case of rubidium. Combining our previous result of the intensity $I(r,z)$ comparison result, since $\Gamma_{\text{sc}} \propto \text{Im}[\alpha(\omega)]I(r,z)$, we conclude that g has roughly an order of magnitude longer lifetime than g' when the two are trapped in optical traps of the same depth generated at the tune-out wavelength of their respective excited states.

Now, let us consider the reverse scenario: the excited state is trapped by the trap generated at the tune-out wavelength of the ground state. In this case, the g' tune-out wavelength ($\lambda_{g'}$) lies at 790 nm, and Re$[\alpha(\omega_{g'})]$ of e' is ~ 6000 a.u.. Since the transitions that contribute to Im$[\alpha(\omega_{g'})]$ of e' are the same as those of g' and also $\lambda_{g'} \sim \lambda_{e'}$, $(\Gamma_{lk}/\Delta_{lk})^2$ of the D_1 and D_2 transitions are of the same order as in the above case: 1.5×10^{-12} and 6×10^{-12} from the D_1 and D_2, respectively. In contrast, the situation changes quite

dramatically for ^{88}Sr. Here, the g tune-out wavelength (λ_g) lies at 689.2 nm, $\sim$50 nm away from λ_e, and e has Re$[\alpha(\omega_g)]$ of $\sim$1500 a.u.. Moreover, the transitions that contribute to Im$[\alpha(\omega_g)]$ of e are very different from those for Im$[\alpha(\omega_e)]$ of g. In particular, $\alpha(\omega_g)$ of e is mostly dominated (87%) [40] by the ^{3}P$_0$-^{3}S$_1$ transition; thus, we will consider only this transition to estimate the scattering. The ^{3}S$_1$ state has a total linewidth of $2\pi\times10$ MHz and has a partial decay rate to ^{3}P$_0$ of $2\pi\times1.5$ MHz. Therefore, Im$[\alpha(\omega)] \propto \Gamma_{^3\mathrm{S}_1-^3\mathrm{P}_0} A_{^3\mathrm{S}_1}/\Delta^2_{^3\mathrm{S}_1-^3\mathrm{P}_0} \sim 1\times10^{-12}$. Here, one can see that the lifetimes of e and e' are of a similar order. Therefore, we cannot neglect the relative transition factors we have neglected for the case of rubidium. After properly including these factors, the comparison reveals approximately a factor of two longer lifetime for e than e' at the same trap depth.

Considering a case that uses both independent state-dependent lattices at λ_g and λ_e, using the strontium clock states is again advantageous compared to the hyperfine states of a rubidium atom. To see this, we want to look at the scattering rate of g' (g) in the presence of the trap generated at λ'_g (λ_g). Although g' (g) experiences $V_{\mathrm{dip}} = 0$ at this wavelength, $\Gamma_{\mathrm{sc}} \neq 0$ for a multi-level atom. As before, the trap for strontium clock states is four time more intense than that of rubidium because Re$[\alpha]$ is four times smaller for e at λ_g than e' at $\lambda_{g'}$. However, it can be calculated that $(A_l/\Delta_{lk})^2$ is about two orders of magnitude smaller for g than for g', providing a much longer lifetime of g in the presence of the trap at λ_g than that of g' in the presence of the trap at λ'_g. A similar calculation can be done for the opposite case: e' (e) in the presence of the trap generated at λ'_e (λ_e). Although we skip this calculation here, the result will again show the advantages of strontium.

In addition, it should also be noted that making state-dependent lattices with rubidium involves using circularly polarized light and magnetically sensitive states. Therefore, the traps will be sensitive to both stray magnetic fields and laser polarization drifts. In contrast, the traps for ^{88}Sr can be made with linear polarization, and since the clock states have $J = 0$, the states will be insensitive to magnetic fields.

In this Section, we considered the case when the laser's frequency spectrum lies exactly at the desired tune-out wavelengths without any background light. However, in reality, a laser beam's spectral background, due to its amplified spontaneous emission (ASE), can extend over a large wavelength range of several nm. Although we have shown that strontium clock states feature longer lifetimes compared to rubidium atoms, since λ_g is only 150 GHz detuned from the ^{1}S$_0$-^{3}P$_0$ transition, even very weak ASE light near the transition can cause uncontrolled heating of g. Therefore, despite the advantages, implementation of high-fidelity state-dependent lattices still requires careful technical consideration. In Section 2.5 and Chapter 4, we present a method to combat this problem.

2.4 Clock spectroscopy in magic lattices

Thus far, we have demonstrated how to create optical lattice potentials under various conditions such as magic, tune-out, and anti-magic. Now, let us briefly discuss the energy spectrum of trapped atoms in an optical lattice, and the absorption spectrum of the clock states. For simplicity, we consider only the spectrum in the magic lattices and will extend this spectrum to non-magic lattices in Chapter 5. Understanding this absorption spectrum is important because it provides a lattice trap frequency and sample temperatures [85, 86], and constitutes the basic working principle of the lattice cooling technique called sideband cooling [70, 87], which can cool atoms to the motional ground state.

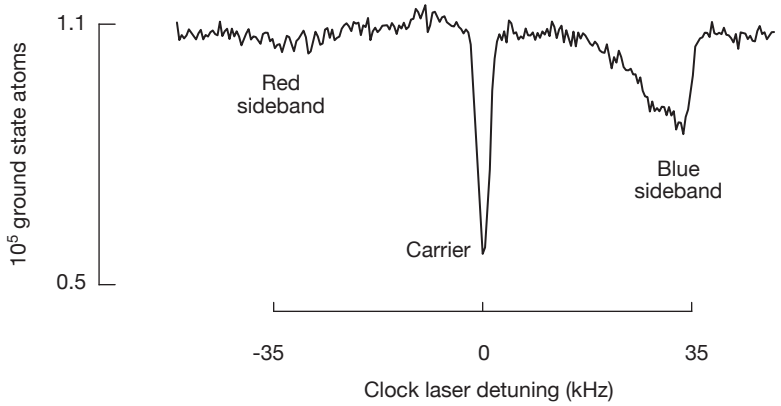

Figure 2.5 Clock sideband spectrum in a 1D lattice.

In the case where the atoms are trapped in deep optical lattices, where tunneling along the lattice is suppressed, the absorption spectrum resembles the spectrum of a harmonically trapped ion [73, 87], and a trapped atom occupies a discrete vibrational state n. Assuming an infinitely flat 1D lattice without any radial confinement and considering the quartic distortion by the sinusoidal lattice potential, the vibrational energy spectrum is [73]

$$E_n/h = \nu_t(n + 1/2) - \frac{\nu_{\text{rec}}}{2}(n^2 + n + 1), \tag{2.24}$$

where ν_t is a lattice trap frequency and ν_{rec} is the recoil frequency, $\nu_{\text{rec}} = \hbar k^2/2m$. Here, k is the wave-vector of a lattice and m is the mass of the atom. With this expression, we can explain all the spectral transitions observed in atoms trapped in a deep lattice.

A typical spectrum consists of three different types of transitions: carrier transitions that maintain the vibrational state, and red and blue sideband transitions that respectively remove and add a motional quantum. In a magic wavelength lattice, the transition frequencies of all carrier transitions are degenerate because the g and e lattices have the same trap frequencies, i.e $E^e_n/h - E^g_n/h = 0$ for all n where E^k_n is the energy of a state k in a vibration state n. From Eqn. (2.24), it can also be calculated that the first

red and blue sideband transitions are detuned from the carrier by $\omega_t - \omega_{\text{rec}}$. Since the power-broadened linewidth of the carrier is $\sim 2\pi\times$kHz$\ll \omega_t$, the sideband transitions are well-resolved from the carrier. Typically, the sideband transitions are highly suppressed compared to the carrier transitions, by a suppression factor that depends on the Lamb-Dicke parameter [87] η. The Lamb-Dicke parameter is characterized by the ratio of probe light recoil frequency to the lattice trap frequency, $\sqrt{\omega_{\text{rec}}^p/\omega_t}$, and describes how tightly the atom is bound compared to the probing wavelength. For all the applications described in this thesis, we work at the *Lamb-Dicke regime*, $\eta \ll 1$: the internal states are tightly bound to the lattice. Therefore, the probing light does not change the motional state, and any transitions that change the motional quantum by more than one are highly suppressed. The detailed derivations of the associated Rabi frequencies of all three types of transitions are available from Refs. [73, 86].

An example of the sideband spectrum in a 1D lattice that features all the three types of transitions is shown in Fig. 2.5. In the figure, one can see that all three transitions are well resolved, and the sideband amplitudes are suppressed compared to the carrier. Moreover, the relative amplitudes of blue and red sidebands can provide the temperature of the sample [73]. For instance, the red sideband in the figure is suppressed compared to the blue sideband due to a large ground vibrational state population. We see that the red and blue sideband peaks are smeared toward the carrier, due to two main reasons. First of all, the sideband transitions are non-degenerate, unlike the carrier transitions. For instance, the frequency of the blue sideband transitions are given by $E_{n+1}^e/h - E_n^g/h = \omega_t - \omega_{\text{rec}}(3n+2)/2$; thus, the higher blue transitions lie closer to the carrier. Since each peak's amplitude is dependent on both the level population that is Boltzmann distributed and its respective Rabi frequency, we observe that the sideband peak amplitude exponentially reduces closer to the carrier. Second, these multiple sideband peaks are not resolved; instead, they smear, because of the coupling between the radial and longitudinal motional states that we have neglected in Eqn. (2.24) [73]. In Chapter 5, we extend this discussion to 2D non-magic lattices and observe resolved non-degenerate carrier and blue-sideband transitions. Furthermore, we use the clock states' spectroscopic features in the 2D non-magic lattices to locally measure the sample temperature and to characterize our cavity-enhanced optical lattices.

2.5 Increasing the size of optical lattices

In Section 2.1, we have shown how to create an infinitely extended 1D optical lattice by considering a plane wave. However, since a more realistic model for a laser beam is a TEM_{00} mode with a Gaussian intensity profile, the lattice sites are no longer identical on length scales that are comparable to the finite transverse extent of the beams because the potential depth of the lattice varies. For this reason, the system sizes that can be simulated on quantum simulators are limited by the number of identical lattice sites that can be used.

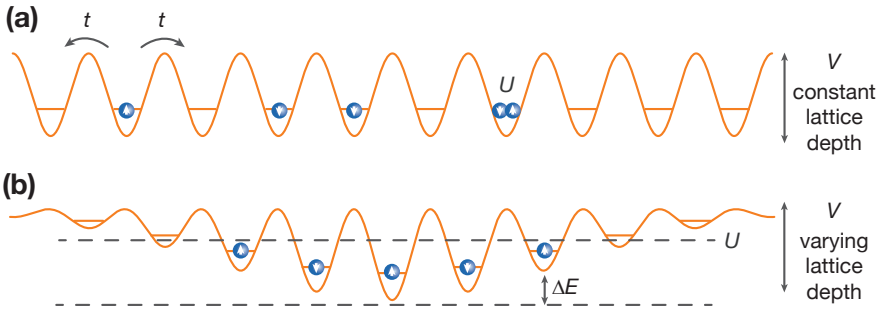

Figure 2.6 Fermionic atoms in an optical lattice. (a) Ultracold fermionic atoms trapped in infinitely extended optical lattices of depth V can tunnel between sties at rate t. Two fermions of opposite spin on the same site interact with interaction energy U. (b) Finite-sized optical lattices vary quadratically in depth causing a site-dependent energy offset ΔE, typically referred as harmonic confinement or a lattice envelope.

In quantum simulators, the depth variation in the optical lattice potential leads to spatial variation of the tunneling rate, the interaction parameters, and the chemical potential. Therefore, descriptions of such quantum systems must rely on local-density approximations [88] and take into account edge effects that can become more important than those in the bulk system. The inhomogeneity also limits the size of a potential Mott insulator [88], in which each lattice site is occupied by a single atom. This limit, in turn, restricts the size of quantum simulations, which are often initialized in a Mott insulating state. The fidelity of such simulations is then limited by the finite size and the imperfections of the initial Mott insulator.

Although our main interest is building a quantum simulator, the system size limitation due to harmonic confinement also hinders other lattice-based quantum technologies, the most prominent example being optical lattice clocks. One fundamental limit to optical lattice clocks' stability is the quantum projection noise, which scales as $\propto 1/\sqrt{N}$, where N is the number of atoms. In one-dimensional (1D) optical lattice clocks (the most common type), increasing the atom number leads to interaction-induced frequency shifts [89–91], which lower the clock accuracy. These shifts can be reduced by using 2D [92] or 3D lattices [93, 94], in which case the atom number is limited by the mode area or mode volume of the optical lattices, respectively. Here, the mode area (volume) refers to the transverse area created by the two (three) orthogonal beams that create the lattices, which is directly proportional to the number of usable lattice sites. Moreover, this system-size limit would also ultimately hinder implementing large-scale quantum computations consisting of tens of thousands of qubits.

2.5.1 Example of the system size: Mott insulator size

Let us provide a concrete example of how harmonic confinement limits the achievable system size. For this discussion, we focus on the application for quantum simulations. However, a similar calculation can be performed for other applications by considering an appropriate starting state of the particular application in interest to show the system size limitation due to the harmonic confinement.

One of the most common initial states for quantum simulations is a Mott insulator, a low entropy initial state in which a single atom occupies each lattice site. Since this is the starting state, the achievable Mott insulator size determines the size and thus the complexity of the simulation. In this Section, we show how this Mott insulator size depends on the waists of the beams that create the optical lattices.

The most important energy scales of quantum simulation in optical lattices are t and U, which respectively characterize the tunneling of atoms between neighboring sites and the interaction energy between two atoms on the same site as shown in Fig. 2.6(a). In two dimensions, a fermionic spin-1/2 Mott-insulator forms when the interaction energy U is approximately the same as the ground bandwidth $8t$ [14], filling each lattice site with exactly one atom.

However, since the lattice is not perfectly flat, there is an additional site-specific energy offset ΔE as shown in Fig. 2.6(b). This offset leads to an additional constraint, $\Delta E < U$, which limits the size of the Mott insulator. To estimate the system size, we first estimate at which lattice depth the constraint $U = 8t$ is satisfied [14]. Following Ref. [88],

$$U = \sqrt{8/\pi} k a E_{\text{rec}} (V/E_{\text{rec}})^{3/4}, \tag{2.25}$$

$$t \sim \frac{4}{\sqrt{\pi}} E_{\text{rec}} \left(\frac{V}{E_{\text{rec}}}\right)^{3/4} \exp\left[-2\left(\frac{V}{E_{\text{rec}}}\right)^{1/2}\right], \tag{2.26}$$

where $k = 2\pi/\lambda$ and a are the wave-vector and the scattering length, respectively. The lattice potential can be approximated as

$$V(x_1, x_2) \sim V[e^{-2x_1^2/w^2}\cos^2(kx_1) + e^{-2x_2^2/w^2}\cos^2(kx_2)]. \tag{2.27}$$

Using the expressions above, a Mott insulator forms when $V = E_{\text{rec}}[\ln(8\sqrt{2}/ka)]^2/4$. Let us consider the fermionic isotope ^{87}Sr which has $a = 96a_0$, where a_0 is the Bohr radius, and a nuclear spin $I = 9/2$. When using nuclear-spin-polarized atoms in a mixture of $|g, m_I = \pm 9/2\rangle$ in optical lattices created at a wavelength of 914 nm, the transition to a Mott insulator is expected to occur at $V \sim 8E_{\text{rec}}$. At this depth, the interaction energy U is $\sim$728 Hz. We can compare this energy U with the site-specific ΔE to estimate the

size of the Mott insulator. The site-specific energy ΔE scales with the harmonic confinement of the lattice, $M\omega^2 r^2/2$ where $r^2 = x_1^2 + x_2^2$ and $\omega = \sqrt{4V/Mw^2}$ is the radial trap frequency. Here, M is the mass of a ^{87}Sr atom, and w is the $1/e^2$ waist of the beams that create the lattices.

Setting $\Delta E = U$, we find the radius of the Mott insulator $r_{\text{Mott}} = w\sqrt{U/2V}$. Considering the waist of our cavity modes $w = 489(8)\ \mu\text{m}$, we expect a radius of $\sim$60 μm. The area defined by this radius corresponds to the region where the lattice depth is within $96 - 97\%$ of the maximum. The total atom number in this region $N_{\text{atoms}} = \pi r^2/(\lambda/2)^2$ which is $4{\times}10^4$ to $11{\times}10^4$ depending on the wavelength, which ranges from 1064 to $689\ \text{nm}$. Performing the same estimates using a waist of $80\ \mu\text{m}$ as used in Ref. [53], we obtain an atom number ranging from $1{\times}10^3$ to $3{\times}10^3$ for the same wavelength range.

2.5.2 Cavity-enhanced optical lattices

Any optical lattice experiment faces a trade-off between system size and lattice depth, given by the beam waist and intensity, respectively. Therefore, limited laser power leads to a technical limit on the system size. A natural candidate for increasing laser intensities is an optical cavity (or resonator). In a cavity, light circulating between mirrors constructively interferes with incoming light, thus enhancing the laser power circulating within the cavity. Since this enhancement factor depends on the mirror reflectivities, whereas a cavity-mode waist depends on the mirrors' radii of curvature, a cavity provides independent control over the circulating power and waist. This capability lets us achieve deep and large (and thus homogeneous) lattices simultaneously. Other approaches to improving lattice homogeneity use beam shaping via cylindrical lenses [95] or spatial light modulators [96]. However, these approaches face laser power limitations much earlier than power-enhancing buildup cavities do.

This cavity-based solution can be applied at any desired wavelength by optimizing the cavity mirror coatings to achieve the desired intra-cavity amplification factor. Therefore, this solution opens new possibilities to create large and deep lattices at wavelengths, even those where the laser powers are limited. In particular, this feature is necessary for implementations of state-dependent lattices for strontium since both λ_g ($689.2\ \text{nm}$) and λ_e=$633\ \text{nm}$ occur at wavelengths where the laser power is limited.

Creating state-dependent lattices for strontium in a cavity can also enhance the atomic lifetimes. In previous sections, we have seen that the tune-out wavelength of g lies at $-150\ \text{GHz}$ away from the narrow $^1\text{S}_0$-$^3\text{P}_1$ transition, and many applications require using both clock states in state-dependent lattices. Therefore, a tune-out laser beam that has any amplified spontaneous emission (ASE) background present at the narrow $^1\text{S}_0$-$^3\text{P}_1$ transition frequency will heat g, and thus, shorten its lifetime. In Chapter 4, we partly solved this problem using a holographic grating to filter out part of the tune-out laser's

background spectrum. However, this filtering happens naturally for a beam generated inside the cavity because cavity transmits a laser beam only when the cavity length matches the integer of a half wavelength of the laser beam. Therefore, the ASE background will be highly suppressed for a beam created in a cavity compared to free space beams.

Despite the obvious advantages of the cavity-enhanced optical lattices, implementing them in experiments brings technical challenges. While using one-dimensional cavity-enhanced optical lattices for atomic clocks has seen some success [97], implementation in two dimensions is more difficult due to precise requirements on the vertical overlap of orthogonal modes. Moreover, this overlap should be maintained not only during the experimental cycles, but also during the bake-out process of the vacuum chamber where the chamber is typically heated up to $\sim$200 °C. In addition to the overlap difficulties, past attempts have suffered from short lifetimes due to poor vacuum conditions [93] or increased lattice intensity noise due to the frequency-to-intensity noise conversion that occurs when a laser's frequency is stabilized to the resonance of a cavity [97].

In Chapter 5, we discuss our crossed cavity design and its implementation in an experiment that circumvents all the aforementioned stability problems. This success has been achieved by the careful construction of ultra-high-vacuum-compatible and monolithic crossed cavities with a near-perfect vertical overlap. The cavity mirror coatings have been optimized for creating different types of optical lattices for strontium. We experimentally demonstrate that there are no disadvantages of our approach in terms of atomic lifetimes compared to free space optical lattices, and that it also allows the creation of deep and large optical lattices at wavelengths where the available laser power is limited.

2.6 Quantum gas microscopes

In early experiments, the main method for obtaining information from quantum gases was limited to observation in momentum space, which was done by releasing atoms from the trap and taking a snapshot of their density distribution via absorption imaging. However, the relatively recent development of quantum gas microscopes [74, 75] has extended researchers' measurement capability to real space where a single lattice site can be resolved, allowing direct measurements of density and spin correlations. In our experiments, we also plan to implement the same technique to image and address individual lattice sites. These capabilities are crucial for future applications of our machine, described in detail in the next section (Section. 2.7).

Our microscope will use operating principles similar to the ones already developed and implemented for ytterbium [98] due to the similarity in electronic structure between the two species. To date, strontium quantum gas microscopes have not been employed in experiments, yet we plan to incorporate one soon in our work. We next briefly outline the planned working principle of the microscope.

A high imaging resolution will be achieved with λ_{image}=461 nm light for fluorescence detection on the $^1S_0$-$^1P_1$ transition. To prevent atom losses due to heating, we will simultaneously cool the atoms on the narrow-line transition $^1S_0$-$^3P_1$ at 689 nm with direct sideband cooling, a technique allowed by the resolved sideband spectrum discussed in Section 2.4. To capture the fluorescence light to reconstruct the density distribution, a high resolution objective with a numerical aperture (NA) of 0.7 will be used. With this objective, we will achieve a diffraction-limited resolution of $\lambda_{\text{image}}/(2\text{NA}) \approx 330$ nm, enabling site-resolved imaging of the 345-nm-spaced lattice sites created close to the 689.2 nm tuneout wavelength.

The high resolution imaging system will also be used for single-site addressing by first shaping the beam with a spatial light modulator. Since the addressing beam is tuned to the clock transition at 698 nm (λ_{clk}), a dichoric mirror will be used to couple the clock laser light through the objective. Here, the diffraction limited resolution is $\lambda_{\text{clock}}/(2NA) \approx$ 490 nm, larger than the lattice spacing. Therefore, there is some risk associated with the experimentally achievable addressing resolution. However, magnetic field gradients can be used to further increase the resolution.

2.7 Applications

We have presented our setup's ability to generate completely state-dependent lattices with long atomic storage times, to image and address atoms in a single site resolution using a high-resolution microscope, and to create cavity-enhanced lattices that produce an order of magnitude larger optical lattices than the current state-of-the-art, even at wavelengths where the laser power is limited. In this section, we present two main future directions for the experiments, made possible by combining the above tools.

2.7.1 Quantum simulation of light-matter interfaces

So far, using a semi-classical approach, we have discussed the interactions between individual atoms and a light field with a large mode volume, placed in a vacuum. In contrast, here we are interested in studying a light field strongly interacting with an atom, a regime that can be achieved by enhancing the field amplitude by confining the light in a tight volume ($E_0 \sim V^{-1/2}$). The classical example is cavity quantum electrodynamics, whereby an atom is stored in a tightly focused and powerful light field that is created in an optical cavity (note that such a cavity operates in a contrasting way, unlike our build-up cavity discussed in Section 2.5 where the goal was to achieve the largest mode volume, and thus generate a large confining potential). In such systems, both atom and light field need to be treated quantum mechanically, enabling observations that are unseen in semi-classical scenarios such as vacuum-Rabi splitting and modified spontaneous emissions. However, the tight focus of light is diffraction limited in a vacuum to $V \sim \lambda^3$; thus, this

limitation has led to the development of the field of nanophotonics, wherein photons are confined within subwavelength nanostructures to surpass the diffraction limit. Moreover, these synthetic structures allow engineering photonic band structures, which researchers achieve by manufacturing specific geometries and periodicities of the light-guiding nanostructures. Numerous efforts over the last decade have been make to trap neutral atoms in the vicinity of these nanostructures and thus realize strongly coupled light-matter interfaces that support rich physics such as chiral quantum optics, sub/superradiant states, and directional emissions.

However, reaching strong coupling regimes requires placing the atoms within the evanescent fields of the structures at distances below $100\ \mathrm{nm}$. Therefore, stable trapping of atoms at such distances difficult even in 1D–because of surface forces that modify both trapping conditions and the atomic emission properties, thus extending such systems to 2D is even more difficult. In addition, the degree of control over the system parameters in nanophotonic systems is limited. Therefore, considerable attention is now being paid to simulating these phenomena using ultracold atoms, making atoms behave as photons do. These analog simulators based on ultracold atoms in optical lattices can simulate strongly coupled light-matter interfaces that are challenging or impossible to realize in real systems. Ultimately, these simulations can provide novel quantum matter that can be synthetically generated by engineering the long-range interactions between atoms, mediated by the atoms that mimic travelling photons.

Here, we are considering a nanophotonic system wherein two-level atoms, which we will call *quantum emitters* to distinguish them from the strontium clock states, are coupled strongly to a single band of a photonic bath. We next explain how the Hamiltonian of this nanophotonic system can be mapped to our analog simulator that uses the strontium clocks states in a state-dependent lattice created at a wavelength of λ_g. In our simulator, g is trapped in a shallow lattice, and therefore tunnels freely within the lattice, whereas e is tightly trapped as shown in Fig. 2.7(a). Then, a clock laser light focused to a particular lattice site can continuously drive coupling between g and e, with a coupling strength given by the Rabi frequency Ω. Multiple such clock laser lights can be added to address multiple lattice sites (Fig. 2.7(a)). In this case, $^3\mathrm{P}_0$ tightly trapped in a lattice site with the clock laser light shining directly on it acts as an emitter in the excited state (Fig. 2.7(b) left), which can *emit* a bath particle. In this quantum simulation, a bath particle corresponds to an atom in $^1\mathrm{S}_0$ in the shallow lattice (Fig. 2.7(b) middle). On the other hand, an empty lattice site with the clock laser light shining on it maps to an emitter in the ground state (Fig. 2.7(b) right), and can *absorb* a bath particle. This phenomenon would correspond to tunneling $^1\mathrm{S}_0$ arriving at this site and getting excited to $^3\mathrm{P}_0$ by the clock laser light.

To make an analogy with the band structures of nanophotonic systems, we also need to look at the resulting band structure of the state-dependent lattice. The dispersion relation of a 1D lattice using tight-binding approximation, allowing hopping only to neighboring

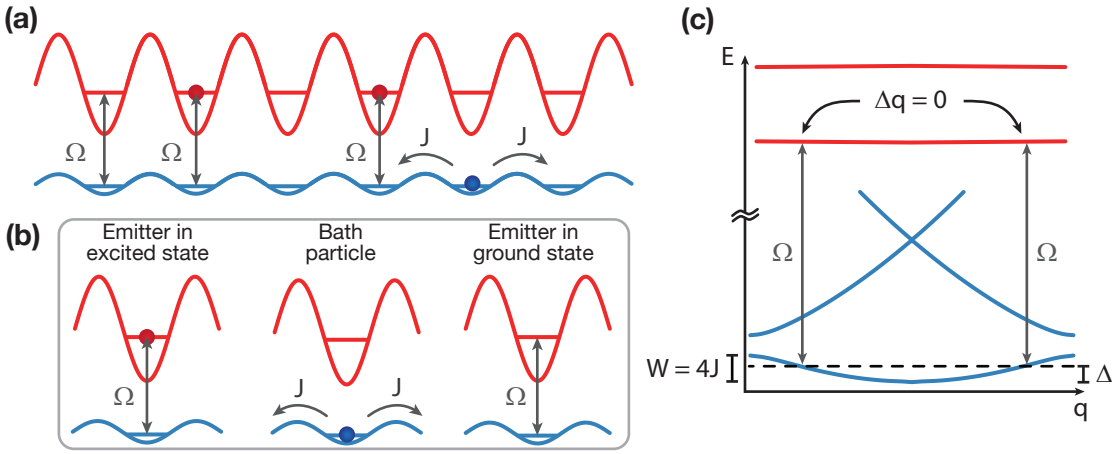

Figure 2.7 Simulation of nanophotonic physics (adapted from Ref. [82]). (a) Strontium clock states in a state-dependent lattice at a wavelength of λ_g. The ground state g (blue circle) tunnels in a shallow lattice, and the excited state e (red circle) is pinned in a deep lattice. The clock laser lights (vertical arrow) that selectively shine on a single lattice site couple g and e with a coupling strength Ω. (b) Mapping of quantum emitters coupled to a photonic bath to strontium clock states trapped in a state-dependent lattice. (c) Energy band structure of g (blue) and e (red) in the state-dependent lattice. The two bands are coupled by the clock laser light. By changing the detuning of the clock laser Δ, one can choose into which part of the band structure the quantum emitter will emit. Moreover, the g band structure is resolved when $\Omega \ll W$.

lattice sites, is given by $E(q) = -2J\cos(q)$, where $q \in [-\hbar k, \hbar k)$ is the quasimomentum with a wavevector k of the lattice, and $W = 4J$ is the bandwidth. Here, q is analogous to the momentum p and can be perceived as associated with the kinetic energy of an atom in the lattice. The derivation of the dispersion relation will not be discussed in this thesis but can be found in many textbooks, in particular, in Ref [99, 100]. For the excited state e that is trapped in the deep lattice, the band is flat since $J \sim 0$ ($W \sim 0$), whereas the band structure of g in the shallow lattice features the cosine structure. This difference between the two band structures is illustrated in Fig. 2.7(c). The non-flat band structure of the shallow g lattice is what is similar to the band structure of nanostructures such as photonic crystals. The two bands, g and e, can be coupled by the clock laser light at detuning Δ, i.e., an emitter coupled to a single band of the bath. The detuning Δ determines at which part of the band structure they couple (Fig. 2.7(c)) and thus also determine where in the band the emission will take place. Therefore, when $\Omega \ll W$, the bath's band structure can be resolved by tuning Δ. In addition, W and Ω can be tuned independently by changing the lattice depth and clock laser's intensity, respectively, to enter different coupling regimes. In particular, the strong coupling regime occurs at $W \sim \Omega$. Therefore, the ease of tuning Δ, W, and Ω in ultracold atom quantum simulators allow explorations of various parameter regimes.

The above simulations can be realized using either bosonic and fermionic isotopes, and the different isotopes of strontium enable a choice of bath interactions (Table 2.1). In particular, ^{88}Sr, with an almost vanishing scattering length of -2 a_0, can be used to realize a non-interacting bath particle that is the case most analogous case to photons that do not interact. Implementation using ^{87}Sr might require care so that Pauli's exclusion does not perturb the tunneling dynamics. This concern can partly be solved by having an equal population of the 10 different spin states of ^{87}Sr to reduce the probability of finding a bath particle with the same spin state at adjacent lattice sites.

Such simulations of nanophotonic physics have just begun, and the first demonstrations were performed using a rubidium-based quantum simulator in one dimension [19, 20, 101]. Our simulator using strontium atoms in a 2D state-dependent lattice with single-site imaging will expand the scope of what has been possible using a rubidium-based quantum simulator. It will allow observations of richer physics, enabled by the higher dimensionality of the lattices, and will feature higher fidelity quantum simulations that are enabled by both longer atomic lifetimes and single-site addressing and detection techniques. Moreover, our large cavity-enhanced lattices that extend more than 300 $\times$300 lattice sites will reduce particle reflections at the boundary that can hamper the directional emission patterns expected in such systems [32].

2.7.2 Collisional phase gates

There have been various proposals for quantum information processing that either use the nuclear states or electronic clock states of strontium as qubits, or even a hybrid scheme

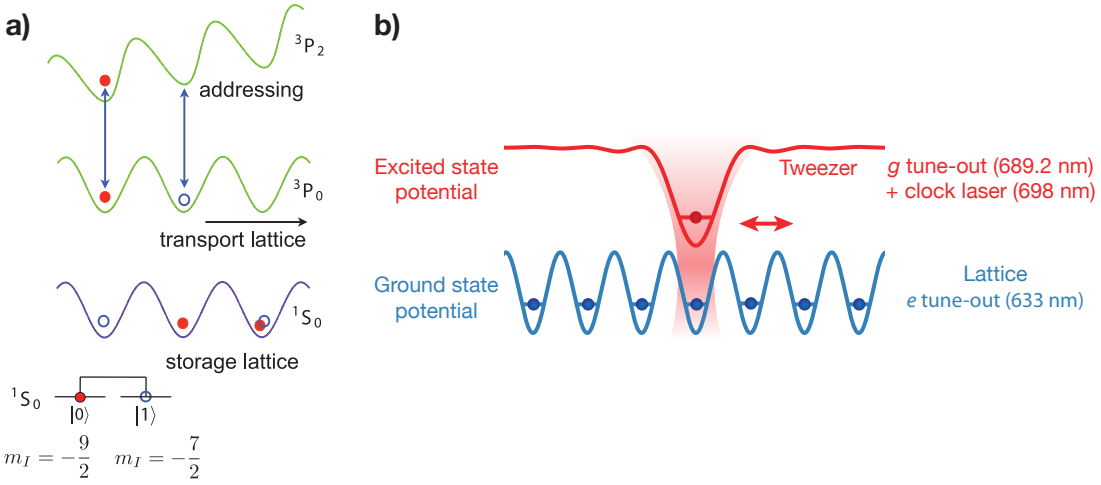

Figure 2.8 Collisional phase gates using strontium in state-dependent optical traps. (a) Qubits ($|0\rangle$ and $|1\rangle$) are realized using the nuclear spin states of $^1S_0$ and are stored in a storage lattice created at λ_e. Then, the qubits are moved to an independent transport lattice created at λ_g for gate operation between distant qubits. They can also be addressed individually by coupling to $^3P_2$, a level that is shifted by a magnetic field gradient (the figure is from Ref. [21]) (b) An alternative scheme to achieve collisional phase gates without having a transport lattice. Here, optical tweezers at λ_g and λ_{clk} are used to excite an atom to e and move them across a layer of g atoms.

that combines both nuclear spin and electronic degrees of freedom. Among these proposals, here, we briefly introduce the proposal of Ref. [21] which uses two nuclear states of $^1S_0$ of ^{87}Sr as qubits and performs an entangling gate via the electronic clock states in state-dependent lattices.

In this proposal, taking advantage of decoupling of the nuclear spin and the electronic state, qubits $|0\rangle$ and $|1\rangle$ are encoded in nuclear spin states m_I: $|0\rangle \equiv |^1S_0, m_I = -9/2\rangle$ and $|1\rangle \equiv |^1S_0, m_I = -7/2\rangle$. The atoms are subjected to two optical lattices operating at the e tune-out wavelength (λ_e =633 nm), forming a *storage lattice*, and at the g tune-out wavelength (λ_g =689.2 nm), forming a *transport lattice*. At these wavelengths, the storage lattice traps only $^1S_0$, and the transport lattice traps only $^3P_0$, as illustrated in Fig. 2.8(a). Here, the qubits are initialized and stored in the storage lattice. Then, one or many qubits can be excited to $^3P_0$ by a clock laser light in parallel to perform entangling gates. Once they are excited, they get trapped in the transport lattice, not in the storage lattice. Then, the lattice can be *transported* in a well-controlled way by introducing a frequency difference between the two counter-propagating beams that make up the lattice. Once the atoms are moved over by a fixed lattice site, the atoms in $^3P_0$ can interact with $^1S_0$ in the storage lattice via the on-site interaction, and this interaction can be used to implement a phase gate. Such type of gates that use on-site interaction are called *collisional phase gates*. The proposed way to achieve single-site addressing for read-out and

gate operations uses $^3P_2$, the state that is more sensitive to a magnetic field compared to the clock states, in the presence of a large external magnetic field gradient that shifts the energy spatially (Fig. 2.8(a)).

In our experiment, we cannot move the lattices since their frequency is stabilized to the build-up cavity's resonance frequency. Nevertheless, we can employ an alternative approach: combine laser beams at wavelengths of λ_g and clock transition (λ_{clk}=$698\ \text{nm}$) and send them through a quantum gas microscope to tightly focus these beams onto a single lattice site (i.e., optical tweezer). This idea is sketched in Fig. 2.8(b). Then, these focused beams can be multiplexed to shine on multiple lattice sites and also moved by using a spatial light modulator or acousto-optic deflector. In this way, the setup can excite g at the particular lattice sites to e atoms, and then, subsequently, move e atoms through the layer of g atoms, enabling the implementation of entangling gates.

Chapter 3

Production of ultracold strontium clouds

In the beginning of this thesis work, the project started in a laboratory with only empty optical tables present. Now, this laboratory has developed into a crowded place with a fully assembled vacuum chamber and the tables equipped with multiple laser systems necessary to cool, trap, and manipulate strontium atoms, as illustrated in Fig. 3.1. As we plan for the world's largest optical lattice quantum simulator, at which lattices extend up to $\sim 300 \times 300$ sites, significant efforts have gone into building an apparatus with a fast cycle time and large numbers of atoms. This chapter contains information about *the first part* of our experimental setup and sequence used to produce a ~ 1 μK-cold atomic cloud of ^{87}Sr and ^{88}Sr, which is the first essential step towards realizing all the interesting applications of our machine discussed in the previous chapter. We provide an overview of the vacuum system (Section 3.1), laser systems (Section 3.2), and optomechanics around the chamber (Section 3.3). Then, we describe our magneto-optical traps (MOT) (Section 3.4, 3.5, and 3.6); in particular, we discuss our improved narrow-line Red MOT technique in detail. This technique is based on adiabatic passage and provides a robust and quick pathway to creating ultracold strontium clouds with large numbers of atom number (Section 3.5).

3.1 Setup overview & vacuum system

Our experiment begins with producing a hot and high-velocity beam of strontium vapour from an oven, which subsequently gets localized and laser-cooled in MOTs. Then, the laser-cooled atoms are optically transported to be trapped in the cavity-enhanced optical lattices, where quantum simulation and high-resolution detection will take place. The vacuum chamber is L-shaped, as shown in Fig. 3.2, and can be conceptually divided into two parts: the *preparation* part for loading and production of ultracold samples and the *science* part for performing high-quality measurements and quantum simulations. The first part consists of an oven, transverse cooling, Zeeman slower and a *main chamber* where we create magneto-optical traps (MOT) for strontium atoms. The second part largely consists of another stainless steel chamber called the *science chamber,* where the crossed cavities are mounted. A vacuum chamber consisting of two different chambers, one for MOTs and the other for quantum simulations, is a common design choice in ultracold experiments, due to the limited space for placing optics; however, for us, this design was particularly important for the build-up cavity assembly. We wanted to avoid the atomic beam hitting the cavity assembly, which may cause possible deposition of

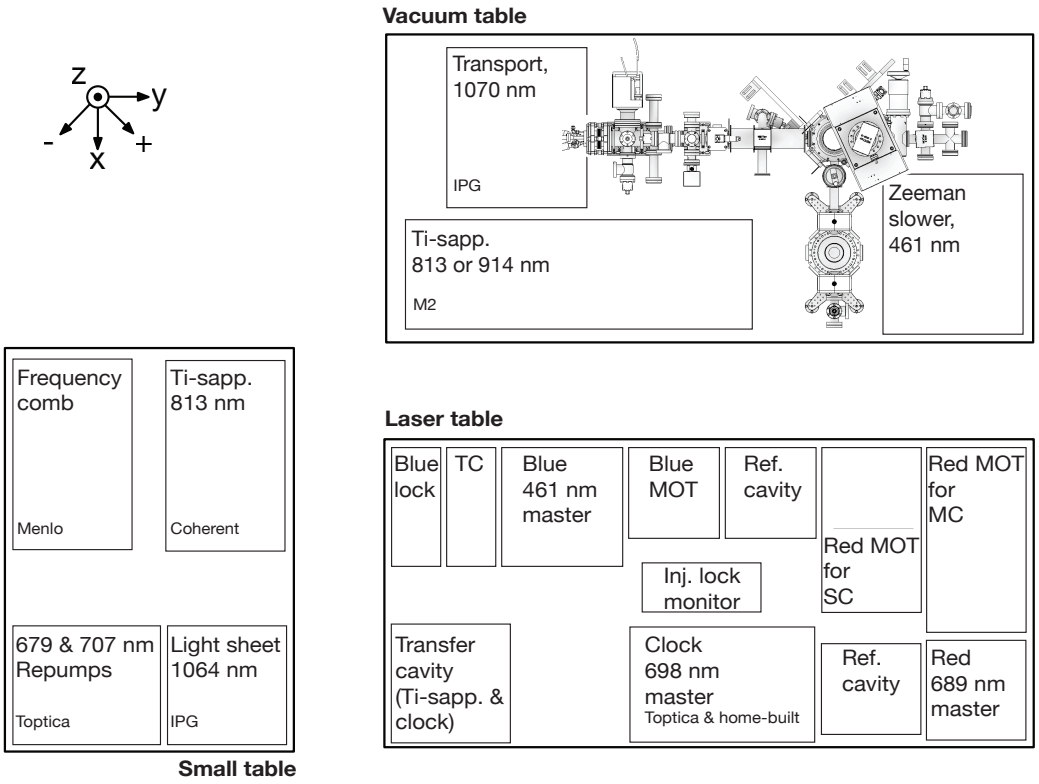

Figure 3.1 Overview of the lab space, showing a schematic of the vacuum system, all the laser systems used in this thesis, and the lab-frame. The abbreviations MC, SC, and Ti-sapp refer to the main chamber, science chamber, and Ti-sapphire laser, respectively.

strontium that could degrade cavity mirror coatings. In this chapter, we focus only on the first part, and the second part of the apparatus will be discussed in depth in Chapter 5. As the construction of the first part has been performed jointly with another PhD researcher who has already published his thesis [55], we will keep the summary brief as the details can be found in Ref. [55] and instead, focus on those that have not been discussed.

Oven

The experiment starts with hot strontium gas leaving the oven at high velocity. The higher the oven temperature, the higher the atomic flux is. For our machine, raising the temperature by $50\ ^\circ\mathrm{C}$ increases the atomic flux in the main chamber by a factor of 3. However, higher flux also reduces the oven's lifetime, leading to a hard trade-off between the two. To give a rough scaling for our machine, we find that loading the oven with $\sim 3\ \mathrm{g}$ of strontium has a lifetime of two years and $\sim$4 months when we run the oven at $500\ ^\circ\mathrm{C}$ and $600\ ^\circ\mathrm{C}$, respectively (assuming that the oven is running continuously every day). We heat up the oven to $500\ ^\circ\mathrm{C}$ or $550\ ^\circ\mathrm{C}$ for ^{88}Sr and ^{87}Sr, respectively. The higher operating temperature for ^{87}Sr compared to ^{88}Sr is not enough to compensate for the lower natural abundance of ^{87}Sr, which is about a factor of 10 lower than ^{88}Sr. However, we find that this increase is a good compromise between higher flux and the oven lifetime.

For the reasons we discussed above, an atomic beam oven sets a hard limit on achievable atomic flux for any quantum gas experiment, particularly for those atomic species with high melting points like strontium, erbium, and dysprosium. Although constructing an oven from scratch is doable, but for the species mentioned above, many research groups rely on commercial ovens from companies such as AOSense and CREATEC because developing a high flux atomic source is challenging. We are currently using an oven from CREATEC; however, because the oven was originally designed for molecular beam epitaxy, several features are not ideal for quantum gas experiments. For this reason, our lab has been developing a high-flux atomic beam source for future upgrades. The details are available from the Master's theses [102, 103].

First stage differential pumping tube

Due to the high temperature of the oven section, the pressure in the oven is relatively high ($\sim 10^{-8}$ at $500\ ^\circ\mathrm{C}$). Therefore, we install a differential pump tube after the oven section to prevent any contaminants from the oven section from affecting the main chamber. The tube is $120\ \mathrm{mm}$ long with a diameter of $5\ \mathrm{mm}$, providing an order of magnitude lower pressure.

Transverse cooling

We mentioned that a high atomic flux is important, but another crucial property is the collimation of an atomic beam. A highly diverging atomic beam with a small overlap with a counter-propagating laser beam that slows down the atoms is useless for cold atom

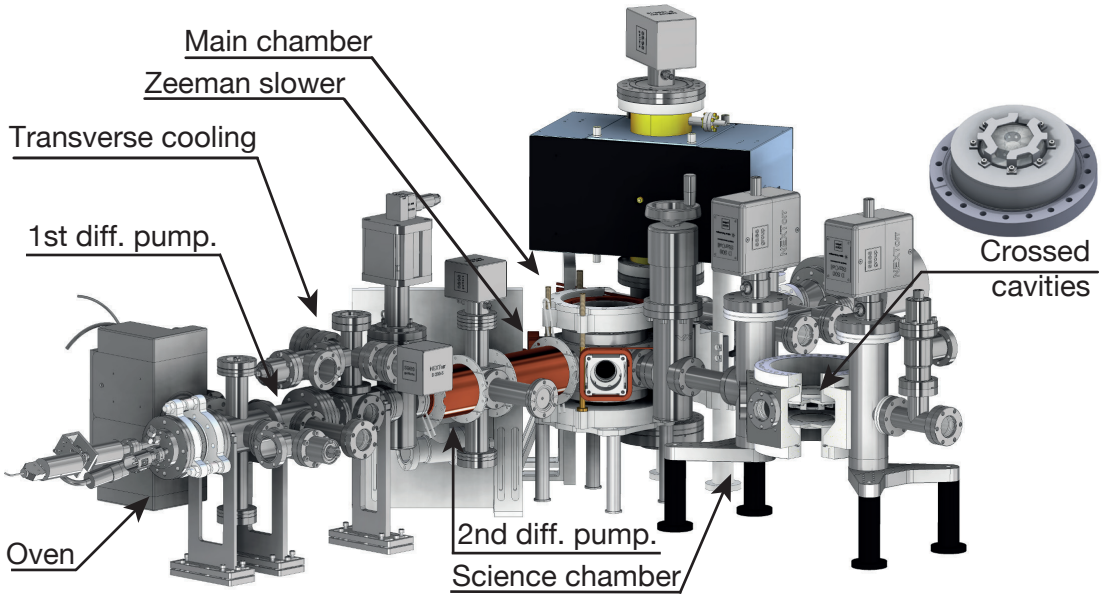

Figure 3.2 Overview of the vacuum system (modified from [55])

experiments. Therefore, to better collimate the hot atomic beam, we perform optical molasses in two orthogonal directions to reduce the atomic beam's transverse velocities. The cooling beam for each direction has a beam diameter of $\sim 4\ \mathrm{mm}$, and it crosses the atomic beam transversely several times. This beam path is achieved by retro-reflecting the cooling beam several times at a small angle between the two mirrors. The traverse cooling region improves the atomic flux by a factor of 2$\sim$3 for both ^{88}Sr and ^{87}Sr.

Zeeman Slower and second differential pumping tube

Our Zeeman slower section is about $\sim 40\ \mathrm{cm}$ long and has a configurable bitter-coil design. The magnetic coils are assembled surrounding two separate vacuum nipples, and one of the nipples has inner dimensions that are the same as the first differential pumping tube, thus acting as a second differential pumping stage. Therefore, this stage once further reduces the pressure. The slower section is designed to slow down the atoms to the capture velocity of the blue MOT, which is $\sim 30\ \mathrm{m/s}$. The laser light for the slower beam comes from the injection-locked blue diode from Nichia, that will be described further in the section describing the laser system (Section 3.2). We find that most of the slowing is done by the light, and the magnetic field has only a little influence. Having a magnetic field improves the flux only by $\sim$10%.

Main chamber

In this chamber, the slowed atoms are captured and laser-cooled down to a few μK via the two stages of MOT. The first stage uses the broad $^1S_0$- $^1P_1$ transition to cool the atoms

to ~ 1 mK, and the subsequent step uses the narrow $^1S_0$- $^3P_1$ transition to cool to a few μK. In this chamber, we measure a pressure of 2×10^{-10} mbar using a hot-wire vacuum gauge, and the atomic lifetime of 50 s in the $^3P_2$ magnetic trap. The details about the MOT setup is explained later in Section 3.4 and 3.5.

3.2 Laser Systems

The laser systems are distributed across three optical tables as already shown in Fig. 3.1, and the laser beams arrive to the vacuum system via optical fibers if the corresponding laser systems are not on the vacuum table. Every laser setup is built on a separate breadboard with side and top enclosures. In this way, we can rearrange the setups easily when necessary, and the optics are protected from dust.

The laser systems necessary for laser-cooling strontium are 461 nm, 689 nm, 679 nm, and 707 nm laser sources with the first two required for MOTs and the latter two required to optically repump the atoms back to $^1S_0$. The cooling steps will be discussed in detail later in Section 3.4 and 3.5. Before the laser beams are delivered to the vacuum chamber and are sent to interact with strontium atoms, the laser beams first need to be prepared with correct detuning and power, and most of these initial preparations are done on the laser table.

In general, many cold atom experiments face difficulty due to limited laser beam power and laboratory space compared to the space needed for the laser systems. Moreover, it is often the case that the laser system needs to be extended as an experiment develops further. For this reason, we have designed most of the laser systems to be scalable in power using compact custom-built injection lock modules. A typical laser set-up starts with a master laser whose frequency is stabilized to a stable reference cavity or a spectroscopy cell. Split-off beams from the master laser can seed multiple injection lock modules to amplify the beam power, and we find that little seed beam power is required, ~ 2 mW. Therefore, in this way, we can get more power by simply adding more injection lock modules when necessary.

3.2.1 Blue laser system

The blue beam initiates the laser-cooling of strontium atoms using the broad $^1S_0$-$^3P_1$ transition, and the laser setup is designed to address the $^1S_0$-$^3P_1$ transition of all naturally occurring isotopes. Moreover, the blue beams are also used as probe beams for absorption imaging. A master laser, Toptica's DL Pro, is frequency stabilized to a spectroscopy cell using a frequency modulation transfer technique [104]. The design of the spectroscopy cell is adapted from Ref. [61]. We use acousto-optical modulators (AOMs) to tune the frequency of the laser to lock to an isotope of interest. The master laser beam is split into multiple beam paths for frequency stabilization to the spectroscopy cell, absorption

imaging in the main and science chambers, and seeding multiple injection modules for preparing the transverse cooling, Zeeman slower, and MOT beams. All the necessary frequency shiftings of the beams is done using AOMs, and the detailed beam paths are available in [55].

3.2.2 Red laser system

The red laser setup has a similar design as the blue laser setup in that it consists of a master laser and a slave laser that is locked to the master laser's frequency by injection lock (although we initially used tapered amplifiers, as will be explained later). However, one major difference is the laser's frequency stabilization method. Compared to the blue laser setup, the requirement on the laser's frequency stability is far more stringent for the red laser, since it is used to address the transition with a linewidth of only $7.4\ \mathrm{kHz}$. This linewidth is more than three orders of magnitude narrower than the blue transition and also much narrower than a typical linewidth of free running external-cavity diode lasers of $\sim$100 kHz; Therefore, the red master laser has to be frequency-tuned to drive the correct atomic transition of strontium, but also the linewidth has to be reduced by stabilizing its frequency to a resonance of an ultrastable high-finesse reference cavity. The red laser setup consists of three major parts: the master laser, frequency stabilization setup to the reference cavity, and slave laser.

Master laser setup

The main role of the master laser is to split off its power to generate the beam paths used for different purposes, just as was done for the blue laser setup. Therefore, it is important to stabilize the master laser's frequency at the most convenient frequency that can easily meet the frequency requirements of different beam paths. For this, let us first look at what different beam paths are and discuss the laser's locking frequency we chose to satisfy all the frequency requirements of different beam paths.

The master laser, DL Pro from Toptica, outputs about $28\ \mathrm{mW}$ of power, and after beam shaping with a pair of cylindrical lenses, its beam path is divided into five different paths as shown in Fig. 3.3. First, we split off the beam to couple to a wavemeter to measure the laser's frequency (Path 1 in Fig. 3.3). With the wavemeter, we can set the frequency of the master laser as close to the desired frequency within roughly a few hundred MHz. The second split off is used to couple the light to the reference cavity to stabilize the laser's frequency to the cavity's resonance frequency (Path 2 in Fig. 3.3). The third path is dedicated to seed a slave laser by injection locking, and the seed laser is primarily used for the red MOT beams (Path 3 in Fig. 3.3). Therefore, depending on whether the laser is used to address ^{88}Sr or ^{87}Sr, one may want to tune the frequency appropriately before seeding, rather than in the slave laser setup, to save the beam power.

Let us now discuss the target transition frequencies for the red MOT. To operate the red MOT for ^{88}Sr and ^{87}Sr, we need the beams that address the $^1S_0$-$^3P_1$ transition of ^{88}Sr,

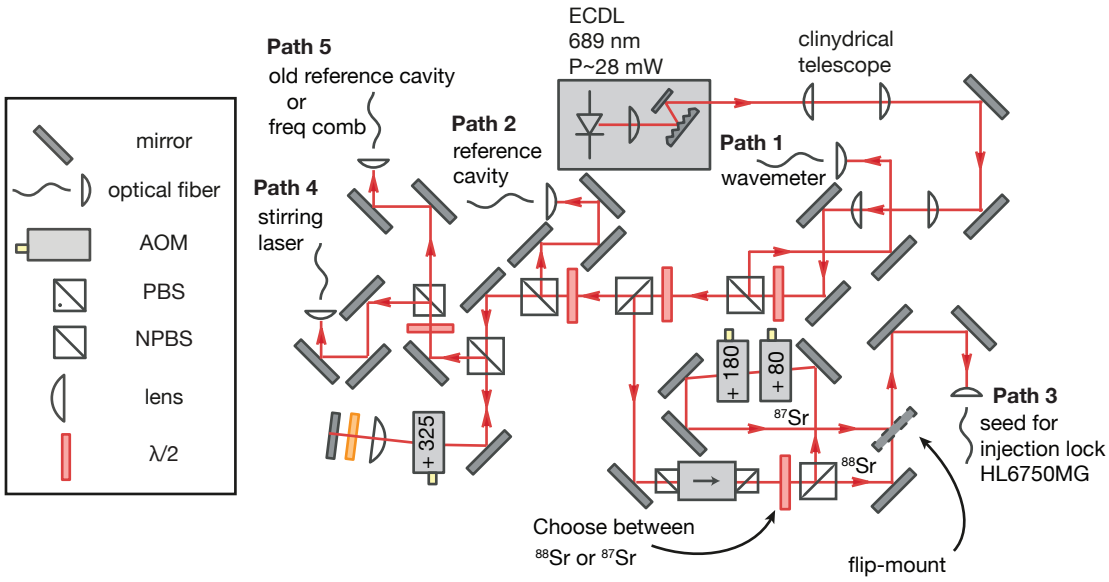

Figure 3.3 Overview of the red master laser system. The beam path from the master laser, Toptica's DL Pro, is splitted into five paths: to a wavemeter (Path 1), to lock to the reference (Path 2), to seed an injection lock module (Path 3), to be used as a stirring laser beam (Path 4), to beat with a femtosecond optical frequency comb (Path 5)

and ^{1}S$_0$ ($F = 9/2$)-^{3}P$_1$ ($F' = 11/2$) and ^{1}S$_0$ ($F = 9/2$)-^{3}P$_1$ ($F' = 9/2$) of ^{87}Sr transitions (Section 2.2), respectively. In Figure 2.2 in Section 2.2, we have shown the detunings of the ^{1}S$_0$-^{3}P$_1$ hyperfine structures with respect to the state assuming $I = 0$; however, here, the more useful numbers are the detunings from the ^{1}S$_0$-^{3}P$_1$ transition of ^{88}Sr, taking account the isotope shift of $62.1865(123)$ MHz [105], which is shown in Table 3.1. As shown in the Table 3.1, the difference in ^{88}Sr ^{1}S$_0$-^{3}P$_1$ and ^{87}Sr ^{1}S$_0$ ($F = 9/2$)-^{3}P$_1$ ($F' = 11/2$) is more than 1 GHz. Although this gap can certainly be bridged using AOMs or EOMs, instead, we change the locking frequency of the master laser depending on the isotope of interest to ease bridging the gap. More explicitly, we use the fact that we can lock the laser to the fundamental transverse mode (TEM$_{00}$) of the reference cavity at every free spectral range, which is 1.5 GHz in our case.

Isotope	F'	^{1}S$_0 \rightarrow {}^1$P$_1$ (MHz)	^{1}S$_0 \rightarrow {}^3$P$_1$ (MHz)
^{88}Sr		0	0
	$7/2$	-9.7	1352.0
^{87}Sr	$9/2$	-68.9	-221.7
	$11/2$	-51.6	-1241.4

Table 3.1 The detuning from the ^{88}Sr transitions to address the different hyperfine states of ^{87}Sr [37].

Frequency tuning to address the $^1S_0$-$^3P_1$ transition of ^{88}Sr For cooling ^{88}Sr, we lock the frequency of the laser $80\ \mathrm{MHz}$ above the ^{1}S$_0$-^{3}P$_1$ transition. The reason for the $80\ \mathrm{MHz}$ offset is related to the later stage of the setup. In a nutshell, it allows us to have one double-pass AOM ($\sim$-2$\times$80 MHz) for shifting the frequency of all three red MOT beams and a single-pass AOM ($\times 80\ \mathrm{MHz}$) to individually shut off each red MOT beam.

To achieve this frequency stabilization, we first roughly put the laser to the transition frequency by looking at the wavemeter and then, beat the laser with a femtosecond optical frequency comb to find out the absolute frequency (Path 5 in Fig. 3.3). Then, we find the cavity resonance of the TEM$_{00}$ mode that is as close to our desired frequency. Since the cavity length is not tunable, and a free spectral range of the cavity is $1.5\ \mathrm{GHz}$, the maximum frequency tuning required to match the frequency of the atomic transition to the cavity resonance is $\pm 750\ \mathrm{MHz}$. Therefore, ideally one should put an AOM in Path 2 in Fig. 3.3 to match the two frequencies. In fact, for our first-generation of the reference cavity, we had to tune the beam's frequency by $\pm 625\ \mathrm{MHz}$. However, for our second version of the cavity, which is the one we are currently using, the required frequency tuning range was small such that it can be done by shifting other AOMs in the later stage of the setup by a few MHz. Therefore, the beam couples directly to the cavity without any frequency shifters.

Once the master laser's frequency is locked to the TEM$_{00}$ using a Pound–Drever–Hall (PDH) locking scheme, to deliver the the seed beam that is $80\ \mathrm{MHz}$ detuned from the ^{1}S$_0$-^{3}P$_1$ transition to the injection lock module, the mirror mounted on a removable flip-mount in Path 3 shown in Fig. 3.3 to be removed to fiber-couple the light.

Frequency tuning to address the $^1S_0$-$^3P_1$ hyperfine states of ^{87}Sr For ^{87}Sr, we lock the laser to the resonance of the cavity's TEM$_{00}$ mode, but to the one that is a free spectral range ($\sim$1.5 GHz) below. In doing so, the master is laser is only $-180\ \mathrm{MHz}$ detuned from the ^{1}S$_0$ ($F = 9/2$) and ^{3}P$_1$ ($F' = 11/2$) transition. We note that our strategy does not allow simultaneous cooling of ^{88}Sr and ^{87}Sr, but reduces the numbers of AOMs necessary to address the ^{87}Sr MOT transition (or EOM can be used to shift the frequency as well). The reduction of number of AOMs was particularly crucial during the early stages of our experiment when we had to secure $10\ \mathrm{mW}$ of the beam power to seed a tampered amplifier that amplified the laser power such that we have enough power for the red MOT beams.

To deliver the seed beam to the injection lock module in Path 3, the waveplate's setting has to be changed such that all the beams reflect from the PBS, thus all the beam power directs to the path with two single pass AOMs (Fig. 3.3). These two AOMs shift the frequency such that the seed beam is once again at $80\ \mathrm{MHz}$ above the ^{1}S$_0$ ($F = 9/2$) and ^{3}P$_1$ ($F' = 11/2$) transition.

Let us next talk about Path 4 and 5. Both paths get shifted by $625\ \mathrm{MHz}$ by the same double-pass AOM. Path 5 was initially designed as the beam path to lock to the old refer-

ence cavity that required a frequency shift of 625 MHz to match the cavity resonance and atomic transition. Therefore, the thought was to split off a part of this frequency shifted beam (Path 4) to prepare for the stirring laser beam that addresses $^1S_0$ ($F = 9/2$)-$^3P_1$ ($F = 9/2$) transition, which is $\sim$1 GHz detuned from the $^1S_0$ ($F = 9/2$)-$^3P_1$ ($F = 11/2$) transition (Table 3.1). This beam needs additional frequency shifts to reach the desired detuning, and these additional shifts are done in a separate breadboard which will be discussed later. Currently, a laser beam from path 5 is fiber coupled to the beat with a femtosecond optical frequency comb, which is very useful for determining the shift of the cavity resonance that occurs due to the shrinkage of the cavity spacer.

Master laser's frequency stabilization to a ultra-stable reference cavity

A great choice for reducing a laser's linewidth is by stabilizing its frequency to a high-finesse optical cavity. When the cavity mirrors are manufactured with the desired coating specifications, a cavity resonance's linewidth can be very narrow, thus transmitting light with a narrow frequency band (although this band repeats every free spectral range). Moreover, when the cavities are placed in the correct environment [106], the cavity length, which is inversely proportional to the cavity's resonance frequency, can be maintained stably. For these reasons, the cavity resonance frequency serves as a good frequency reference. For instance, we expect that locking the master laser's frequency to a resonance of the TEM_{00} mode of our reference cavity would allow reaching a linewidth $\sim$1 Hz, given that all the known cavity lock systemics [107] are taken care of. Our cavity assembly consists of a commercial notched cavity from Stable Laser Systems (ATF-4020-4) that has a linewidth 5.4 kHz (finesse of 280000), enclosed in a custom-made cavity housing. The details about our housing, the cavity assembly, and frequency stabilization scheme which is done using the PDH scheme are available from [108, 109]. Currently, the best laser linewidth we have observed with our setup is $\sim$4 Hz [109]. Reaching several 1 Hz laser linewidths is not necessary for operating the red MOT; however, we use a cavity with such a high finesse as we plan to also frequency stabilize the clock laser, which is only 9 nm away from the red transition, to the same reference cavity.

The red 689 nm laser injection module

Unfortunately, the sources for amplifying the laser beam at 689 nm are few. Back in 2015, we were excited to hear about the availability of 689 nm tapered amplifiers (TAs) from Eagleyard that output 500 mW with a seed power of $\geq$10 mW. However, the highest fiber coupling efficiency we could get was only 50 %, and we found that the beam power degrades over time. Over the course of 1.5 years, we observed a power degradation from 180 mW to 80 mW when operating the TA at 0.9 A, which is slightly below the maximum current of 1 A. Therefore, we decided to try injection locking cheap laser diodes from Thorlabs as an alternative, and we were happily surprised.

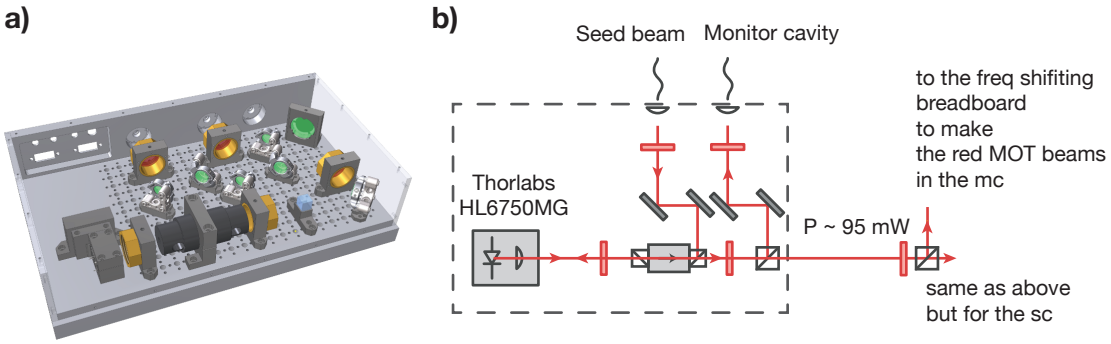

Figure 3.4 The red laser injection lock module. (a) An illustration of our compact and stable injection lock module. The module consists of three fiber coupling ports: for seeding, for monitoring the lock, and for experiments. The third fiber port is often replaced with a window to use the beam in free space. (b) Beam path for injection locking. The slave diode is HL6750MG from Thorlabs and outputs $\sim 95\ \mathrm{mW}$ of power after an optical isolator. Afterwards, the beam's power is split for making the red MOT beams for the red MOT in the main chamber (MC) and for making optical molasses beams for cooling in the science chamber (SC)

We tried two diodes from Thorlabs: HL6738MG and HL6750MG. They cost only 47 € and 77 €, respectively, whereas a typical price for a TA is 2,000 €. The diode HL6738MG behaved as expected, similar to that described in the specification sheet. It outputs $\sim 30\ \mathrm{mW}$, with a central frequency only about $1\ \mathrm{nm}$ away from $689\ \mathrm{nm}$ at room temperature. To get more power, we tried HL6750MG. According to the specification sheet, we expected that we would have to heat up the diode to $50\ ^{\circ}\mathrm{C}$ to get $50\ \mathrm{mW}$ of power at wavelength close to at a wavelength of $689\ \mathrm{nm}$. However, we found that the diode outputs $94\ \mathrm{mW}$ after an isolator ($\sim 90\ \%$ transmission) when operating at $112\ \mathrm{mA}$, close to the maximum current rating of $120\ \mathrm{mA}$, and has a center wavelength $687\ \mathrm{nm}$ at room temperature. The beam shape also looks reasonable, other than it being elliptical, which can be easily fixed using a cylindrical telescope. After beam shaping, a coupling efficiency to a fiber of $\sim 70\ \%$ can be achieved. Our first setup worked stably for up to two years until the diode broke. As the diode is cheap and the setup is simple, replacing the diode can be done in a few hours. However, unfortunately, the next two diodes broke within three months. We are not sure what the problems were, but these two problematic diodes were ordered at the same time. A further diode, received from a different order, has been working well for a year. Therefore, the diodes' long term reliability may need further examination. Despite this, the injection lock setup is far more attractive than tapered amplifiers due to its simple design that does not require water cooling, and its inexpensive price. Moreover, there currently are commercial lasers at $689\ \mathrm{nm}$ based on the same injection-locked diode from Moglabs.

The output of the injection locked slave laser shown in Fig. 3.4(b) is split into two paths using a waveplate and a polarizing beam-splitter, and the two paths are fiber-coupled to

the beam paths. One path shifts the frequencies for the red MOT beams for the main chamber and the other path for optical molasses beams for cooling in the science chamber (Chapter 5). Since the atoms transported to the science chamber are only $\sim 10\ \mu$K cold, performing optical molasses in the science chamber needs significantly less beam power than that needed for operating the red MOT in the main chamber. Therefore, we send most of the beam's power to the setup for the red MOT beams.

Frequency shifting for the red MOT beams

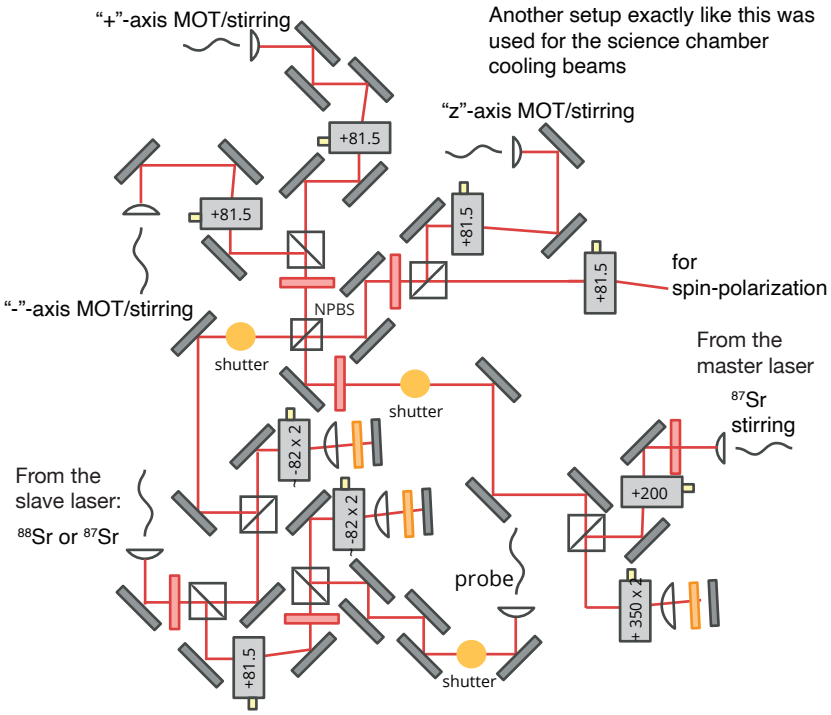

Figure 3.5 Overview of the frequency shifting of the red slave laser system. The double-pass AOMs used to modulate the beam's frequency, and the single pass AOMs are used turn on and off individual red MOT beams. The red MOT and stirring beams are merged using non-polarizing beam splitter.

So far, we have discussed how to amplify the beam's power and tune each beam's frequency to address the correct atomic transitions. However, apart from shifting the laser frequencies to the atomic transitions, we also need to modulate and ramp up the beam's frequency for the operation of the red MOT to respectively artificially increase the capture velocity and to compress the atoms in the single frequency red MOT. Moreover, we wanted the capability to turn on and off each beam independently to implement our new cooling technique, described later. In addition, for cooling ^{87}Sr, we need to merge the red MOT and stirring beams. In this section, we describe the optical setup for the Red MOT and stirring beams that achieves all the aforementioned requirements.

We first focus on the setup for ^{88}Sr, where the cooling is simpler than that for ^{87}Sr due to the absence of hyperfine structures. The basic setup starts from the beam derived from the injection lock module and the schematic of the beam paths is shown in Fig. 3.5. The beam is first split into two using a waveplate and polarizing beam-splitter cube, making beam paths for the red MOT and probe beams. The beam for the red MOT passes a double pass $\sim 80\ \mathrm{MHz}$ AOM, which is used to globally shift the frequency of all three $+, -, z$-axes of the MOT beams. Then, the beam is split into four, and three of them are used to realize $+, -$, and z-axis MOT beams. Each beam passes through another single-pass $\sim 80\ \mathrm{MHz}$ AOM. The AOMs in front of each beam allow us to switch on and off the beams of different axes independently, which is crucial for realizing the cooling technique explained later. Then, all three beams are fiber coupled to the MOT breadboards (Fig. 3.6) placed on the vacuum table. The fourth beam after the beam splitter can be used for spin polarization or as an additional probe beam. Note that the exact frequencies of these AOM frequencies are not exactly at $80\ \mathrm{MHz}$, because they drift as the cavity resonance's slow drift due to the length shrinkage.

Since the double pass AOM is used to modulate the frequency, it is important to optimize the bandwidth of the double-pass AOM. For this reason, it is also ideal to make the beam path from the double pass AOM to the fiber couplers as short as possible. The distance we have in between the two is about $\sim 50\ \mathrm{cm}$, and we can sweep the double-pass AOM up to $10\ \mathrm{MHz}$ (which means $20\ \mathrm{MHz}$ in laser frequency) while keeping the beam power at the MOT breadboard within $90\ \%$.

For ^{87}Sr, a stirring laser beam source derived from the master laser setup is frequency shifted further by single and double pass AOMs. We use this double-pass AOM to tune the frequency of the beam close to the transition. The stirring beam is then merged with the red MOT beam using a non-polarizing beam splitter. Therefore, like the red MOT beams, the stirring beam is also split into four, with three of them being coupled to the MOT breadboards in the vacuum table. We have about $\sim 200\ \mu\mathrm{W}$ of stirring beam for each axis. In principle, the power of the stirring beam can also be amplified using another injection lock module.

3.2.3 Repump laser system

Both $679\ \mathrm{nm}$ and $707\ \mathrm{nm}$ repump lasers are derived from Toptica DL Pro diode lasers. We do not lock the lasers to the transition, but let each run free run at the transition frequencies of $^3\mathrm{P}_0$-$^3\mathrm{S}_1$ and $^3\mathrm{P}_2$-$^3\mathrm{S}_1$, respectively. We tuned the frequency of the lasers to the ones that maximize the fluorescence of the steady state blue MOT signals. For operating the red MOT for ^{87}Sr at which the $^3\mathrm{P}_2$-$^3\mathrm{S}_1$ transitions split into many different hyperfine transitions, we periodically modulate the frequency of the $707\ \mathrm{nm}$ laser by scanning the piezo that changes the laser's cavity length.

3.3 Optomechanics near the main chamber

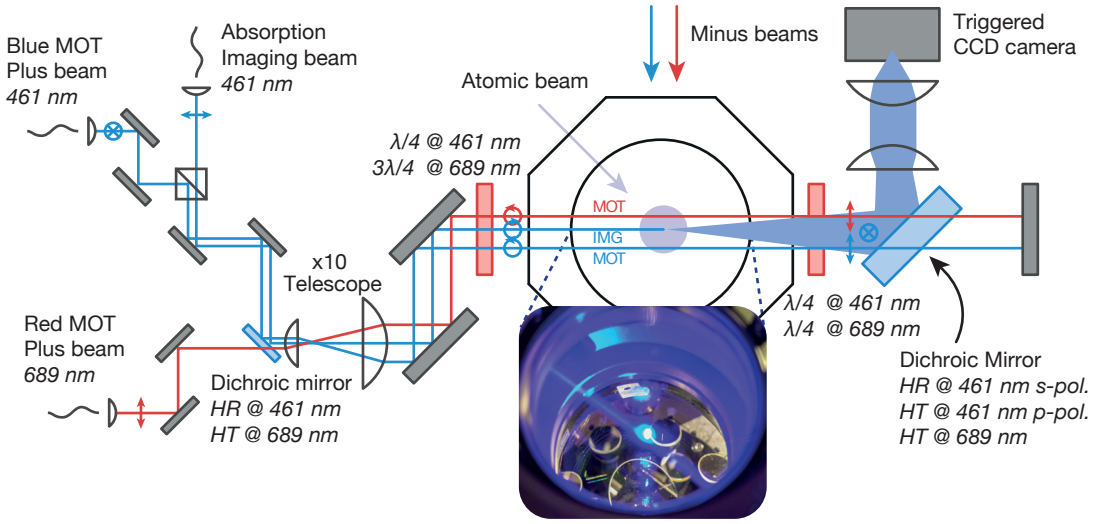

Figure 3.6 Illustration of the blue and red MOT beam setup near the main chamber (taken from [55]). The blue and red MOT beams are merged using a dichroic mirror and expanded together using a $\times 10$. The custom-made dual-wavelength waveplates are used to set the correct polarizations for both MOT beams. The dichoric mirror that is polarization-dependent for blue in the imaging path.

To achieve the two-stages of MOT, we merged both the blue and red MOT optics required for one axis into a single breadboard. A schematic sketch of the MOT beam paths is shown in Fig. 3.6. Let us briefly discuss the optomechanics of the MOT breadboards. The main chamber is surrounded by two vertical breadboards with a horizontal one on top, each having the optics for the horizontal ($+$ and $-$ axes) and vertical (z) red and blue MOT beams, respectively. For a compact and stable design, we chose a vertical breadboard that is $300\ \mathrm{mm}$ wide, $390\ \mathrm{mm}$ high, and $20\ \mathrm{mm}$ thick. On this breadboard, we merge three beam paths: the red MOT, blue MOT, and blue imaging probe beams. To fit all the optics and to produce the large blue and red MOT beams of $12\ \mathrm{mm}$ and $6\ \mathrm{mm}$ in diameter, respectively, we use a mix of optics with different sizes. Initially, we keep the beams relatively small such that we can use 1/2 or 1 inch optics, and merge blue and red MOT beams using a dichroic mirror. Then, we magnify all the beams at once using Thorlab's $10\times$ Galilean beam expander (Fig. 3.6). Moreover, we use Thorlab's 1/2 inch Polaris mirror mounts to be both compact and stable. The appropriate polarization configurations for the blue and red MOT beams are achieved by the custom-made dual wavelength waveplates. The optics on the top breadboard are exactly the same as the ones on the vertical breadboard except for an additional repump beam path and much less spatial constraint. We find that the MOT setup is very stable, and we do not need to re-align the MOT beams for years. What drifts are the beam powers due to the drifts of

the fiber-coupling efficiencies between the fiber ports on the MOT breadboards and ones on the laser table.

3.4 Loading to the $^3P_2$ Magnetic Reservoir

We explain our experimental sequence for the two stages of the MOTs, the blue and red, in detail. *For the convenience of the notation, we use a coordinate system (X,Y,Z) which correspond to (+,-,z) of the lab coordinate introduced in Fig. 3.1.* After the atoms are slowed by the Zeeman slower, we localize and cool the atoms by operating the blue MOT on the $^1S_0$-$^1P_1$ transition. For the blue MOT, we use three retroreflected laser beams at $460.86\,\mathrm{nm}$ with powers of ($6\,\mathrm{mW}$, $6\,\mathrm{mW}$, $4\,\mathrm{mW}$) along the (X, Y, Z) axes and $1/e^2$-waists of $6\,\mathrm{mm}$. A pair of anti-Helmholtz coils provides the magnetic quadrupole field $B(\rho, z) = B'\sqrt{\rho^2/4 + z^2}$ for the MOT, with a gradient $B' = 63.7\,\mathrm{G/cm}$ ($B'/2$), with respect to the axial (transverse) coordinate z ($\rho = \sqrt{x^2 + y^2}$). The blue MOT cools the atoms down to $\sim$1 mK, limited by the Doppler cooling limit of $T_D = \hbar\Gamma_{\mathrm{blue}}/(2k_B) = 0.7\,\mathrm{mK}$. Here, $2\pi\hbar = h$ is Planck's constant and k_B is Boltzmann's constant. While operating the blue MOT, the atoms leak to the $^1D_2$ state and decay into $^3P_2$ or $^3P_1$ states. The atoms that decayed to the metastable $^3P_2$ atoms are then stored in a magnetic trap [64, 37] created by the magnetic gradient of the MOT coils, whereas the $^3P_1$ states decay back to $^1S_0$ with a rate of $\Gamma = 2\pi\times7.4\,\mathrm{kHz}$ and goes back to the blue MOT cooling process. We let atoms accumulate as the metastable $^3P_2$ atoms in the magnetic trap, where the atoms are trapped in the linear potential $U(\rho, z) = g(^3P_2)m(^3P_2)\mu_B B(\rho, z)$, and an exponentially decaying density profile. Here, $g(^3P_2) = 3/2$ is the magnetic g-factor of the $^3P_2$ state, $m(^3P_2)$ is the magnetic quantum number, and μ_B is the Bohr magneton. The density profile for the bosonic isotope ^{88}Sr thus depends on the relative occupation of the magnetic sublevels $|m| = 1$ and 2. The hyperfine structure due to the large nuclear spin ($I = 9/2$) in the fermionic isotope ^{87}Sr complicates predictions of the density profile further. Compared to ^{88}Sr, the five hyperfine states have different and much smaller g-factors, which lead to a more extended and less tightly trapped atomic cloud. In principle, the loading rate to the magnetic trap can be enhanced by repumping the $^3P_1$ states to the $^3S_1$ states as well [110].

The atom number in the magnetic trap saturates when the gain by loading from the atomic beam balances the loss due to collisions with the atomic beam. For our system, we find a corresponding $1/e$ magnetic trap lifetime of $24\,\mathrm{s}$ ($16\,\mathrm{s}$) for bosonic ^{88}Sr (fermionic ^{87}Sr) at an oven temperature of $600\,^\circ\mathrm{C}$. With the atomic shutter closed, we measure $1/e$ magnetic lifetime of $50\,\mathrm{s}$ for ^{88}Sr irrespective of the oven temperature. After $3\,\mathrm{s}$ of loading, we shine the repump lasers for $10\,\mathrm{ms}$ to the sample to transfer the atoms back to the $^1S_0$ ground state. For this purpose, we use two lasers that operate on the $^3P_2$-$^3S_1$ and $^3P_0$-$^3S_1$ transitions at $707\,\mathrm{nm}$ and $679\,\mathrm{nm}$, respectively. The repump pulse transfers atoms to the $^3P_1$ state, from which they decay with a lifetime of $\tau = 21.28(3)\,\mu\mathrm{s}$ [56] back to the $^1S_0$ ground state. For the laser intensities and magnetic fields used here, the

$^1S_0$ state population is refilled with a $1/e$-time of $1.3(1)$ ms. In the spinless electronic ground state, the atoms experience almost no magnetic force and start to expand freely.

To further cool the atoms to the μK regime, they need to be captured in a secondary narrow-line magneto-optical trap ("red MOT") operating on the $^1S_0$-$^3P_1$ transition at $\lambda \simeq 689.4$ nm with linewidth $\Gamma = 1/\tau = 2\pi \times 7.48(1)$ kHz. The large discrepancy between red and blue transition linewidths makes it necessary to significantly broaden the linewidth of the red MOT laser to prevent atom loss: The Doppler-broadened linewidth $\Delta\omega_D = 2\pi \times \sqrt{4\hbar\Gamma_{\text{blue}} \ln 2/(m\lambda^2)} \simeq 2\pi \times 0.9$ MHz is ~120 times larger than Γ. Furthermore, spatially confining atoms in a magneto-optical trap for the $^1S_0$-$^3P_1$ transition requires a magnetic quadrupole field with typical axial gradients B' of a few G/cm [64, 49, 63, 37]. This order-of-magnitude reduction in magnetic field compared to the blue MOT has to be achieved on timescales comparable to the $^1S_0$ refilling time to prevent atoms from escaping due to their per-axis atomic root-mean-square velocity ~ 0.25 mm/ms. For this reason, we switch the field gradient diabatically and we find a typical Zeeman shift of several MHz on the red MOT transition.

3.5 The Red MOT using saw-tooth adiabatic passage

The traditional strategy to overcome such large Doppler and Zeeman shifts is to frequency-modulate the red MOT laser at a modulation frequency f_{mod} over a period $t_{\text{sweep}} = 1/f_{\text{mod}}$. The resulting laser spectrum is a comb of frequencies spaced by f_{mod}, and care has to be taken to find a balance between modulation speed and power-broadened linewidth. Traditionally, the resulting cooling process has been explained in terms of Doppler cooling with a modified laser spectrum. However, in this section, we present our improved Red MOT sequence based on the recently-developed sawtooth-wave-adiabatic-passage (SWAP) technique [66–69].

We first describe the basics of SWAP molasses cooling and extend this idea to the SWAP MOT model. Then, we show that even the traditional approach is more usefully described in terms of adiabatic rapid passage processes, because optimal sweep times are comparable to the atomic lifetime τ [64, 49, 63, 37]. Lastly, we present our experimental sequence and results of the performance of the SWAP MOT.

3.5.1 Optical molasses using sawtooth-wave adiabatic passage

In this section, we will explain the working principle of optical molasses via sawtooth-wave adiabatic passage [66, 68]. Here, we consider the simplest case where a two-level atom with internal ground g and long-lived excited e states that moves in one dimension with velocity v and is subjected to co- and counter-propagating laser beams as shown in Fig. 3.7. To initiate the cooling, the frequency ω of the two beams is linearly swept across the resonance frequency of the $g - e$ transition ω_{eg} in a sawtooth pattern in time

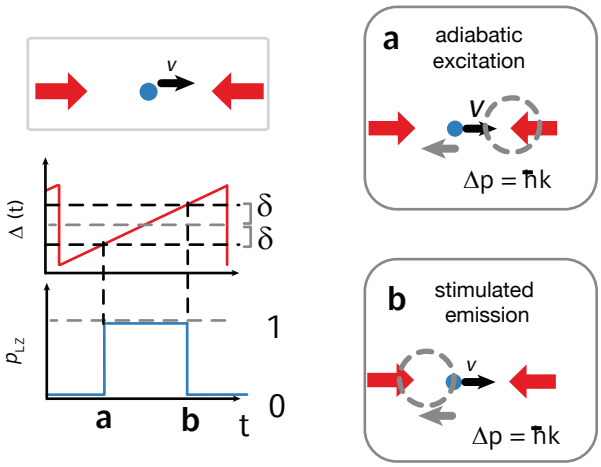

Figure 3.7 Illustration of working principle of optical molasses via sawtooth-wave adiabatic passage. The atom first interacts with a counter-propagating beam, getting a momentum kick in an opposite direction of its motion. The atom subsequently undergoes stimulated emission due to the co-propagating beam., resulting in another instance of the same momentum kick.

with a duty cycle t_{cycle}. In Fig. 3.7, we show this frequency sweep pattern where the y-axis is shown as a function of the detuning Δ from the free space resonant frequency ω_{eg}. Each laser beam interacts with an atom, giving a momentum kick $\hbar k$, but the two beams interact with the atom at different times. The non-zero velocity of the atom induces a Doppler shift kv in the reference frame of the atom, such that it first interacts with a counter-propagating beam, getting a momentum kick in the direction opposite its motion. Here, k is a wave-number given by $2\pi/\lambda$ where λ is a wavelength of the cooling beams. Then, given that the atom stays in the e state, the subsequent interaction with the co-propagating beam induces stimulated emission back to g which imparts another momentum kick in the opposite direction of its motion as illustrated in Fig. 3.7. Therefore, for each sweep, the atom receives a $2\hbar k$ momentum kick on average which reduces the atom's speed.

Let's look closely into the parameters that determine the efficiency of the cooling and the cooling limit. First of all, the method relies on efficient transfer of atoms from g to e, which depends on the Landau-Zener probability of adiabatic passage to the excited state. Assuming that the lifetime of e is much longer than the duty cycle ($t_{\text{cycle}} \ll \tau_e$), and that the Rabi frequency Ω of the beams stays constant, this probability is given by [68],

$$p_{\text{LZ}} = 1 - \exp\left(-\frac{\pi}{2}\frac{\Omega^2}{\dot{\Delta}}\right) \tag{3.1}$$

where $\dot{\Delta}$ is a sweep rate $\Delta_{\text{sweep}}/t_{\text{sweep}}$. Here, Δ_{sweep} is a detuning range of the frequency

sweep, and t_{sweep} is the sweep duration. For the simplest case where the frequency of the cooling beams are reset instantaneously before each sweep, $t_{\text{sweep}} = t_{\text{cycle}}$. From the above expression, we can see this probability is solely determined by the adiabaticity parameter $\Omega^2/\dot{\Delta}$. The above equation shows that one would want a fast sweep rate Δ such that the atoms do not decay during t_{sweep} and also to address larger velocity classes, but this comes at the cost of requiring dramatically larger Ω to ensure a high probability of excitation. Although this equation captures an important understanding of the excitation process, we will see later that the excited state population never reaches p_{LZ}, because it decays during the whole excitation process for the experimental parameters we use.

For this cooling to work, the time-ordering of the interaction with the two beams is crucial. This ordering is determined by the initial state of the atom before the sweep starts, the sweep direction, and the magnitude of the Doppler shift. Assuming $t_{\text{sweep}} = t_{\text{cycle}}$ once again, the initial state preparation and the sweep direction can both be controlled. However, as the atoms are cooled via a train of sweep cycles, the Doppler shift of the atoms also reduces. At low momentum, when the Doppler shift becomes small compared to the Rabi frequency $kv \leq \Omega$, the time-ordering breaks and the atom would find itself in a heating trajectory if the spontaneous emission is neglected [66]. However, in real experimental settings, one cannot ignore the effect of the spontaneous emission which resets the atom back to the correct state, which would be g for the sweep direction shown in Fig. 3.7, at the beginning of each sweep, preventing the atoms from heating. Ref. [68] shows that the SWAP cooling can cool the atoms close to the recoil limit when the correct experimental parameters are met.

3.5.2 SWAP MOT

Our goal is to apply the SWAP cooling in a MOT setting. This setting is similar to the previous but more complex: a three-level atom interacts with a train of frequency-swept laser pulses in the presence of a quadrupole magnetic field, as illustrated in Fig. 3.8(a). In addition, the two laser beams have equal intensities and opposite circular polarizations and propagate with wave vectors $\pm k\hat{\boldsymbol{z}}$, where $k = 2\pi/\lambda$. This three-level atom setting is reflected in the level structure of ^{88}Sr atoms. Specifically, we consider the non-degenerate $^1S_0$ ground state $|g\rangle$ and the two stretched magnetic sublevels $|\pm\rangle$ of the $^3P_1$ state (V-type level scheme) for an atom moving in the $\hat{\boldsymbol{z}}$ direction, as shown in Fig. 3.8(a). Based on our experimental results, we will argue later that the population dynamics for ^{87}Sr with its ten nuclear magnetic states can be understood in a similar framework.

In this section, we will be investigating the frequency modulation and illumination sequences sketched in Fig. 3.8(b). In the first strategy, we use broadband-modulated laser cooling (BB), similar to traditional frequency-comb Doppler cooling. Here, the laser frequency is scanned in a triangle ramp between ω_{start} and ω_{end}, such that the laser is always red-detuned from the atomic resonance at ω_{atom}. We use three retroreflected laser beams that are always turned on, as indicated by the continuous illumination sequence below

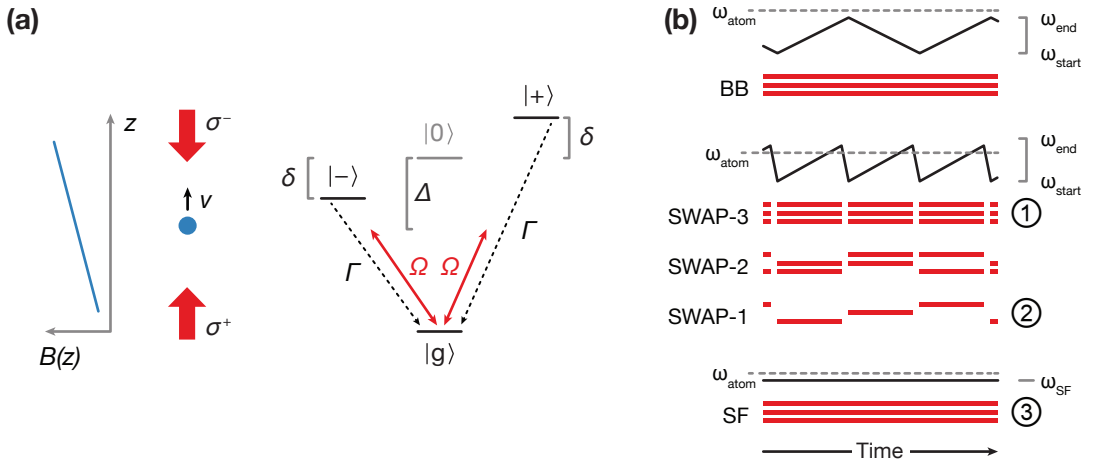

Figure 3.8 Illustration of the SWAP MOT configuration. (a) One-dimensional laser cooling configuration in the presence of a magnetic field gradient. We use a reduced three-level system in a V configuration to model cooling on the ^{88}Sr $^1S_0$-$^3P_1$ transition. (b) Detuning (black solid lines) and illumination (red rectangles) sequences for the three axes used in different cooling stages of the red MOT, as explained in the main text.

the frequency scan in Fig. 3.8(b). The red MOT lasers have $1/e^2$-waists of 3 mm and we use powers of up to 8 mW per beam. All measurements in this paper use red light derived from a tapered amplifier, seeded with a diode laser that is itself stabilized to a high-finesse reference cavity.

As an alternative to the BB strategy, we investigate the sawtooth-wave adiabatic passage (SWAP) cooling technique [66–68]. In this method, the laser frequency is ramped in a sawtooth-shaped ramp, as shown in the center panel of Fig. 3.8(b). In contrast to BB, the laser is swept across the free-space atomic resonance to ω_{end} and is rapidly reset to ω_{start} on a timescale that is fundamentally limited by the acoustic wave transfer time in the acousto-optical modulators that we use. To avoid another sweep across the resonance during this reset, we turn off the radio-frequency power in the acousto-optic modulators at ω_{end}. In combination with technical limitations in the timing system, the frequency reset results in dark time of ~ 5 μs after each sweep.

We investigate three SWAP strategies, labelled SWAP-3, SWAP-2, and SWAP-1, respectively, corresponding to the number of bright axes during each frequency sweep. Here, SWAP-3 is the only previously studied strategy in the context of magneto-optical trapping [67]. After a period of frequency-modulated laser cooling according to these strategies, we apply a period of red-detuned single-frequency Doppler cooling to the atoms, indicated in the bottom panel of Fig. 3.8(b) as strategy SF. We find that a combination of the strategies SWAP-3, SWAP-1, and SF results in the highest phase-space-density samples on the shortest time scales. We will first show a simple model to explain both BB

and SWAP strategies within a common framework.

Then, we will study the broadband BB, SWAP-3, SWAP-2, and SWAP-1 separately. Lastly, we will show our final sequence that combines both broadband SWAP and the single-frequency MOT.

SWAP MOT cooling model in 1D

We treat the atomic position z and velocity v classically and thus can combine the Doppler and Zeeman shifts of $|\pm\rangle$ into a single parameter $\delta = kv + g(^3\mathrm{P}_1)m(^3\mathrm{P}_1)\mu_B B' z/\hbar$ that describes the energy splitting between the states $|\pm\rangle$ corresponding to the magnetic quantum numbers $m(^3\mathrm{P}_1) = \pm 1$. The $J = 0 \to J = 1$ transition under consideration leads to equal Clebsch-Gordan factors of $1/\sqrt{3}$ for all possible transitions. Although we use retroreflected laser beams, which produce a standing wave with rotating linear polarization at each position, $|\delta| > 0$ locally selects the resonant transition and the cooling process terminates as soon as $|\delta|$ locally becomes small compared to the power-broadened linewidth. For a magnetic quadrupole field, the atom is thus cooled to a drift velocity pointing towards the magnetic field zero.

The above considerations result in an equal Rabi frequency $\Omega \equiv \Gamma/\sqrt{3}\sqrt{s_0/2}$ for each beam. Here, $s_0 = I_{\mathrm{pk}}/I_{\mathrm{sat}}$ is the saturation parameter in terms of the saturation intensity $I_{\mathrm{sat}} = \pi hc/(3\lambda^3\tau)$ and the Gaussian laser beams' peak intensity $I_{\mathrm{pk}} = 2P/(\pi w_0^2)$, with beam power P and $1/e^2$-waist w_0, respectively. We also allow for the lasers to be switched off by letting $\Omega(t)$ vary with time. The laser frequency for each beam is scanned simultaneously as $\Delta(t) \equiv \Delta_0 + f(t)$, starting at a fixed initial detuning $\Delta_0 \equiv \omega_{\mathrm{start}} - \omega_{\mathrm{atom}}$ and continuing with a periodic frequency ramp $f(t)$.

Under these assumptions, we find the time-dependent Hamiltonian

$$H(t)/\hbar = \begin{pmatrix} \Delta(t)+\delta & 0 & \Omega(t)/2 \\ 0 & \Delta(t)-\delta & \Omega(t)/2 \\ \Omega^*(t)/2 & \Omega^*(t)/2 & 0 \end{pmatrix}, \tag{3.2}$$

and the optical Bloch equations for the density matrix ρ

$$\dot{\rho} = -i[H(t)/\hbar, \rho] + \mathcal{L}\rho. \tag{3.3}$$

We model the effects of spontaneous emission on the elements of the density matrix by the Liouvillian

$$\mathcal{L}\rho = -\Gamma \begin{pmatrix} \rho_{11} & \rho_{12} & \rho_{13}/2 \\ \rho_{21} & \rho_{22} & \rho_{23}/2 \\ \rho_{31}/2 & \rho_{32}/2 & -\rho_{11}-\rho_{22} \end{pmatrix}. \tag{3.4}$$

This model is useful to describe the loading and initial cooling of the red MOT because the atomic velocity and position do not change significantly on the timescale of

the cycle time $t_{\mathrm{cycle}} \equiv t_{\mathrm{sweep}} + t_{\mathrm{dark}}$, which in all cases of interest is on the order of the atomic lifetime τ. This condition places the initial stage of frequency-swept laser cooling in the red MOT in an interesting regime. We work neither in the adiabatic rapid passage regime, where $t_{\mathrm{cycle}} \ll \tau$, nor fully in the steady state with respect to atomic decay, where $t_{\mathrm{cycle}} \gg \tau$. For this reason, adiabatic approximations of the Bloch equations produce misleading results and we have to rely on numerical solutions to explain our experimental results. For instance, we show the population dynamics of a typical pulse train for a representative sweep (dead) time of $t_{\mathrm{sweep}} = 2\tau$ ($t_{\mathrm{dead}} = 0.238\tau$) in the high velocity regime in Fig. 3.9(a). Here, an atom at detuning $\delta = 100\ \Gamma$ is exposed to a train of laser pulses whose frequency is swept over $\Delta_{\mathrm{sweep}} = 1000\ \Gamma$, ending at $\omega_{\mathrm{end}} - \omega_{\mathrm{atom}} = +13.3\ \Gamma$, with a Rabi frequency of $\Omega = 34\ \Gamma$. Because of the large splitting between the excited states, the pulse train efficiently excites only the $|+\rangle$ state. After the first excitation, spontaneous emission reinitializes the atom to a ground state fraction depending on t_{cycle}/τ. We find that the population dynamics reliably settle to a periodic pattern for all parameter ranges in this work after a few cycles.

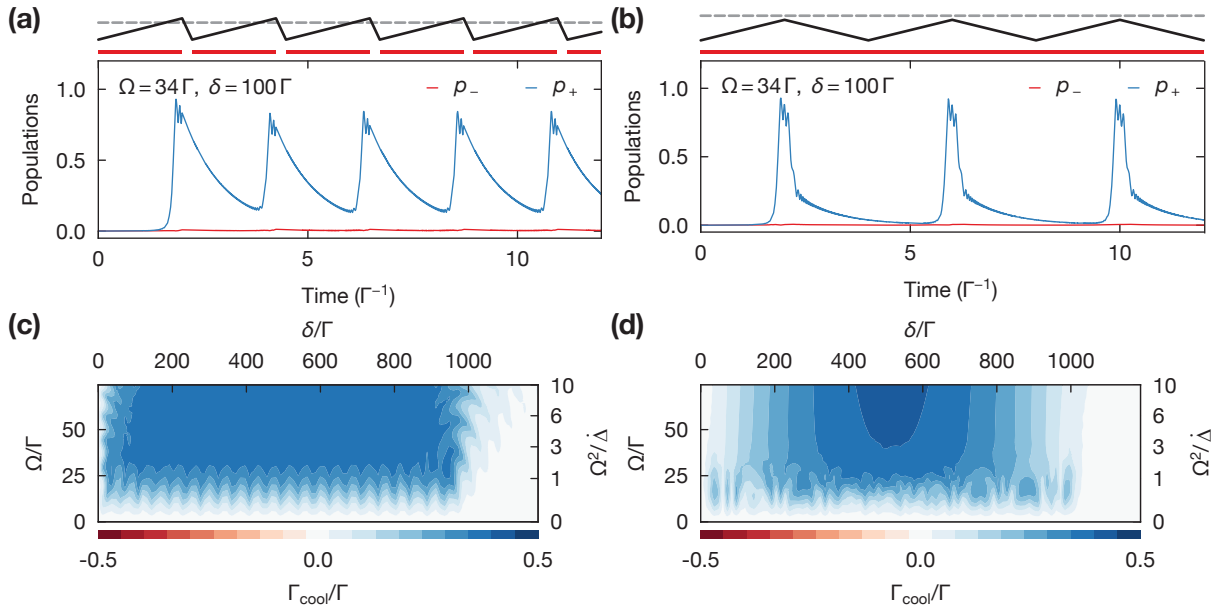

Figure 3.9 SWAP MOT cooling in a high-velocity regime. (a) Typical population dynamics in the high-velocity (or $|\delta| \gg \Omega/\sqrt{2}$) regime. We use $t_{\mathrm{sweep}} = 2\tau$ and $\Delta_{\mathrm{sweep}} = 1000\,\Gamma$ for all results shown in this Figure. (b) Traditional broadband frequency-modulated cooling can be understood within the same framework. For atoms at small $|\delta|$, the downward sweep causes stimulated emission by the *same* beam that caused the excitation on the upward sweep. (c) In the adiabatic regime, where $\Omega^2/\dot{\Delta} > 2/\pi$, the cooling rate Γ_{cool} is remarkably insensitive to the level splitting δ and Rabi frequency Ω. (d) The unwanted stimulated emission process partially cancels the desired momentum transfer, reduces the cooling rate, and causes a stronger parameter dependence in the low-$|\delta|$ regime for BB compared to SWAP.

We can also see from Eqn. 3.2 that if $|\delta| \ll \Omega/\sqrt{2}$, because the velocity and the Zeeman splitting are small or compensate each other, we have a competition between adiabatic passage from the ground state to either of the excited states $|\pm\rangle$. If there is no imbalance between the transition probability to $|\pm\rangle$, the cooling efficiency vanishes, because the atom absorbs a photon from each of the counterpropagating beams. Typical population dynamics for $\delta = 2.4\ \Gamma$ are shown in Fig. 3.10.

The transition from cooling to heating leads to a balance where one finds the same steady-state temperature $k_B T_{\mathrm{ss}} = \hbar\Omega/2$ as for Doppler cooling as long as one cannot take advantage of stimulated processes where the atom is stimulated back to the ground state by the *other* beam [68]. In contrast to optical molasses [66] it is not possible to realize this situation in a magneto-optical trap [67], because opposite circular polarizations are used in combination with a magnetic-field gradient to create localization. In a situation where one can separate atomic localization from the excitation process, such as in a magic-wavelength optical dipole trap, SWAP cooling could be much more effective by exploiting stimulated emission in the regime of $t_{\mathrm{cycle}} \ll \tau$ as originally envisioned [66, 68].

To describe the efficiency of the cooling process, we introduce the laser cooling rate

$$\Gamma_{\mathrm{cool}} \equiv \Gamma\, \mathrm{sign}(\delta) \langle p_+ - p_- \rangle_{\mathrm{cycle}} \tag{3.5}$$

as the difference between the scattering rates due to the cycle-averaged probabilities of exciting the corresponding states $p_+ \equiv \rho_{11}$ and $p_- \equiv \rho_{22}$, respectively. Because the SWAP cooling process is based on adiabatic passage, this cooling rate is remarkably insensitive to laser frequency or intensity drifts, as shown in Fig. 3.9(c).

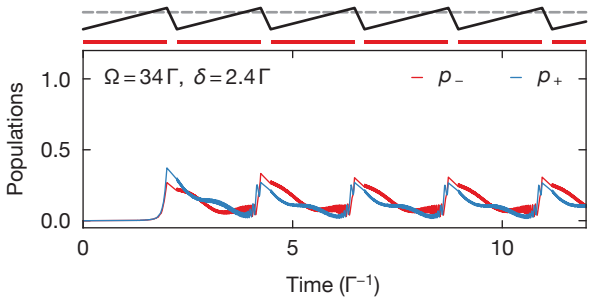

Figure 3.10 SWAP MOT cooling dynamics in a high-velocity regime. Typical population dynamics in the low-velocity (or $|\delta| \ll \Omega/\sqrt{2}$) regime where cooling stops.

Interestingly, we can understand the broadband-modulated laser cooling (BB), traditionally used in narrow-line magneto-optical traps for Sr [64, 49, 37] within the same framework: In Fig. 3.9(b), we show population dynamics for a pulse train where the laser frequency is ramped in a triangle pattern with the same slope (Rabi frequency) $\dot{\Delta}$ (Ω) as

in panels (a), such that the adiabaticity parameter remains the same. The laser is never turned off ($t_{\mathrm{dead}} = 0$) and the detuning ramp still spans $\Delta_{\mathrm{sweep}} = 1000\,\Gamma$, but ends to the red of the resonance at $\omega_{\mathrm{end}} - \omega_{\mathrm{atom}} = -13.3\,\Gamma$. We immediately see the disadvantage of this BB strategy compared to the SWAP-1 strategy, in that p_+ is not allowed to decay spontaneously, but is stimulated back to the ground state on the down-slope of the ramp by the *same* beam that excited it. This stimulated process produces a momentum kick opposite to the initial excitation and reduces the amount of spontaneous scattering, and thus Γ_{cool}.

As shown in Fig. 3.9(d), the BB strategy works well when the time between adiabatic transfers on the up- and down-slope of the frequency ramp is long enough for a significant fraction of p_+ to decay, because adiabatic passage is insensitive to the direction of the frequency sweep across the resonance. However, the cooling efficiency is strongly reduced for low-$|\delta|$ atoms compared to SWAP-1. Some of this efficiency can be recovered by modulating the laser frequency in a sinusoidal fashion (reduced $\dot{\Delta}$ at small $|\delta|$) as traditionally done [49, 63], but SWAP is more efficient.

In conclusion, we find that the adiabatic passage picture provides a better framework to understand both traditional BB and SWAP cooling strategies. In addition, the model predicts that, compared to BB, SWAP (1) optimizes the excitation process for low-velocity atoms at low Zeeman shifts, (2) makes the cooling process more homogeneous across the whole thermal sample loaded from the magnetic trap, and (3) is more robust with respect to intensity fluctuations.

In the subsequent section, we will show experimental results that support this conclusion and discuss secondary experimental conditions that influence the choice of cooling strategy.

3.5.3 Experimental Implementation of SWAP MOT

To study the differences between the cooling strategies sketched in Fig. 3.8(b), we start by applying the corresponding pulse train for a time t_{red} to the atomic sample while keeping the magnetic field gradient and the laser intensity constant. At the end of t_{red}, we turn off the magnetic field gradient as well as the laser beams, and either image the atoms in situ, or allow the atoms to fall for $15\ \mathrm{ms}$ before imaging. We take two absorption images simultaneously by exposing the atomic cloud for $50\ \mu\mathrm{s}$ to two separate probe beams propagating along Y and Z, respectively. Using standard methods [86], we extract the temperature, atom number, and in-trap phase-space-density of the atomic cloud. The error bars for these quantities combine a 10% shot-to-shot atom number fluctuation with the statistical fit error derived by rescaling each image fit to $\chi^2 = 1$.

The results for varying cooling times t_{red} are shown in Fig. 3.11(a). Here, all strategies use a common red laser power of $2\ \mathrm{mW}$ per axis and a sweep range of $\sim$11 MHz. The SWAP strategies end at a (blue) detuning of $100\ \mathrm{kHz}$, while the BB strategy ends at

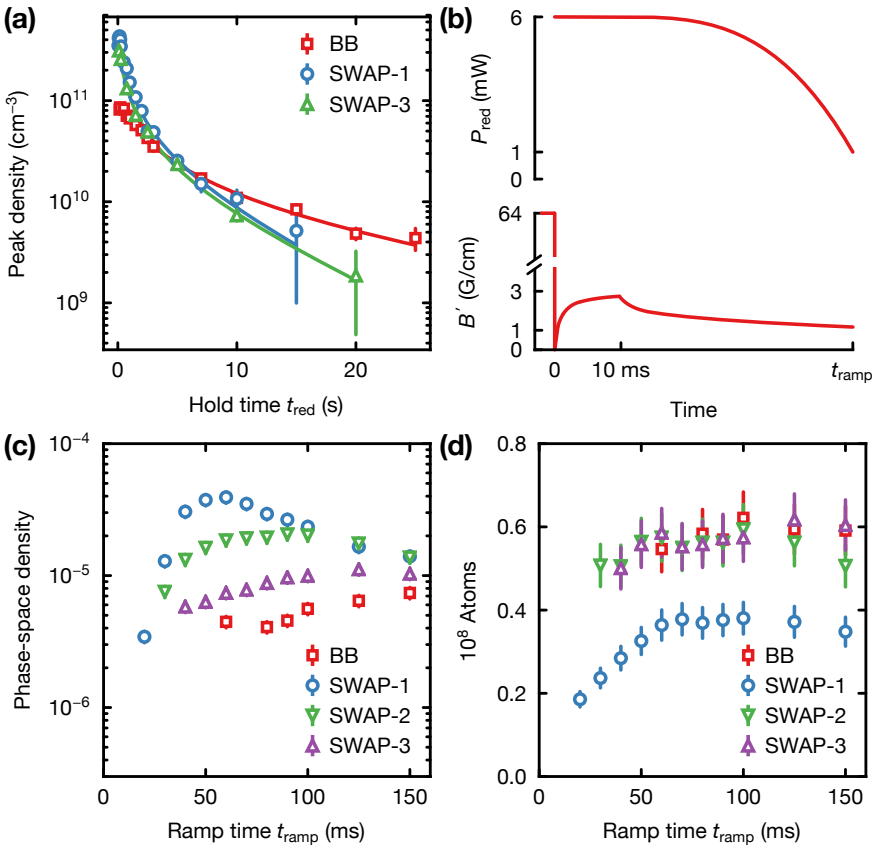

Figure 3.11 (a) The peak density decreases as a function of hold time when the intensity and magnetic field gradient are held constant. At short times, light-assisted collisions at high densities lead to loss for all cooling strategies. (b) Optimized ramp of the light intensity and magnetic field gradient used to measure phase-space-densities (c) and atom numbers (d) versus ramp time t_{ramp} for all modulation strategies.

a (red) detuning of $-100\,\mathrm{kHz}$. We use a sweep time $t_{\mathrm{sweep}} = 40\ \mu\mathrm{s}$ ($80\ \mu\mathrm{s}$) for SWAP (BB).

Compared to the SWAP strategies, BB exhibits a lower initial density, but a slower decay at long times. We determine both $1/e$ lifetime τ_{MOT} and two-body-loss rate coefficient K_2 for all strategies by fitting the solution of $\dot{n} = -n/\tau_{\mathrm{MOT}} - K_2 n^2$ to the density data in Fig. 3.11(a). We find that the red-detuned BB strategy leads to a MOT with $\tau_{\mathrm{MOT}} = 25 \pm 10\ \mathrm{s}$, comparable to the lifetime of atoms in the magnetic trap. We thus attribute this one-body loss to collisions with the atomic beam. The SWAP-1 and SWAP-3 strategies lead to a reduced $\tau_{\mathrm{MOT}} = 7(2)\ \mathrm{s}$ and $8(2)\ \mathrm{s}$, respectively. In addition, all strategies show non-exponential loss at short times, due to light-assisted scattering on the repulsive V_{1u} asymptote [111]. We find similar two-body-loss rate coefficients $K_2 \simeq 5(1) \times 10^{-12}\ \mathrm{cm}^3/\mathrm{s}$ for all strategies at this laser power.

Previous attempts at optimizing the broadband stage of the cooling procedure made a choice between quickly cooling only the coldest atoms for atomic clocks [49] and slowly cooling almost all atoms for quantum gas experiments [37]. With the SWAP technique, we aimed to combine the advantages of both methods and varied the parameters of each strategy to obtain the coldest samples in the shortest times. As we see in Fig. 3.11(a), the SWAP-1 strategy can condense hot atoms on fast timescales and thus reaches its steady-state temperature quickly. This steady-state temperature is proportional to the laser intensity, and the shape of the atomic cloud is determined by the magnetic field gradient [49]. We thus ramp both magnetic field gradient and laser intensity with the empirically optimized polynomial shapes shown in Fig. 3.11(b) while the atoms are cooled. Under these conditions, we find that the strategies produce samples with dramatically different phase-space densities as a function of total ramp time. In Fig. 3.11(c), we see that all strategies have an optimal associated time: If we ramp too quickly, the phase-space density remains low. If we ramp too slowly, we start to lose phase-space density due to light-assisted collisions between the coldest atoms. We also see that SWAP-1 produces the highest phase-space densities while BB performs the worst. The SWAP-1 strategy achieves this goal despite losing 40% of the atoms, as shown in Fig. 3.11(d). This loss is not present in the other strategies, and we attribute this loss to hot atoms that escape from the cooling region while the corresponding axes are not illuminated.

Based on these results, we decided to combine the high capture efficiency of SWAP-3 with the fast and efficient cooling of SWAP-1. We use the same laser power and magnetic field ramps as in Fig. 3.11(b), but switch from SWAP-3 to SWAP-1 at a time $t_{\mathrm{switch}} < t_{\mathrm{ramp}}$. We optimized t_{switch} and the SWAP cooling parameters of this combined sequence in detail for both bosonic ^{88}Sr and fermionic ^{87}Sr isotopes, and found that its performance is limited by the initial capture fraction of SWAP-3 from the magnetic trap.

In Fig. 3.12(a), we show the atom number at $t_{\mathrm{ramp}} = 45\ \mathrm{ms}$ ($150\ \mathrm{ms}$) for ^{88}Sr (^{87}Sr) versus the initial power per beam P_{init}. We trap 1.5×10^8 (1.0×10^7) ^{88}Sr (^{87}Sr) atoms for $P_{\mathrm{init}} = 8\ \mathrm{mW}$. The data suggests that we reach the adiabatic passage regime for relatively

low initial powers. We find that a sweep range of $\Delta_{\mathrm{sweep}} = 2\pi \times 11$ MHz ($2\pi \times 5.7$ MHz) for ^{88}Sr (^{87}Sr) produces a comparable power-dependence for both isotopes. The ratio between sweep ranges is consistent with similar cooling conditions requiring similar adiabaticity parameters, and the lower average scattering rate for the $F = 9/2 \rightarrow F' = 11/2$ transition in ^{87}Sr compared to the $J = 0 \rightarrow J' = 1$ transition in ^{88}Sr. The final number of ^{87}Sr atoms is ∼80% of the value suggested by the relative natural abundance of ^{87}Sr and ^{88}Sr (7.00%/82.58%). We attribute this discrepancy to the more extended atomic density profile in the magnetic trap. If sufficient optical power is available, increasing the beam sizes could lead to an improved capture fraction. For a given beam size, the capture fraction of the SWAP MOT seems to be proportional to the adiabaticity parameter if we take into account that ^{87}Sr scatters less cooling light than ^{88}Sr.

In the remainder of Fig. 3.12, we explore the SWAP cooling parameters for two representative initial powers: (1) a "low" power per beam of 3 mW that is available from a typical diode laser at 689 nm, and (2) a "high" power per beam of 8 mW that requires multiple diode lasers or a tapered amplifier. For brevity, we only show data for ^{88}Sr, because we find equivalent results for ^{87}Sr with the caveat of a reduced scattering rate that requires a reduced sweep range for the same power.

When we vary the sweep range Δ_{sweep} by varying ω_{start}, we find the data shown in Fig. 3.12(b). For high power, the atom number first increases and then saturates because an increased sweep range can address atoms at higher Zeeman shifts. For low power, the atom number peaks, but then slowly decreases with the linear decrease in adiabaticity parameter. Even though the atom number shows a similar behavior in the low- and high-power limits, the phase space density decreases exponentially with increased sweep range, as shown in Fig. 3.12(c). This behavior is consistent with an exponential decrease in the cooling rate due to the reduced adiabatic transfer efficiency $\propto p_{\mathrm{LZ}}$. We show in Fig. 3.12(d) that the sweep time influences the number of atoms dramatically as well: the cooling rate is too small to capture the fastest atoms for increased sweep times. Finally, we find that reducing the sweep time below the natural lifetime does not improve the number of captured atoms in the SWAP MOT, consistent with the predictions of the optical Bloch equations in the previous section.

3.6 Single-frequency MOT

As a last step in our cooling protocol, we use traditional narrow-line laser cooling at a single frequency to reach final temperatures of $1-2$ μK. We start the red MOT with the optimized SWAP combination sequence discussed the previous section. The laser frequency is scanned from $\omega_{\mathrm{start}} - \omega_{\mathrm{atom}} = -2\pi \times 8.5$ MHz (-4.2 MHz) to $\omega_{\mathrm{end}} - \omega_{\mathrm{atom}} = 2\pi \times 0.1$ MHz for ^{88}Sr (^{87}Sr) as shown in the upper panel of Fig. 3.13. At the same time, the laser power and magnetic field gradient are slowly ramped with the polynomial shapes shown in Fig. 3.13. After reaching the steady state of the combined technique, we switch to the

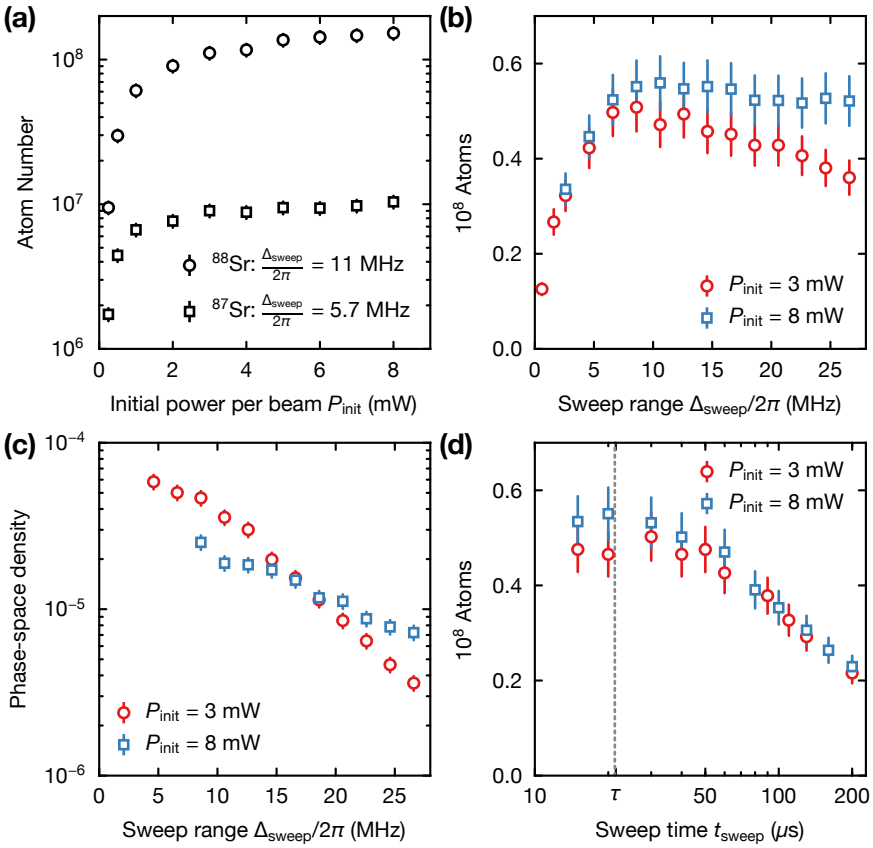

Figure 3.12 (a) The atom number in the SWAP MOT for an 8.5 MHz sweep range saturates as a function of the initial laser power per beam P_{init} for ^{88}Sr and ^{87}Sr. (b) For ^{88}Sr, the atom number saturates for high powers per beam (blue squares) as a function of sweep range, but decreases linearly for large sweep range at low powers (red circles). (c) At the same time, the phase-space density decreases exponentially. (d) Longer sweep times preclude capturing the fastest atoms from the magnetic trap. Sweep times shorter than the natural lifetime τ do not increase the capture fraction further.

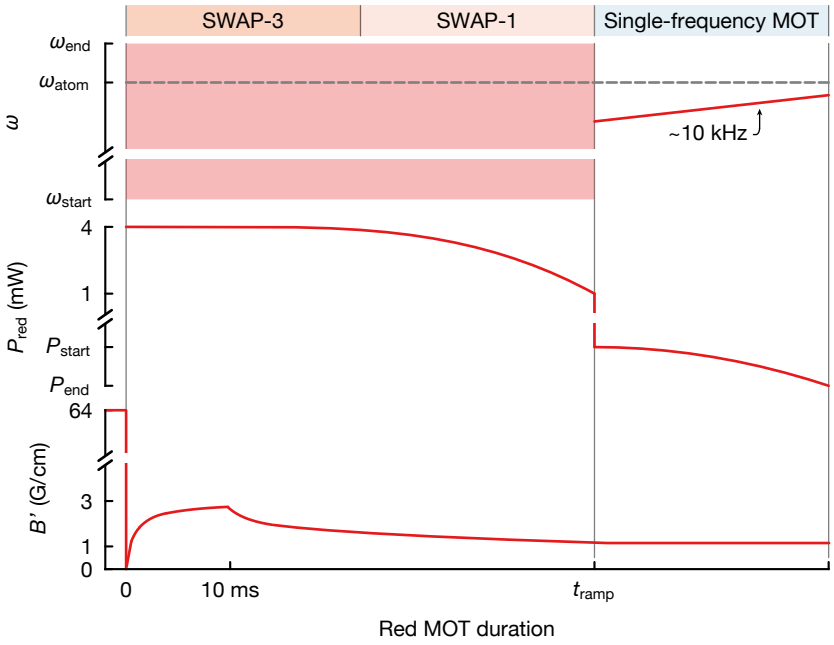

Figure 3.13 Optimized experimental sequence used for our both ^{88}Sr and ^{87}Sr magneto-optical traps. The cooling technique in a given interval is indicated at the top (SWAP-3, SWAP-1 or single-frequency MOT). Top, middle, and bottom graphs show the red MOT beam frequency spectrum, power, and gradient traces versus the red MOT duration, respectively.

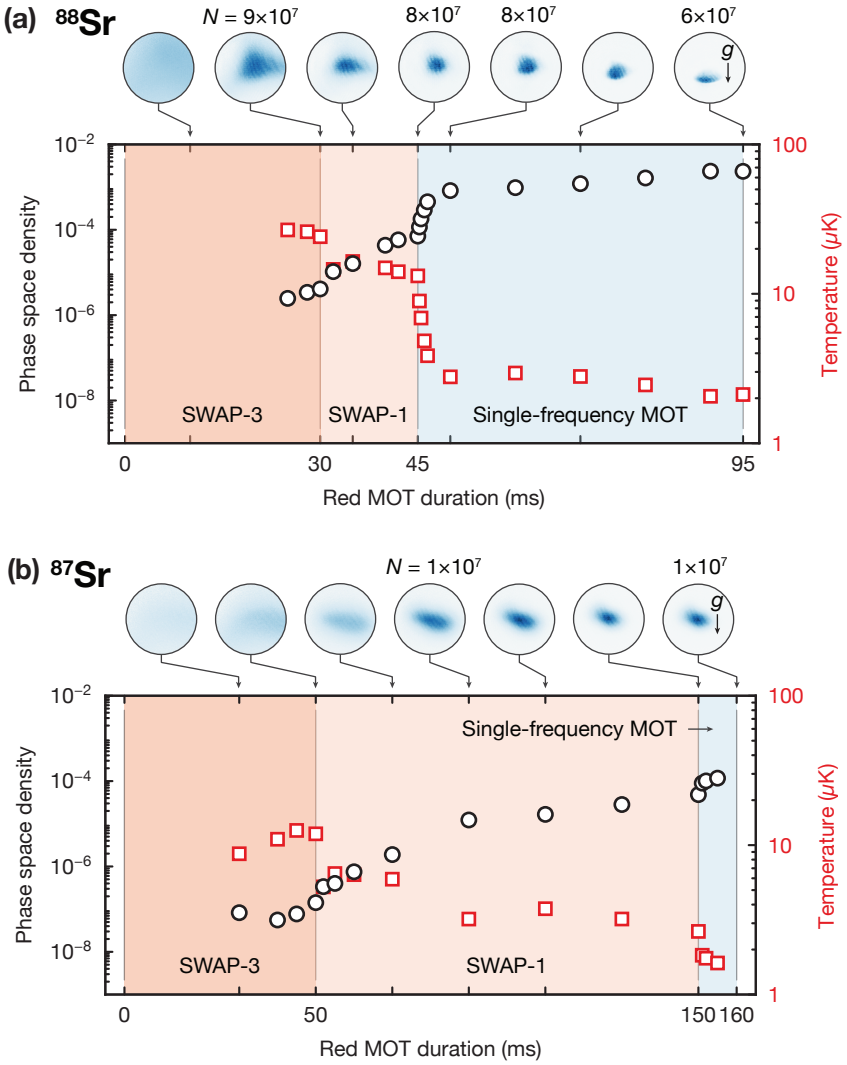

Figure 3.14 Performance of the final red MOT sequence. (a) Measured temperatures (red squares) and phase-space densities (black circles) versus red MOT duration for ^{88}Sr. The label on the bottom (SWAP-3, SWAP-1 or single-frequency MOT) specifies the active cooling strategy. In-situ images taken at different red MOT times are shown on the top with atom number (N) and the direction of gravity (g). (b) We find comparable results for ^{87}Sr when taking the reduced scattering rate into account.

single-frequency MOT at t_{ramp} to further cool the sample. To switch to the SF strategy, we select cooling parameters that would leave the cloud shape and temperature unchanged. Thus, we turn off the frequency scan, set the laser frequency to a -80 kHz (-10 kHz) red detuning, and quickly lower the beam power from 1 mW to $P_{\mathrm{start}} = 35$ μW (20 μW) for ^{88}Sr (^{87}Sr). Finally, we ramp the beam power once again with a polynomial shape to $P_{\mathrm{end}} = 1$ μW (0.5 μW) for ^{88}Sr (^{87}Sr) to reduce the steady-state temperature of the cooling process. To ensure fast cooling during the single-frequency MOT, we minimize the atomic movement along gravity caused by the change in the detuning and gradient [49]. We thus limit the detuning ramp amplitude to only $\sim$10 kHz and keep the gradient constant.

The series of in-situ absorption images of ^{88}Sr in Fig. 3.14(a) illustrates the cooling process. The SWAP-3 strategy allows us to capture about 9×10^7 atoms, but the cloud remains large and dilute. As soon as we switch to SWAP-1, the atomic cloud shrinks visibly. In the single-frequency MOT, the atoms sag along the direction of gravity while cooling to a few μK, which is a characteristic behavior of the bosonic narrow-line MOT [49]. We cool to 3 μK after 5 ms of the single-frequency MOT without losing atoms. The phase-space density at this point is 8×10^{-4}, a factor of 400 larger than for the case of a red MOT time of 25 ms (prior to this, we cannot get reliable estimates due to irregular in-situ shapes). The phase-space density increases further over the final 45 ms of single-frequency cooling and reaches 2×10^{-3} with a final temperature of 2 μK at the expense of losing 25% of the atoms. Note that this final cooling step in the single-frequency MOT takes the same amount of time as all of the initial cooling procedure, pointing towards a mechanism that competes with the cooling process while the ^{88}Sr atoms sag to the lower edge of the MOT. This atom loss is likely due to a combination of light-assisted collisions and radiation trapping [35, 112].

We apply the same protocol to ^{87}Sr, but increase its cooling efficiency by adding red stirring laser beams [64], which copropagate with the red MOT beams. The in-situ images in Fig. 3.14(b) show the cooling progress for ^{87}Sr. Unlike ^{88}Sr with its vanishingly small scattering length, the ^{87}Sr sample does not sag under gravity. Instead, it thermalizes by interparticle collisions [64, 37]. We observe larger and more dilute initial atomic clouds of ^{87}Sr than of ^{88}Sr during SWAP-3, because of the reduced cooling rate discussed in the previous Section. For the same reason, it takes longer to condense the ^{87}Sr cloud to the steady state in the subsequent SWAP-1 cooling stage. In total, we find that we need to operate the SWAP MOT about three times longer for ^{87}Sr than for ^{88}Sr. We reach a temperature of 3 μK and a phase-space density of 5×10^{-5} at the end of SWAP-1. The subsequent 10 ms of single-frequency MOT cools the atoms further, reaching a final temperature of 1.4 μK and a phase-space density of 1.4×10^{-4} without atom loss.

3.7 Conclusion

In this chapter, we described the basic construction of our Sr quantum simulator including the vacuum system, laser systems, and production of red and blue MOTs. For the latter, we described an improved method to produce high-phase-space-density red MOTs using sawtooth-wave adiabatic passage cooling. With a simple model, we have shown that even the traditional broadband-modulated laser cooling used in most Sr MOTs is better understood within the adiabatic passage framework. Our theoretical studies predict and our experimental results show that a SWAP MOT is more robust and efficient than the traditional broadband-modulated MOT. We investigated three SWAP MOT strategies. We found that illuminating all axes in the SWAP-3 strategy leads to the largest capture fraction from the magnetic trap. Once the atoms have been captured and cooled to the steady-state temperature, it is beneficial to illuminate only one MOT axis at a time. This SWAP-1 strategy reduces light-assisted collisions, avoids unwanted stimulated exchange of momentum between different axes, and thus leads to a much faster cooling speed at low temperatures. At very low temperatures, regular narrow-line Doppler cooling at a single frequency becomes the optimal strategy (SF). To exploit the advantages of SWAP-3, SWAP-1, and SF, we combined them in an optimal way. With this combined sequence, we created high-phase-space-density samples of bosonic ^{88}Sr and fermionic ^{87}Sr atoms within 50 and $160\,\mathrm{ms}$, respectively. Our results for ^{88}Sr also suggest that the narrow-line, single-frequency cooling stage produces most of its effect on time scales of 10 ms before it becomes limited by density-dependent effects [35, 112]. Our method is simple to implement, and in combination with high-flux atomic sources [112–114], it can be used to improve the duty cycle of atomic clocks and the repetition rate of precision experiments and quantum simulations. Extending our method by a final dark-spot MOT stage [37] might result in even lower final temperatures and higher phase-space densities. We expect that our cooling method can also benefit narrow-line magneto-optical traps for other two-electron atoms, lanthanides, and molecules.

Chapter 4

Demonstration of a state-dependent lattice for the strontium clock states

Having presented the background knowledge of state-dependent traps and our steps for creating both a ~ 1 μK-cold ^{88}Sr and ^{87}Sr atomic cloud, we are finally ready to discuss our experimental demonstration of a state-dependent optical lattice for strontium clock states. This demonstration was performed using the same setup as described in the previous chapter (Chapter 3) and by loading the ultracold strontium into a 1D optical lattice made with a free-space beam. Although our ultimate goal is to implement 3D state-dependent lattices in which the horizontal lattices are generated by the build-up cavities, benchmarking the performance of a state-dependent lattice in a simpler setting using a 1D lattice made by a free-space beam will help us disentangle any heating problems that arise in the cavity setup in future.

For the benchmarking, our goals were 1) to precisely measure the tune-out wavelengths, which has not been done for strontium prior to this work although many related works exist for alkali atoms, 2) to measure the polarizabilities of g and e at the tune-out wavelengths of e and g, respectively, thereby benchmarking the achievable trap depth, 3) to trap the clock states in the state-dependent lattices and measure their lifetimes. While pursuing these objectives, we focused exclusively on the tune-out wavelength of g ($\lambda_{t,g}$), for two reasons. First, the excited state (e) atoms have strong two-body collisions that shorten their lifetimes in a 1D lattice. Second, the tune-out wavelength of e lies at 633 nm, where the available laser power is limited. Although diode lasers are available, they only output ~ 30 mW, and tapered amplifiers at this wavelength are currently not available (although they were once available from the company Eagleyard for a limited time). One method could have been to use a dye laser or setting up a doubling cavity from 1266 nm. Since our build-up cavities would solve the laser power issue, we decided not to put any effort into developing high power laser sources for 633 nm. Despite the above limitations, the methods that will be explained in this section can be applied to e atoms without much difficulty in our final setup. In it, we have the ability to restrict lattice occupancy to one atom per site in a 3D lattice, thus eliminating two-body collisions. Furthermore, the intra-cavity amplification from the build-cavities allows the generation of deep lattices at 633 nm.

In this chapter, we elaborate on the calculation of dynamical polarizability $\alpha(\omega)$ using a quantum mechanical picture and provide the tune-out frequency $\omega_{t,g}$ ($2\pi \times c/\lambda_{t,g}$) for

^{88}Sr and ^{87}Sr (Section 4.1). Since we only consider the tune-out frequency (wavelength) of g in this section, we drop the subscript g and replace $\omega_{t,g}$ ($\lambda_{t,g}$) with ω_t (λ_t). Then, we summarize the experimental setup and results of measuring ω_t and implementing the state-dependent lattice at ω_t (Section 4.2). Since this work has been performed jointly with another PhD researcher who has already published his thesis [55], we will keep the summary brief as most of the details can be found in Ref. [55] and [40], and we will focus on those that have not been discussed. Lastly, we discuss how the precise knowledge of ω_t can be used to calculate atomic lifetimes, refining our knowledge of the atomic structure of strontium (Section 4.3). As strontium is the primary atom used in optical lattice clocks, precise knowledge of its atomic structure can reduce the uncertainty on the systematic frequency shifts of strontium atomic clocks. When calculating these lifetimes, we find large discrepancies in the atomic data that are used to calibrate systematic effects in Sr optical lattice clocks, thus calling for a thorough experimental reinvestigation.

4.1 The $^1S_0$ ground state tune-out frequency

The dynamical polarizability $\alpha(\omega)$ of an electronic state consists of contributions from the core electrons ($\alpha(c;\omega)$) and valence electrons. The valence part of the polarizability is determined by summing up all the contributions of excited states v that are dipole-coupled to the state of interest, $\sum_v \alpha(v;\omega)$, and it is this valence polarizability that we reviewed in Section 2.3. For applications of creating far-off resonant traps, researchers are interested in the range of ω where $\alpha(\omega) \gg 0$ or $\alpha(\omega) \ll 0$. In this case, the valence part dominates, $\sum_v \alpha(v;\omega) \gg \alpha(c;\omega)$; thus, $\alpha(c;\omega)$ is often neglected. However, for precise knowledge of the tune-out frequency where $\alpha(\omega) = 0$, $\alpha(c,\omega)$ cannot be ignored as it shifts the tune-out frequency, although $\alpha(c;\omega)$ can be treated as an offset that does not depend on ω.

Each contribution from an excited state v of the valence part can be calculated by treating the effect of a far-off resonant laser light as a second order perturbation to the energy of a non-degenerate atomic state of interest k [115–118]. This treatment results in

$$\alpha_k(v;\omega) = \left(\frac{|\langle v|\,\hat{\mathbf{e}}\cdot\boldsymbol{d}\,|k\rangle|^2}{\hbar(\omega_{kv} - \omega - iA_v/2)} + \frac{|\langle k|\,\hat{\mathbf{e}}\cdot\boldsymbol{d}\,|v\rangle|^2}{\hbar(\omega_{kv} + \omega + iA_v/2)}, \right) \tag{4.1}$$

where $\hat{\mathbf{e}}$, $\boldsymbol{d}$, A_v are the laser polarization unit vector, induced dipole moment, and the total decay rate of an excited state v, respectively, as already introduced in Chapter 2. Here, $\langle k|\,\hat{\mathbf{e}}\cdot\boldsymbol{d}\,|v\rangle$ is a dipole matrix element between k and v. This dipole matrix element is related to the partial decay rate as:

$$\Gamma_{kv} = \frac{\omega_{kv}^3}{3\pi\epsilon_0\hbar c^3}|\langle v|\,\hat{\mathbf{e}}\cdot\boldsymbol{d}\,|k\rangle|^2. \tag{4.2}$$

In most cases, the total decay rate A_v is well known from experimental measurements, whereas Γ_{kv} is not directly accessible. Therefore, Γ_{kv} can be calculated from a measured

A_v. Following the derivations in Refs. [65, 107],

$$\Gamma_{kv} = A_v \omega_{kv}^3 \frac{(2F_k+1)\begin{Bmatrix} F_k & F_v & 1 \\ J_v & J_k & I \end{Bmatrix}^2}{\sum_{F=|J_k-I|}^{|J_k+I|} \omega_{k,F}^3 (2F+1)\begin{Bmatrix} F & F_v & 1 \\ J_v & J_k & I \end{Bmatrix}^2} \sum_{m_v=-F_v}^{F_v} (2F_v+1)\begin{pmatrix} F_k & 1 & F_v \\ m_k & p & -m_v \end{pmatrix}^2 \tag{4.3}$$

where we have considered a case that an excited hyperfine structure manifold decays to a lower hyperfine structure manifold, $F_v \to F_k$. The summation in the denominator in Eqn. (4.3) takes into account that F_v can decay to any ground hyperfine structure. Here, p specifies the laser polarization where $p = 0$ is linear and $p \pm 1$ is circular. The above expression can be used for the fine structures as well; in that case, F, J, and I are replaced by J, L, and S, respectively. It can be shown that for the case of a two-level atom, $\Gamma_{kv} = A_v$, and Eq. (4.1) becomes approximately $\alpha(\omega)$, found using the classical approach in Eq. (2.6). In a nutshell, Eqn. (4.3) contains a branching ratio of different decay paths and Clebsch Gorden coefficient resulted from applying the Wigner-Eckert theorm to the dipole operator.

Let us now focus on calculating $\alpha(\omega)$ of the ground state ^{1}S$_0$ ($\alpha_g(\omega)$). The valence part of the ground state ^{1}S$_0$ (g) polarizability is determined by summing over all the contributions of excited states dipole-coupled to g, which is dominated by the ^{1}P$_1$ and ^{3}P$_1$ contributions. For this reason, we write the g polarizability using the four components

$$\alpha_g(\omega) = \alpha_g(^1\mathrm{P}_1;\omega) + \alpha_g(^3\mathrm{P}_1;\omega) + \alpha_g(v';\omega) + \alpha_g(c;\omega), \tag{4.4}$$

where $\alpha_g(j;\omega)$ are the contributions from the excited state j, $\alpha_g(v';\omega)$ is the sum of contributions from all other valence states, $\alpha_g(c;\omega)$ is the contribution of the core electrons.

The contribution from the ^{1}P$_1$ and ^{3}P$_1$ states be expressed in terms of the total decay rate A_v by combining Eq. (4.1), Eq. (4.2), and Eq. (4.3). However, it would be difficult to see the dependence of the polarizability on light- and atom-polarization. A more nature way to expression the valence polarizability is to decompose it into a spherical tensor basis. This decomposition will allow us to see the dependence of the polarizability on light- and atom-polarization better, providing us an intuitive picture for the light and atom interactions. A good derivation and review of this decomposition is available from Refs. [116, 115, 107, 119], although the notations vary across the literatures. Then, the each contribution decomposes into scalar, vector, and tensor components as [116, 115]

$$\begin{aligned} \alpha_g(j;\omega) = &\alpha_g^s(j;\omega) \\ &+ \alpha_g^v(j;\omega)(i\boldsymbol{\epsilon}\times\boldsymbol{\epsilon}^*)\cdot\boldsymbol{e}_z\frac{m_F}{F} \\ &+ \alpha_g^t(j;\omega)\frac{3|\boldsymbol{\epsilon}\cdot\boldsymbol{e}_z|^2-1}{2}\frac{3m_F^2-F(F+1)}{F(2F-1)}, \end{aligned} \tag{4.5}$$

where F is the hyperfine quantum number associated with the ground state g, m_F is the corresponding magnetic quantum number, and j indicates one of the excited states $^1\mathrm{P}_1$ and $^3\mathrm{P}_1$. The $^1\mathrm{S}_0$ (g) state of the fermionic isotope ^{87}Sr has a single hyperfine state $F = 9/2$, since the electronic angular momentum J and the nuclear spin I are 0 and $9/2$, respectively ($|J-I| \leq F \leq |J+I|$). For the bosonic isotope ^{88}Sr where $I = 0$, J replaces F ($F = J$). Therefore, any discussion involving F_j throughout this text only applies to ^{87}Sr. The quantization axis is assumed to be along $\boldsymbol{e}_z$, and $\boldsymbol{\epsilon}$ is the complex polarization vector of the applied laser at frequency ω. From Eqn. (4.5), we can see that *the scalar component does not depend on the polarization, while the vector and tensor components do.*

The scalar, vector, and tensor parts themselves can be written as sums over all hyperfine states F_j in the excited fine structure state [116, 115]

$$\begin{aligned}
\alpha_g^s(j;\omega) &= \sum_{F_j} \frac{2}{3} g_{j,F_j}^{(0)}(\omega) |D_{j,F_j}|^2, \\
\alpha_g^v(j;\omega) &= \sum_{F_j} (-1)^{F+F_j+1} \sqrt{\frac{6F(2F+1)}{F+1}} \\
&\qquad \times \begin{Bmatrix} 1 & 1 & 1 \\ F & F & F_j \end{Bmatrix} g_{j,F_j}^{(1)}(\omega) |D_{j,F_j}|^2, \\
\alpha_g^t(j;\omega) &= \sum_{F_j} (-1)^{F+F_j} \sqrt{\frac{40F(2F-1)(2F+1)}{3(F+1)(2F+3)}} \\
&\qquad \times \begin{Bmatrix} 1 & 1 & 2 \\ F & F & F_j \end{Bmatrix} g_{j,F_j}^{(2)}(\omega) |D_{j,F_j}|^2.
\end{aligned} \tag{4.6}$$

Scaling of the polarizability terms as a function of laser detuning is encapsulated in the detuning factors

$$\begin{aligned}
g_{j,F_j}^{(K)}(\omega) &= \frac{1}{2\hbar} \mathrm{Re}\left(\frac{1}{\omega_{j,F_j} - \omega - \frac{i}{2\tau_j}} + \frac{(-1)^K}{\omega_{j,F_j} + \omega + \frac{i}{2\tau_j}} \right) \\
&\approx \frac{1}{2\hbar} \left(\frac{1}{\omega_{j,F_j} - \omega} + \frac{(-1)^K}{\omega_{j,F_j} + \omega} \right)
\end{aligned} \tag{4.7}$$

where ω_{j,F_j} is the transition frequency from the ground to the excited hyperfine state F_j, τ_j is the excited state lifetime ($1/A_{T_j}$), and $K = 0, 1, 2$ for scalar, vector, and tensor polarizabilities, respectively [116, 115]. Because we work in the far-detuned regime to find ω_t, we can ignore the imaginary terms in the denominators of Eqn. (4.7), which we have confirmed numerically. The detuning factor is identical for the scalar and tensor polarizabilities, but the counter-rotating term for the vector polarizability changes its sign.

All polarizability terms scale with the modulus-squared of the reduced matrix element

associated with the corresponding dipole transition

$$|D_{j,F_j}|^2 = |\langle g, F \| D \| j, F_j \rangle|^2. \tag{4.8}$$

Since the $^1S_0$ state of ^{87}Sr has a single hyperfine state and there exists only one decay path, the situation greatly simplifies and the reduced matrix element can be expressed in terms of the excited state lifetime τ_j as

$$|D_{j,F_j}|^2 = \frac{3\pi\epsilon_0\hbar c^3}{\omega_{j,F_j}^3 \tau_j}(2J_j+1)(2F_j+1)\begin{Bmatrix} J & J_j & 1 \\ F_j & F & I \end{Bmatrix}^2. \tag{4.9}$$

4.1.1 $^1S_0$ tune-out frequency of ^{88}Sr

Let us finally apply the expressions we have derived to calculate the tune-out frequency of ^{88}Sr. Due to the absence of hyperfine structure, the situation strongly simplifies for the case of ^{88}Sr. Replacing F (F_j) with J (J_j) where J=0 ($J_j = 1$ for both $^1P_1$ and $^3P_1$ contributions) in Eqn. (4.6), the vector and tensor polarizabilities vanish and only the scalar component remains. The resulting polarizability is

$$\begin{aligned}\alpha_g = \alpha_g^s &= \frac{3\pi\epsilon_0\hbar c^3}{\omega_{^1P_1}^3 \tau_{^1P_1}}\left(\frac{1}{\omega_{^1P_1}-\omega}+\frac{1}{\omega_{^1P_1}+\omega}\right)+\frac{3\pi\epsilon_0\hbar c^3}{\omega_{^3P_1}^3 \tau_{^3P_1}}\left(\frac{1}{\omega_{^3P_1}-\omega}+\frac{1}{\omega_{^3P_1}+\omega}\right) \\ &= \frac{6\pi\epsilon_0\hbar c^3}{\omega_{^1P_1}^2 \tau_{^1P_1}}\left(\frac{1}{\omega_{^1P_1}^2-\omega^2}\right)+\frac{6\pi\epsilon_0\hbar c^3}{\omega_{^3P_1}^2 \tau_{^3P_1}}\left(\frac{1}{\omega_{^3P_1}^2-\omega^2}\right).\end{aligned} \tag{4.10}$$

Each contribution of $^1P_1$ and $^3P_1$ Eqn. (2.6) retains the same form as the classical form we discussed in Section. 2 (Eqn. (2.6)) due to the fact that the upper levels only decay to g and the simple structure of $^1S_0$ ground state that has $J = 0$. Neglecting the small contributions from $\alpha_g(v';\omega)$ and $\alpha_g(c;\omega)$, the tune-out frequency occurs when $\alpha_g(^1P_1;\omega)$ balances $\alpha_g(^3P_1;\omega)$, thus it lies in-between $\omega_{^1P_1}$ and $\omega_{^3P_1}$. Since $\tau_{^1P_1} \ll \tau_{^3P_1}$, the tune-out frequency occurs very close to $\omega_{^3P_1}$ to cancel out the contribution from $^1P_1$. For this reason, a better way to denote the tune-out frequency is its detuning from $\omega_{^3P_1}$: $\Delta_t = \omega_t - \omega_{^3P_1}$.

To calculate the tune-out detuning precisely, we also need the knowledge of the core and remaining valence contributions. Our theory collaborators, M.S. Safronova's and S.G. Porsev's, performed these calculations. They calculated the valence contributions of α_g by solving the inhomogeneous equation as described in Refs. [120, 121]. Then, using the sum-over-states formula Eqn. (4.6), we extracted the contributions of the $^1P_1$ and $^3P_1$ states and determined the remaining valence contributions, $\alpha_g(v', \Delta_t) = 6.57(14)$ a.u. The core part of the polarizability, $\alpha_g(c;\Delta_t)$, was also calculated by them using the single-electron approximation including random-phase approximation corrections [122] to be $\alpha_g(c;\Delta_t) = 5.30(5)$ a.u.

Combining all, we obtain $\Delta_t = 143.796$ GHz for ^{88}Sr. For $\omega_{^1\mathrm{P}_1}$ and $\omega_{^3\mathrm{P}_1}$, we use the values from Ref. [123] and [124], respectively. The ^{1}S$_0$-^{3}P$_1$ transition frequency ($\omega_{^3\mathrm{P}_1}$) has been measured directly with a 10 kHz precision, and the precise knowledge of $\omega_{^1\mathrm{P}_1}$ is not necessary because Δ_t is far de-tuned from it. Using our wavemeter, we measure $\omega_{^1\mathrm{P}_1}$ that is $\sim 2\pi\times$ 500 MHz away from the reported value in Ref. [123]; however, this discrepancy shifts Δ_t less than $2\pi\times1$ MHz. However, the lifetimes $\tau_{^1\mathrm{P}_1}$ and $\tau_{^3\mathrm{P}_1}$ are *critical* in determining Δ_t. For these lifetimes, we use the measured values from Ref. [125] and Ref. [56] for $\tau_{^1\mathrm{P}_1}$ and $\tau_{^3\mathrm{P}_1}$, respectively. The former value was measured using photoassociative spectroscopy [125], and the latter has been measured directly by measuring the photons collected from ^{3}P$_1$ decaying to ^{1}S$_0$ [56].

4.1.2 ^{1}S$_0$ tune-out frequency of ^{87}Sr

We have shown above that the hyperfine structure of ^{87}Sr make the polarizability calculation more complicated. Let us know find out by how much Δ_t changes due to the hyperfine structures. The two excited states of interest ^{1}P$_1$ and ^{3}P$_1$ both have $J_j = 1$, and thus have the same three hyperfine states $F_j = 7/2$, $9/2$, and $11/2$. For this reason, the scalar, vector, and tensor polarizabilities only differ in the group-theoretic numerical prefactors associated with the excited states, except for the slightly different detuning dependence of the vector polarizability.

Note that ω_{j,F_j} can be expressed in terms of the (hypothetical) hyperfine-free transition frequency $\bar{\omega}_j$ and the hyperfine shift Δ_{j,F_j} as $\omega_{j,F_j} = \bar{\omega}_j + \Delta_{j,F_j}$. The hyperfine shift can be calculated from the magnetic dipole interaction constant A_j and the electric quadrupole interaction constant Q_j as [65, 71]

$$\begin{aligned} \Delta_{j,F_j} &= \frac{A_j}{2}K_j + \frac{Q_j}{4}\frac{\frac{3}{2}K_j(K_j+1) - 2I(I+1)J_j(J_j+1)}{I(2I-1)J_j(2J_j-1)}, \\ K_j &= F_j(F_j+1) - J_j(J_j+1) - I(I+1), \end{aligned} \tag{4.11}$$

where J_j is the electronic angular momentum of the excited state. We use the hyperfine constants $A_{^1\mathrm{P}_1} = -2\pi \times 3.4(4)$ MHz, $Q_{^1\mathrm{P}_1} = 2\pi \times 39(4)$ MHz, $A_{^3\mathrm{P}_1} = -2\pi \times 260.084(2)$ MHz, and $Q_{^3\mathrm{P}_1} = -2\pi\times35.658(6)$ MHz, summarized in Ref. [65]. The isotope shift of $\bar{\omega}_{^3\mathrm{P}_1}$ was measured recently in Ref. [105]: the hyperfine-free transition frequency of ^{1}S$_0$-^{3}P$_1$ in ^{87}Sr is red detuned by 62.1865(123) MHz from the transition frequency in ^{88}Sr [124]. As previously mentioned, the ^{1}S$_0$-^{1}P$_1$ transition frequency does not need to be as precise and is obtained from Ref. [123]. The isotope shift on this transition does not influence the calculations, as will be shown below.

To study the contributions from each component in detail, we dig deeper into the scalar, vector, and tensor polarizabilities of the ^{87}Sr ^{1}S$_0$ state. By specializing the prefactors, we

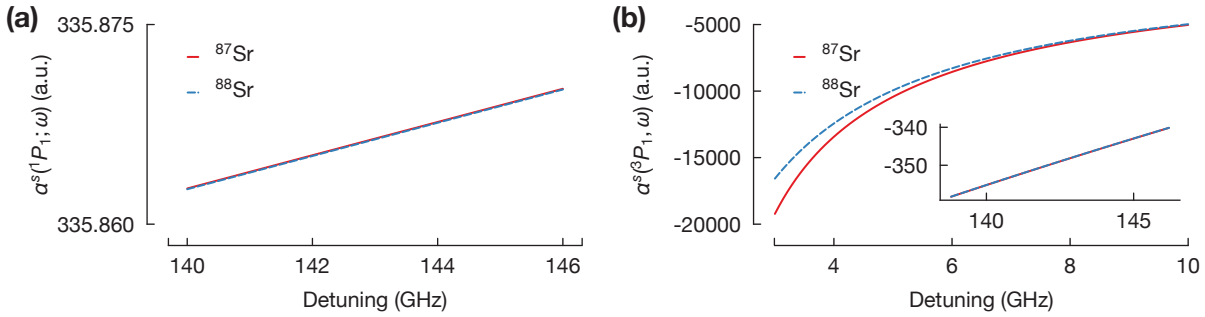

Figure 4.1 Comparison of $\alpha_g^2(\omega)$ for ^{87}Sr and ^{88}Sr near Δ_t. (a) The ^{1}P$_1$ scalar contribution as a function of detuning from the ^{1}S$_0$-^{3}P$_1$ transition. For the case of ^{87}Sr, the detuning is referenced with respect to $\bar{\omega}_{^3\mathrm{P}_1}$, which includes the isotope shift. (b) same as (a) but with the ^{3}P$_1$ contribution. The inset shows $\alpha^s(^3\mathrm{P}_1;\omega)$ at the detuning range relevant to Δ_t.

re-write the reduced matrix elements as

$$|D_{j,F_j}|^2 = \frac{3\pi\epsilon_0\hbar c^3}{\omega_{j,F_j}^3\tau_j}[4/5, 1, 6/5], \tag{4.12}$$

where the numerical factors in the square brackets correspond to $F_j = 7/2$, $9/2$, and $11/2$, respectively. As expected, this means that the lifetime τ proportionally scales up scalar, vector, and tensor polarizabilities. Bringing it all together, we find

$$\begin{aligned}
\alpha_g^s(j;\omega) &= 2\sum_{F_j}\frac{3\pi\epsilon_0\hbar c^3}{\omega_{j,F_j}^3\tau_j}\left[\frac{4}{15},\frac{5}{15},\frac{6}{15}\right]g_{j,F_j}^{(0)}(\omega),\\
\alpha_g^v(j;\omega) &= \sum_{F_j}\frac{3\pi\epsilon_0\hbar c^3}{\omega_{j,F_j}^3\tau_j}\left[-\frac{44}{55},-\frac{10}{55},\frac{54}{55}\right]g_{j,F_j}^{(1)}(\omega),\\
\alpha_g^t(j;\omega) &= \frac{\sqrt{2}}{3}\sum_{F_j}\frac{3\pi\epsilon_0\hbar c^3}{\omega_{j,F_j}^3\tau_j}\left[-\frac{88}{165},\frac{160}{165},-\frac{72}{165}\right]g_{j,F_j}^{(2)}(\omega).
\end{aligned} \tag{4.13}$$

Therefore, finding Δ_t for ^{87}Sr is more complicated due to the vector and tensor components, thus Δ_t is also dependent on the laser polarization.

4.1.3 Far-detuned regime at Δ_t: $\alpha_g(\omega)$ of ^{88}Sr vs ^{87}Sr

To get an intuitive picture of how the hyperfine structure changes $\alpha_g(\omega)$, we compare the $\alpha_g(\omega)$ of ^{87}Sr and ^{88}Sr at the far-detuned regime from both $\omega_{^1\mathrm{P}_1}$ and $\omega_{^3\mathrm{P}_1}$, which is in fact the case for Δ_t. For this, we approximate $|D_{j,F_j}|^2$ of ^{87}Sr to $\approx \frac{3\pi\epsilon_0\hbar c^3}{\bar{\omega}_j^3\tau_j}[4/5, 1, 6/5]$ to pull $\frac{3\pi\epsilon_0\hbar c^3}{\omega_{j,F_j}^3\tau_j}$ out of the sum in Eqn. (4.13). After this approximation, we see that both vector and tensor polarizabilities sum to zero when we are in the far-detuned regime

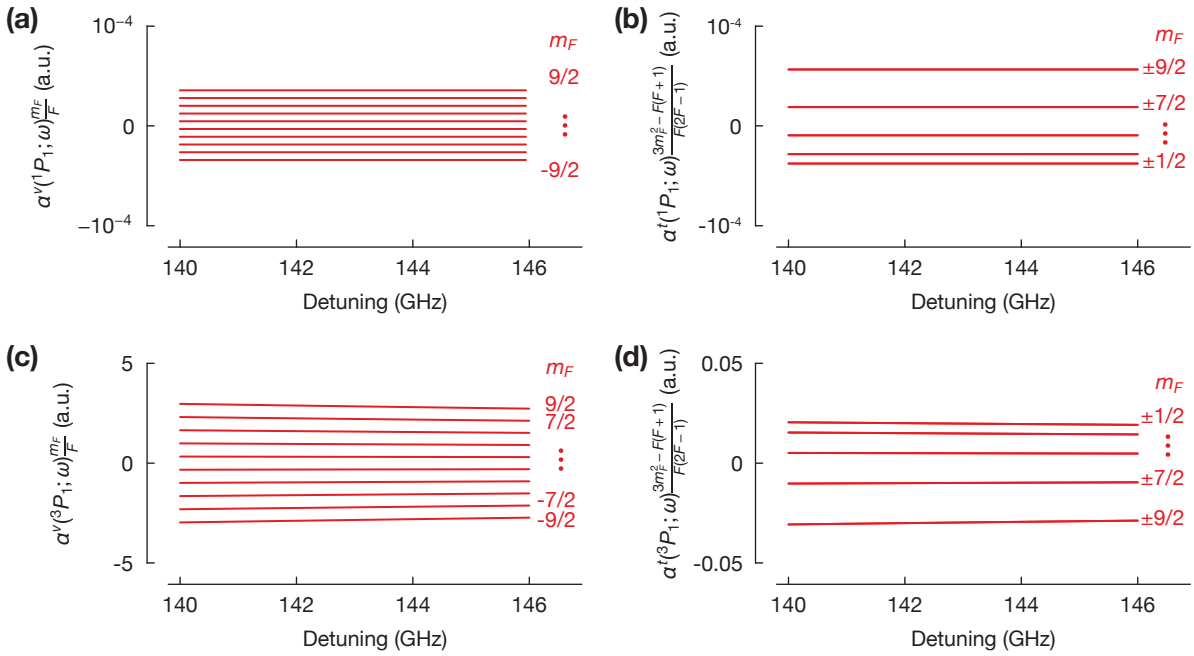

Figure 4.2 Comparison of $\alpha_g^v(\omega)$ and $\alpha_g^t(\omega)$ for ^{87}Sr and ^{88}Sr near Δ_t. (a) the ^{1}P$_1$ vector contribution as a function of detuning from the ^{1}S$_0$-^{3}P$_1$ transition for different m_F states (Eqn. (4.6)). We assume the beam ellipticity of 1 to show the upper limit. (b) the ^{1}P$_1$ tensor contribution (Eqn. (4.6)) as a function of detuning from the ^{1}S$_0$-^{3}P$_1$ transition for different m_F states. Here, we assume a linear polarization to show the upper limit. (c)-(d) same as (a)-(b), but from the ^{3}P$_1$ contributions.

compared to the hyperfine structure, where the detuning factor contributes equally, and can be pulled out of the sum. In this regime, the only contribution that survives is the scalar polarizability. For the same reason, we also expect negligible differences in α^s between the two isotopes in this regime. The scalar polarizability component of ^{1}P$_1$ and ^{3}P$_1$ of the two isotopes are illustrated in Fig. 4.1(a) and (b), respectively, as a function of the detuning from the ^{1}S$_0$-^{3}P$_1$ transition. In Fig. 4.1 (b), we see that they become indistinguishable as the detuning increases (the plot was generated based on Eqn. (4.13) without the approximation on $|D_{j,F_j}|^2$). Note that the detuning for ^{87}Sr is referenced with respect to $\bar{\omega}_j$, which takes the isotope shift into account.

Next, we take a closer look at each contribution in the detuning range relevant to Δ_t without any approximation. Comparing Fig. 4.2(b)-(c) and (e)-(f), the ^{1}P$_1$ tensor and vector contributions are more than two orders of magnitude smaller than the contributions from the ^{3}P$_1$ state, since the frequency of ω_t is more than a few hundred THz detuned from the ^{1}S$_0$-^{1}P$_1$ transition. For this reason, we can ignore the vector and tensor contributions to $\alpha_g(^1\mathrm{P}_1;\omega)$ and set $\alpha_g(^1\mathrm{P}_1;\omega) = \alpha_g^s(^1\mathrm{P}_1;\omega)$.

With this simplification, we analyze the difference of the ^{87}Sr and ^{88}Sr tune-out detun-

$\alpha_g(^3\mathrm{P}_1, \omega)$	$\delta\Delta_t = \Delta_t^{87} - \Delta_t^{88}$
$\alpha_g^s(^3\mathrm{P}_1; \omega)$	$+2\pi \times 8$ MHz
$\alpha_g^v(^3\mathrm{P}_1; \omega)$	$-2\pi \times 23$ MHz $\leq \delta\Delta_t \leq +2\pi \times 23$ MHz
$\alpha_g^t(^3\mathrm{P}_1; \omega)$	$-2\pi \times 2$ MHz $\leq \delta\Delta_t \leq +2\pi \times 12$ MHz

Table 4.1 Comparison of the ^{87}Sr and ^{88}Sr tune-out detuning: Δ_t^{87} was numerically computed considering the contributions shown in the left column. For the vector and tensor contributions, the shift was calculated for the stretched $|m_F| = F$ states and we show the corresponding ranges. A beam ellipticity of 2% was used for the vector shifts and we assumed perfect (maximum) polarization alignment for the tensor shifts.

ing Δ_t due to the hyperfine structure. Table 4.1 shows the shifts due to scalar, vector, and tensor polarizabilities. For the calculations due to the vector polarizabilities, we used an upper limit on the beam ellipticity of 2%, and assumed perfect alignment of $\boldsymbol{\epsilon} \cdot \boldsymbol{e}_z = 1$ to evaluate the tensor polarizability. The shifts depend on the m_F states (Eqn. (4.6)), and we show the maximum ranges of the shift as a worst case estimate. In the experiment, we do not spin-polarize the sample, and we likely work with an equal population among all m_F states. As a conservative estimate, we use the full span due to the vector shift to estimate differential shifts between the measured tune-out detuning Δ_t^{88} for ^{88}Sr and the tune-out detuning Δ_t^{87} for ^{87}Sr.

4.2 Measurement summary

After having calculated the expected Δ_t and understood the main contributors to this value, let us recap the goals that we mentioned in the beginning of the chapter were to (1) precisely determine Δ_t, (2) to measure $\alpha_e(\omega)$ at Δ_t, (3) implement the state-dependent lattice created at Δ_t. To achieve the above goals, we used the following methods described in detail [82]:

(1) We loaded $\sim \mu$K-cold thermal atoms in an incommensarate 1D lattice composed of a deep magic-wavelength (813 nm) lattice and a shallow lattice created by the light near the tune-out wavelength (689.2 nm). Here, the deep lattice was generated by retro-reflecting 290 mW of 813 nm light, making a lattice with a longitudinal trap frequency ($\nu_t = \omega_t/2\pi$) of $\sim$40 kHz, and the shallow tune-out lattice was generated by retro-reflecting the beam with a power of 4.5 mW. Once the atoms were loaded, we intensity modulated the shallow lattice at $2\nu_t$ causing parametric heating [126] that resulted in transitions between lattice bands that are two motional quanta apart. This heating causes atom loss from the lattice. We measured the corresponding induced loss rate at particular detuning of the shallow lattice by measuring the atom number as a function of modulation time. When repeating such measurements at different detunings of the shallow lattice, one would expect the loss rate to approach 0 at Δ_t. Thus, by measuring the detuning where

the heating rate diminishes, we determined Δ_t. This simple method is distinct from conventional methods that typically use atom interferometers based on thermal atoms [127–130] or quantum degenerate gases [30, 84, 131, 132], and allows long interrogation times and applicability to atoms in excited states, molecules, and trapped ions. We performed the above measurements for both ^{88}Sr and ^{87}Sr.

(2) Once Δ_t was determined using the above method, we were ready to measure $\alpha_e(\omega_t)$. For this measurement, we turn off the shallow lattice and only trap the atoms in the deep lattice. Then, we performed the clock spectroscopy using ^{87}Sr, measuring the carrier frequency, in the presence of a laser beam ω_t as a function of beam power. Such a beam shifts the frequency of the carrier peak given by the ac-Stark shift that is proportional to $\alpha_e(\omega_t)$ and the intensity of the beam. We calibrate the intensity by measuring the free-space Rabi oscillations on the ^{1}S$_0$-^{3}P$_1$ transition using a resonant beam that had been merged with the Stark-shifting beam in the same optical path.

(3) We excited ^{87}Sr g atoms trapped in the deep magic lattice to e by applying a 10-ms-long adibatic-rapid-passage pulse. Then, we transferred them to the tune-out lattice with $\nu_t \sim 40$ kHz by diabatically turning on the tune-out lattice beam, followed by ramping down of the magic-wavelength lattice after 1 ms. Then, we measure the number of atoms as a function of lattice hold time to extract the lifetime of e atoms in the tune-out lattice.

The results of our goals (1),(2), and (3) as follows:

(1) We obtained $\Delta_t = 143.009\ \text{GHz} \pm (8\ \text{MHz})_{\text{stat}} \pm (2\ \text{MHz})_{\text{sys}}$ and $\Delta_t = 142.86\ \text{GHz} \pm (80\ \text{MHz})_{\text{stat}} \pm (2\ \text{MHz})_{\text{sys}}$ for ^{87}Sr for ^{88}Sr and ^{87}Sr, respectively. We attribute the larger uncertainty in Δ_t of ^{87}Sr due to worse data quality due to the two-body decay collisions. The small difference of Δ_t of ^{87}Sr and ^{88}Sr is expected due to the hyperfine structure of ^{87}Sr.

(2) We obtained $\alpha_e(\omega_t) = 1555 \pm 8_{\text{state}} \pm 2_{\text{sys}}$ a.u.. To the best of our knowledge, this is the first time in which the alkali-earth atom's excited state polarizability has been measured.

(3) The measured lifetime of e in a tune-out state-dependent lattice agrees well with the theoretically predicted loss due to photon scattering for each lattice axis of 24 s per recoil of lattice depth. Depending on the application, a compromise between lattice depth and tunneling rate needs to be found. For instance, a two-dimensional tune-out lattice trapping e atoms in a Mott insulator state would have a lifetime $\sim$1 s.

4.3 Atomic lifetime determination

One might have noticed that our measured value of ^{88}Sr Δ_t does not agree with the value that was calculated in Sec 4.1.1. This calculation used the values of $\tau_{^1\text{P}_1}$ and $\tau_{^3\text{P}_1}$ that

were measured in Ref. [125] and [56], respectively. Now, we can turn this calculation around to estimate $\tau_{^1\mathrm{P}_1}$, which was measured only in an indirect manner in Ref. [125], by combining our data and the directly measured value of $\tau_{^3\mathrm{P}_1}$ [56] into a rearrangement of Eqn. (4.10):

$$\tau_{^1\mathrm{P}_1} = \frac{-6\pi\epsilon_0 c^3}{[\alpha_g(v;\omega_t) + \alpha_g(c;\omega_t) + \alpha_g^s(^3\mathrm{P}1,\omega_t)]\omega_{^1\mathrm{P}_1}^2(\omega_{^1\mathrm{P}_1}^2 - \omega_t^2)} \tag{4.14}$$

Doing this calculation gives a value of $\tau_{^1\mathrm{P}_1}$ =5.234(8) ns, which has a 7σ discrepancy with the currently accepted value of $5.263(4)$ ns [125].

We highlight that the currently best values for $\tau_{^3\mathrm{P}_1}$ and the lifetime of the $^3\mathrm{D}_1$ state are correlated because they are extracted from a single dataset [125]. The $^3\mathrm{D}_1$ lifetime directly determines the dynamic contribution to the strontium lattice clock blackbody radiation shift [121], its currently largest systematic uncertainty [133]. This uncertainty can be directly improved by a new direct measurement of $\tau_{^1\mathrm{P}_1}$ in combination with our results and Ref. [56].

Moreover, the precise measurement of $\alpha_e(\omega_t)$ can be used to extract the $^3\mathrm{P}_1$-$^3\mathrm{S}_1$ lifetime because this transition is the main contributor to the $\alpha_e(\omega_t)$ (87%). With help of M.S. Safronova and S.G. Porsev, we extracted $\tau_{^3\mathrm{S}_1}$13.92(11) ns. This precision of our calculated value is an order of magnitude improvement compared to prior measurements that ranged from 10.9(1.1) ns to 15.0(8) ns [134–136].

4.4 Conclusion

In this chapter, we presented detailed calculations of the tuneout wavelengths of g of both fermionic and bosonic isotopes of Sr. We showed in particular how, even though the hyperfine structure of ^{87}Sr complicates the calculation, a light with small ellipticity (2%) results in the the tune-out frequency of ^{87}Sr and ^{87}Sr being within $\sim$ 50 MHz of each other. Implementing the state-dependent lattice in our simulator, we demonstrated high-fidelity, state-dependent control of the strontium optical qubit. Combining our results with single-site addressing and control [137] removes the main obstacle for the realization of quantum computation and quantum simulation schemes with two-electron atoms [21], and opens the path to the simulation of new types of physical systems as described in Section 2.7.

Chapter 5

Cavity-enhanced two dimensional optical lattices

In this chapter, we discuss the extension of our experimental apparatus to support the build-up cavities. With the extended setup, we demonstrate the largest 2D optical lattices to date with a mode area close to $1\ \mathrm{mm}^2$ that can trap neutral atoms in both high- and low-intensity lattice regimes. We achieve this mode area by generating the lattices in optical cavities with large mode diameters to enhance optical power [41]. Notably, this enhancement can be done at any wavelength of interest, even those for which the available laser power is limited, while keeping the mode area constant, and our cavity is coated for multiple wavelengths. We demonstrate the advantage of this flexibility by creating our lattices at an unconventional wavelength of 914 nm such that our mode area is more than an order of magnitude larger than what is possible in free space using conventional setups and current laser technology. While other cavity-enhanced lattices for similar purposes have been constructed in the past [138, 139, 93], our cavities have a factor of 3.5 larger mode area than the largest cavity-enhanced lattices [93], while achieving more than two orders of magnitude longer trap lifetime. Our cavity assembly is a monolithic device that contains two independent perpendicular optical cavities that cross at right angles, as shown in the photograph in Fig. 5.1(a), leading to a high degree of mechanical and thermal stability. We will first briefly summarize the cavity's monolithic design and its integration into our vacuum system.

We characterize these cavity lattices by loading strontium atoms and performing clock spectroscopy at a wavelength where the differential light shift of the clock states is large in high-intensity lattices. We observe spatially dependent clock excitation with resolved carrier and sideband transitions. These features let us directly map the lattice potential envelope, shown in Fig. 5.1(b) and (c). With the measured potential, we quantify the size and homogeneity of the created potential. Furthermore, we use these features to measure local temperatures and the polarizability ratio between the two clock states with high precision. Finally, the monolithic cavity design results in a long atom lifetime in the cavity lattices and an excellent stability of the experimental setup.

5.1 Science chamber

The main and science chambers are connected by a pneumatic valve and bellow. We attach a bellow in between to relieve any mechanical constrain between the two chambers' assemblies (in Fig. 3.2, the bellow is replaced by a nipple just for illustration). The

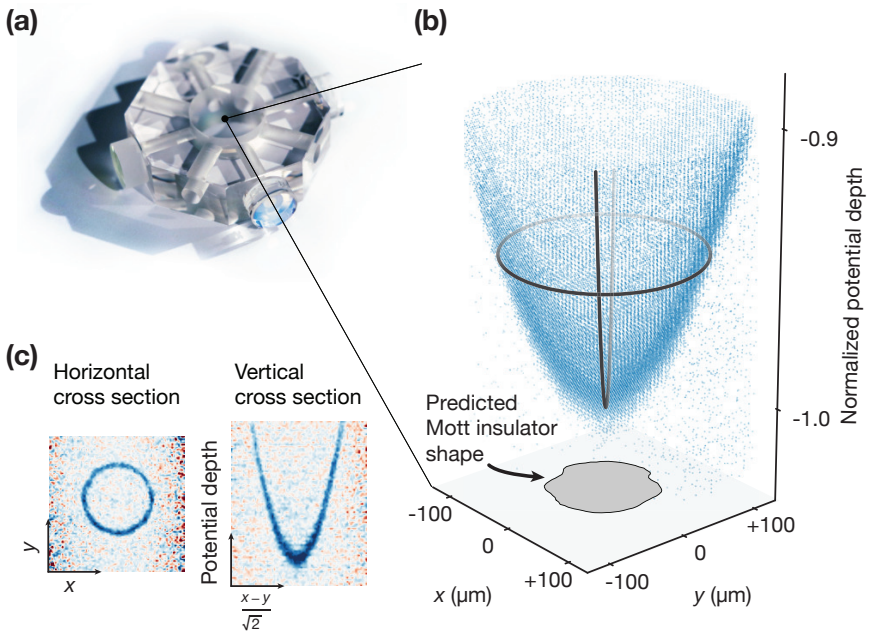

Figure 5.1 (a) Photograph of the monolithic cavity assembly. The two-dimensional optical lattice is formed at the intersection of the optical axes of both cavities. (b) From the measured potential envelope of the optical lattice, we confirm that each cavity supports a fundamental TEM_{00} mode with $1/e^2$ waist of $489(8)\ \mu\mathrm{m}$ at $914.3\ \mathrm{nm}$. A Mott insulator of strontium atoms created in an optical lattice with this potential envelope is expected to form in the shaded area, which has a diameter $\sim 125\ \mu\mathrm{m}$. (c) Cross sections through the experimental data corresponding to horizontal and vertical lines drawn in panel (b). The details of (b) and (c) will be explained in Sect. 5.5.

science chamber is a custom designed steel chamber whose design specifications are described in [55]. Since the cavities are in vacuum and the quantum simulations will take place in the science chamber, we put significant effort into designing the system to reach an ultra high vacuum lower than in the MOT chamber. First of all, we put two ion and non-evaporative-getter (NEG) combination pumps on each side of the science chamber. In addition, we also coated the inside of the science chamber with NEG.

bake-out For the bake-out, we isolated the main chamber and science chambers as best as possible by placing metal walls in between the two sections as shown in Fig. 5.2(a). The junctions between the walls were taped such that any small fiber glasses cannot travel to the main chamber section. With this, we were able to bake the science chamber without removing any of the existing optics. The bake-out procedure was not trivial due to the presence of NEG pumps that activate at different temperatures. The NEG coating of the science chamber can be activated starting from temperatures as low as $200\ ^\circ\mathrm{C}$ (although a higher activation temperature is recommended) whereas the activation of the NEG on the combination pumps heats the pumps as hot as $500\ ^\circ\mathrm{C}$. Because both activations generate significant heat, which greatly increases pressure in the chamber, we wanted to make sure that activating one does not saturate the other.

In next paragraphs, we explain in detail the bake-out procedure which led to a final pressure that was below the operating range of the ion pressure gauge ($< 5\times10^{-11}$ mbar). The pressure and temperature logs at each step is shown in Fig. 5.2.

① After the complete assembly, we first baked out the chamber at a low temperature of at $120\ ^\circ\mathrm{C}$ for 2-3 days to get rid of water that deposited during the assembly process. We chose this low temperature to not activate any of the NEG coatings.

② After this initial bake-out, we lowered the temperature and confirmed that the pressure is lower than before the bake-out. At this point, we measured a pressure of 3×10^{-10} mbar.

③ We degassed the ion pumps by turning them on and off several times. Surprisingly, the degassing process increased the pressure by two orders of magnitude.

④ After making sure the ion pumps are off, we began the next bake-out process to activate the NEG coatings in the science chamber. Prior to the assembly, we had tested the performance of the coating in a preparatory lab. At that time, we attached blanks instead of viewports, and we activated the coating by heating the chamber to $300\ ^\circ\mathrm{C}$ for $33\ \mathrm{hrs}$. However, with the real assembly, we could not bake as high due to the low heat load that the viewports can take. Therefore, we baked at $180\ ^\circ\mathrm{C}$ but for the significantly longer duration of a week to ensure activation.

⑤ After a week, we also activated the NEG coatings of the combination pumps. Activating these coatings takes only about an hour and, during the activation, the top part of the pumps heats up to $500\ ^\circ\mathrm{C}$. To make sure that this heat does not raise the

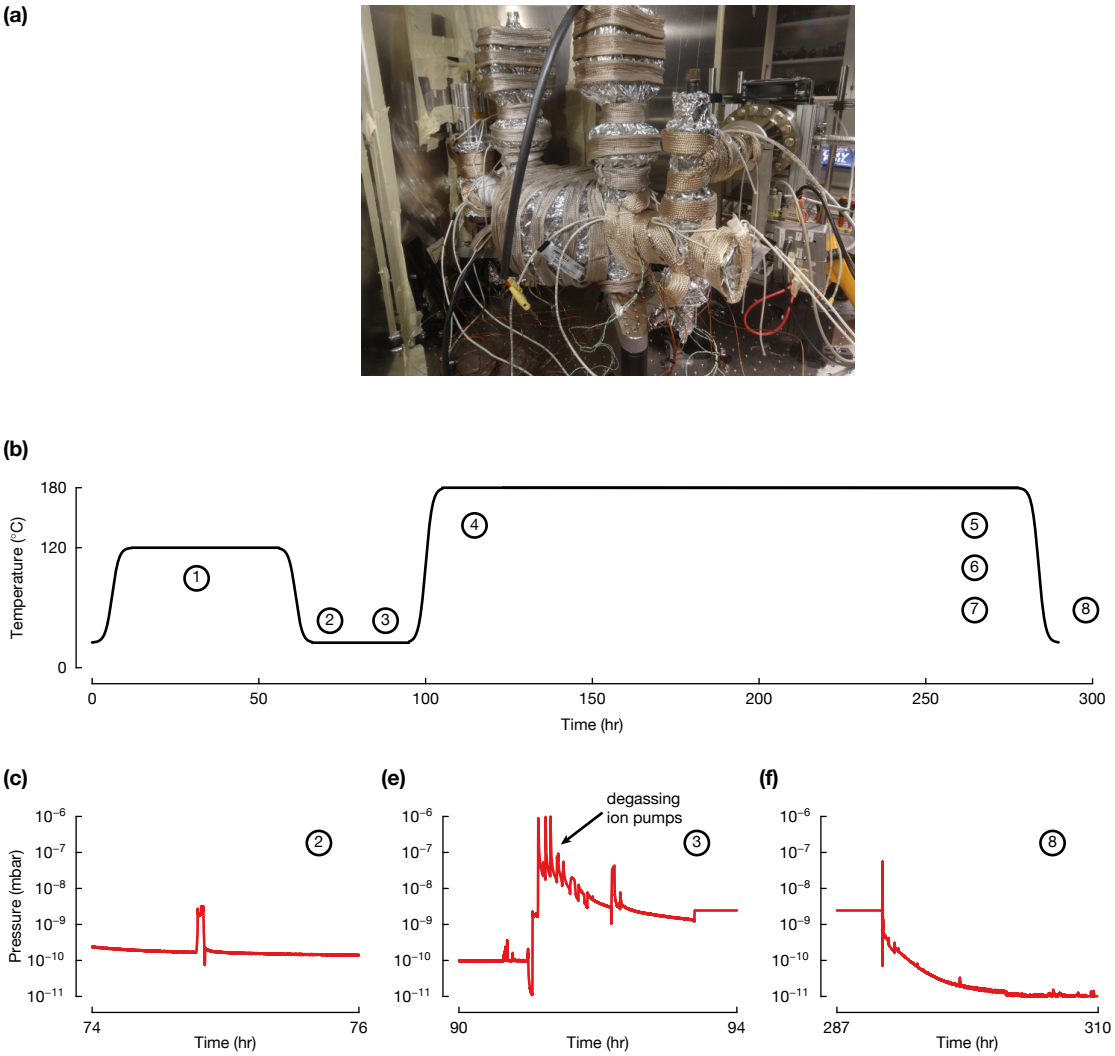

Figure 5.2 Overview of the bakeout process. (a) Photograph of the science chamber being baked. (b) Set temperature plot during the bake-out process. (c) Pressure inside the chamber measured by an ion pressure gauge during the bake-out process. The numbering on the plots corresponding to the baking steps listed in the above text.

temperature of the whole chamber, we unwrap the heating tapes and aluminium foils to let the top part cool down to $60\ ^{\circ}\mathrm{C}$ before the activation.

⑥ After degassing the ion pumps once more, we started the activation for an hour.

⑦ Once the activation stopped and the top parts cooled down to $\sim 200\ ^{\circ}\mathrm{C}$, we also cooled down the rest of the heating.

⑧ Then, we turned on the ion pumps and we had to manually change the output voltage of the ion pumps from $7\ \mathrm{kV}$ to $3\ \mathrm{kV}$ using the controller as the pressure dropped. At the end, we measured a pressure as low as 2×10^{-11} mbar; however, it should be noted that the gauge's minimum range is 5×10^{-11} mbar.

5.2 Crossed Cavities

In contrast to existing buildup cavities, we use a monolithic assembly that is both thermally and mechanically stable, without any movable parts [41], as shown in Fig. 5.1(a). In brief, we have optically contact two pairs of mirrors to an octagon-shaped spacer made from ultra-low expansion glass, forming two cavities that overlap in the center of the spacer. The spacer has bores with different diameters for optical access and high-resolution imaging. By using an interferometric method [41], we have achieved a near-perfect vertical overlap between the two modes.

After construction and characterization, the assembly was mounted in a stainless steel vacuum chamber attached to the vacuum system [39]. In Fig. 5.3(a), we show this science chamber featuring a pair of re-entrant viewports that allow high-resolution imaging of the atomic sample. The octagon-shaped cavity assembly is mounted to the top viewport in a stress-free manner [82] as sketched in the figure. After bake-out, we reach a pressure below $3 \times 10^{-11}\ \mathrm{mbar}$ in the science chamber, demonstrating that the cavity assembly is compatible with state-of-the-art ultra high vacuum chambers.

The cavity mirrors are optimized for quantum simulations with strontium atoms and are highly reflective at several selected wavelengths [41]. In the remainder of this work, we couple laser light at $914.3\ \mathrm{nm}$ into the cavities. At this wavelength, the finesse and intracavity enhancement are 5025(58) and 1132(13), respectively [41]. By coupling a moderate power of $\sim 80\ \mathrm{mW}$ into each arm, we create deep lattices with trap frequencies of $116\ \mathrm{kHz}$, corresponding to lattice depths of $60\ \mu\mathrm{K}$. We optimize the mode-matching of the input beams to each cavity's fundamental transverse electric field mode (TEM_{00}) to $\sim 99\%$ [41].

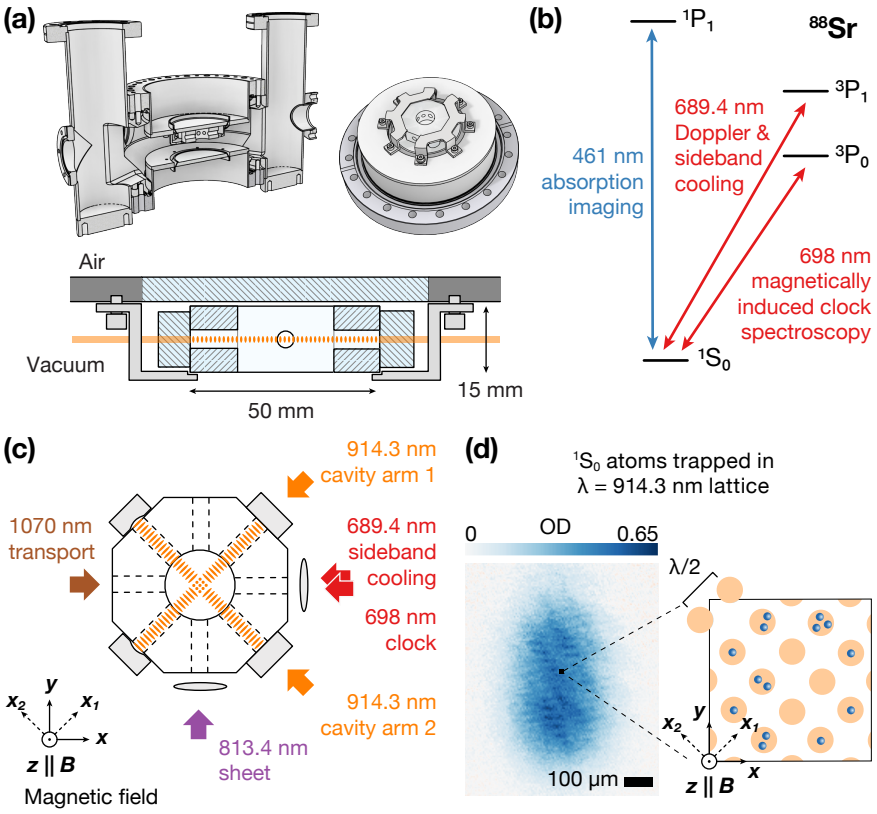

Figure 5.3 Overview of the experimental setup. (a) Cross section of the science chamber, which includes a pair of re-entrant viewports (top left). The cavity assembly rests in a stainless steel cage attached to the top viewport (top right). A simplified cross section cut of the cavity assembly and its mounting structure is shown at the bottom. (b) Simplified ^{88}Sr energy diagram and optical transitions used in the experiment. (c) Sketch of the laboratory and lattice coordinate frames and the relevant laser beams. ^{88}Sr atoms in the $^1S_0$ (g) state are transported into the assembly and are loaded into a trap created by the $914.3\ \mathrm{nm}$ cavity lattice beams and a light sheet at $813.4\ \mathrm{nm}$. The laser beam at $689.4\ \mathrm{nm}$ is used for direct sideband cooling, and the laser beam at $698\ \mathrm{nm}$ drives the clock transition induced by a bias magnetic field B along z. (d) *In-situ* absorption image of g atoms in the combined trap of the lattices and light sheet (left). On the right is an illustration showing the atoms occupying the lattice sites.

5.3 Laser System

5.3.1 Ti:Sapphire laser

The cavity lattice beams at $914.332\ \mathrm{nm}$ are generated from a Ti:Sapphire laser. The output of the laser is divided into four paths: a path for locking the laser's frequency to a pre-stabilization cavity, two paths for coupling into each cavity arm of the crossed cavity assembly, and an optical heterodyne beat setup with a femtosecond optical frequency comb. Locking the laser's frequency to a pre-stabilization cavity with piezo-tunable length allows us to keep the laser's frequency close to the resonance frequencies of the crossed cavities.

The length of the pre-stabilization cavity is actively stabilized by locking one of the resonance frequencies to the clock laser frequency with a Pound–Drever–Hall (PDH) lock. The clock laser itself is frequency stabilized to an ultra-stable reference cavity with a finesse of $\sim$280000. Once the length of the pre-stabilization cavity is stabilized, we lock the Ti:Sapphire laser's frequency to another of its resonances via the PDH technique as well. For this purpose, the error signal is fed back to a piezo attached to the Ti:Sapphire laser's bow-tie cavity mirrors.

The two beams that couple into the cavities are each frequency-shifted with separate double-pass acousto-optic modulators (AOMs) and then fiber-coupled to the optical setup for coupling into the cavities. The AOMs tune the frequency of each beam to the resonant frequency for each cavity. To maintain the desired frequency for each beam, we again use the PDH technique, and use the error signal to control the radio-frequency (rf) signal driving the AOMs. The two cavity are separated in frequency by $\sim 60\ \mathrm{MHz/FSR}$, where $\mathrm{FSR} = c/2L = 3\ \mathrm{GHz}$, where $L = 50\ \mathrm{mm}$ is the cavity length and c is the speed of light.

During the experiments, we actively stabilize the intensity of the laser beams coupled to the cavity. For this stabilization, we split off $\sim 1\%$ of each beam's power and send it onto a photodiode. The photodiode signal is compared to a DC signal to create an error signal which is then fed into a proportional-integral (PI) controller that actively controls the amplitude of the rf signals of the double pass AOMs. With this locking scheme, we control the intensity sent to the cavities. The input cavity beams can also be shut off rapidly by turning off the rf power. Disabling the frequency and intensity locks of the two cavity beams does not affect the frequency stability of the Ti:Sapphire laser, since its frequency is pre-stabilized.

To characterize the laser noise, we measure the relative intensity noise (RIN) of the laser under three different conditions: (1) when the laser frequency is locked only to the pre-stabilization cavity, (2) as in (1) but with additional frequency stabilization to the crossed cavities, and (3) the same as (2) but with intensity stabilization, where conditions (2) and (3) are measured after the transmission through the crossed cavity. In Fig. 5.4, we show such measurements for cavity 2. For comparison, we also measure the

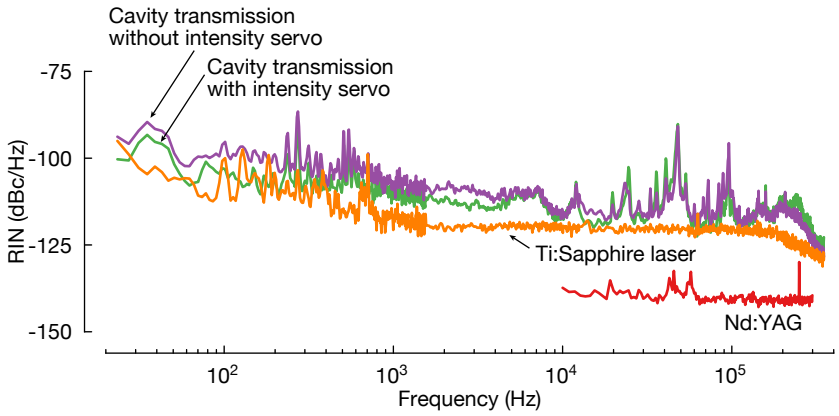

Figure 5.4 Characterization of laser noise. Relative intensity noise of the Ti:Sapphire laser (orange), transmission of cavity 2 with (green) and without (purple) intensity servo, compared with the relative intensity noise of a low-noise Nd:YAG laser (red).

RIN of a commercial low-noise Nd:YAG laser.

Finally, the optical heterodyne beat of the Ti:Sapphire laser and the optical frequency comb is used to monitor the absolute frequency of the laser. By simultaneously measuring this frequency and the frequency of the double-pass AOMs that are used for locking, we can determine the absolute frequencies of both crossed cavity modes used to trap the atoms. We use this to measure the long-term stability of our experimental setup which will be discussed later.

5.3.2 Transport laser setup

Once the atoms are cooled to few μK, we load them into an $1070\ \mathrm{nm}$ optical dipole trap and transport them from the main to science chamber, where the cavities are located. Since $^1S_0$ atoms are non-magnetic, optical transport by moving the focus of the beam is a natural choice rather using a magnetic field gradient. A traditional way of moving the focus is achieved by mechanically moving the stage where the lens is mounted. However, such a setup requires large spaces and a high degree mechanical stability of the moving parts. Instead, recently, an alternative choice of using a focus tunable lens was demonstrated in [140]. The details behind the working principle of the lens can easily found from company Optotune. In short, by applying electric current, one can tune the focal length of the lens. Therefore, the optical transport can be achieved in a compact setup without any moving parts.

As far as we are aware, there have not been any experiments involving optical transport of strontium. Therefore, we initially devised a setup that is optimal for loading a high number of ^{87}Sr and ^{88}Sr atoms. Unfortunately, we encountered several problems when

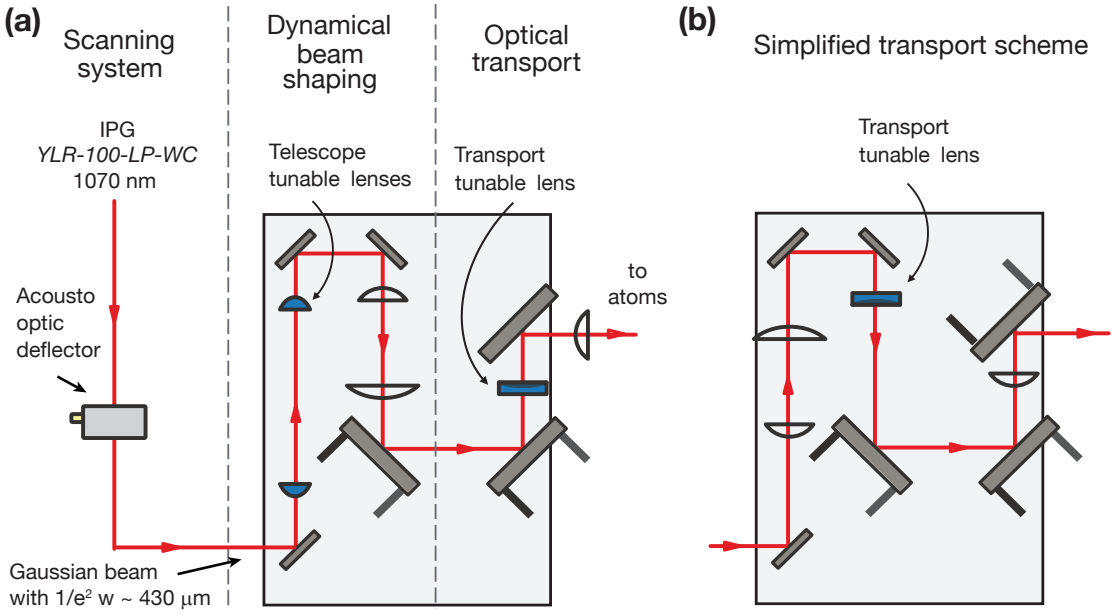

Figure 5.5 Transport setup (a) initial design: it consists of three tunable lenses and AOD to allow dynamical beam shaping (b) final design used in the current experiment. The beam is first expanded by a $\times 4$ telescope before reaching the negative focal length tunable focus lens.

implementing the setup experimentally, and we reverted to a much simpler setup. The simpler setup is far from being optimal in terms of the mode matching between the red MOT and the dipole trap, thus we believe it is worthwhile to discuss our initial setup and the problems we encountered for future considerations.

Initial setup

To optimize the loading to the dipole trap, we ideally would like to start with a dipole beam that matches the dimensions of the optimized red MOT. Unfortunately, the red MOT of ^{88}Sr and ^{87}Sr have very different shapes. The red MOT of ^{88}Sr sags along gravity, producing a pancake shaped MOT that is vertically compressed. The aspect ratio of the vertical and horizontal axes can be as large as 1:20 depending on a magnetic field gradient and laser detuning. On the other hand, the red MOT of ^{87}Sr does not sag and occupies a volume of an ellipsoid. For this case, the typical aspect ratio is 1:2. Therefore, we planned for a dipole beam setup where the beam aspect ratio can be smoothly varied. We would start with an elliptical beam whose aspect ratio can be expanded up to 1:20 and smoothly changed to 1:1. For the transport, it is important to achieve a constant beam waist throughout the transport distance. In addition to this requirement, we wanted a flexible setup where we can also vary the waist of the beam.

To achieve all aforementioned requirements, we devised a setup that consists of an

acousto-optic deflector (AOD), a telescope consisting of a focus tunable lens pair, another tunable lens with negative focal length, and a final focusing lens. Scanning the beam's frequency with AOD achieves a high aspect ratio of the beam, and the tunable telescope and tunable negative focal lens together allow us to displace the beam while keeping the waist the same at all distances. Moreover, by changing the magnification of the tunable telescope, the beam size can be tuned as desired. For our purpose, we were interested in the waist in range of $50 - 100\ \mu\mathrm{m}$.

thermal lensing The main difficulty that we had with the initial setup was thermal lensing that started around the beam power of $3\ \mathrm{W}$. The beam arrives at the first tunable lens setup has a $1/e^2$ waist of $430\ \mu\mathrm{m}$, and the tunable lens has a clear aperture diameter of $10\ \mathrm{mm}$.

Final setup

To avoid the thermal lensing, we changed our setup to a simpler setup shown in Fig. **??**. The beam is first expanded by a $\times 4$ telescope before reaching the negative focal length tunable focus lens. This reduces the intensity by a factor of 16 compared to our previous setup. Also, this tunable lens has a larger clear aperture diameter of $16\ \mathrm{mm}$. Then, the beam is focused on to the atoms by the last lens which has a focus of $250\ \mathrm{mm}$. This design with a single tunable lens does not allow independent control of the waist and distance. Therefore, the waist changes as a function of distance. We found that for our particular lens choices which produce a beam with a waist of $\sim 50\ \mu\mathrm{m}$, the deviation of the beam waist is smaller $10\ \%$. However, while running experiments, we realized that the thermal stability of the lens leads a long term drift of atom number as the lens heats. For this reason, we keep the lens at *steady-state* temperature by always applying a certain amount of current to the lens.

Future upgrade

Due to a low axial trap frequency of the transport beam $\sim 1\ \mathrm{Hz}$, the transport time is $\sim 10\ \mathrm{s}$. To fix this problem, we plan for a moving lattice setup with which one of the lattice beam's focus moves via a tunable lens along with the lattice during the transport to hold the atoms against gravity. This idea has not been implemented for the work of this thesis, yet has been successfully implemented recently, reducing the cycle time significantly.

5.4 Experimental sequence

To benchmark the performance of our optical lattice setup, we prepare strontium atoms in the vibrational ground states of the deep cavity lattices.

5.4.1 Optical transport

We begin by preparing ^{88}Sr atoms using a robust and rapid magneto-optical trap [39] that operates on the narrow $^1S_0$-$^3P_1$ transition, shown in Fig. 5.3(b). Subsequently, we transport the atoms into the center of the cavity assembly by moving the focus of an optical dipole trap beam at $1070\ \mathrm{nm}$ [140]. The beam propagates along the x axis as shown in Fig. 5.3(c), has a $1/e^2$ beam waist of $50\ \mu\mathrm{m}$, and has a gravity-compensated trap depth of $k_B\times\ 45\ \mu\mathrm{K}$ where k_B is the Boltzmann constant. During the transport, atoms spread axially over a few mm due to the weak axial confinement of the transport beam, and the temperature of the atomic cloud rises to $\sim$7 μK.

5.4.2 Crossed dipole trap

After the transport, we perform narrow-line Doppler cooling in a crossed dipole trap. The crossed dipole trap is created by overlapping the 1070-nm-transport beam and a light sheet at $813.4\ \mathrm{nm}$, as sketched in Fig. 5.3(c). The elliptical light sheet has a $1/e^2$ beam waist of $400\ \mu\mathrm{m}$ ($13\ \mu\mathrm{m}$) along the x (z) axis with a gravity compensated trap depth of $5\ \mu\mathrm{K}$, corresponding to trap frequencies of (20, 5, 500) Hz along the (x, y, z) axes. Subsequently, the transport beam is turned off, and we let the atomic cloud expand in the light sheet.

To adiabatically load the atoms into the cavity lattices sketched in Fig. 5.3(c), we linearly ramp up the intensity of the cavity beams to a lattice depth (frequency) of $60\ \mu\mathrm{K}$ ($116\ \mathrm{kHz}$). Here, the lattice depth refers to a horizontal modulation depth assuming an infinitely extended 1D lattice where the lattice trap frequency ν_t and modulation depth V are related by $\nu_t/\nu_{\mathrm{red}} = 2\sqrt{V/h\nu_{\mathrm{rec}}}$, where $\nu_{\mathrm{rec}} = h/2M\lambda^2$ is the lattice recoil frequency for an atom of mass M, and λ is the lattice wavelength. At this point, the atoms are trapped in the potential created by the sheet and cavity beams. The cavity beams by themselves would produce deep lattices horizontally, but produce a relatively weak dipole trap vertically with a trap frequency of $\sim$50 Hz. Therefore, having the sheet beam that intersects the lattice beams approximately at the minimum of the gravity-adjusted lattice potential provides a tighter confinement along z as shown in the vertical potential in Fig. 5.6(a).

After loading the atoms into the lattices, we cool the atoms to the vibrational ground band using sideband cooling on the $^1S_0$-$^3P_1$ transition [87, 70], where the $689.4\ \mathrm{nm}$ cooling beam propagates horizontally at 45° to the lattice axes, as sketched in Fig. 5.3(c). Then, we ramp down the lattice power after sideband cooling to drop the atoms that are trapped only by the lattices but not by the light sheet, and we ramp up the lattices back. We measure in-trap density profiles with *in-situ* absorption imaging along z [39]. In Fig. 5.3(d), we show a typical absorption image. We use a large field of view and low resolution imaging with $5.40(8)\ \mu\mathrm{m}$ per pixel to image the large atomic distribution and do not resolve the lattice structure. Based on the optical density, we expect an average atom number of $\sim$1 per lattice site at the center of the trap.

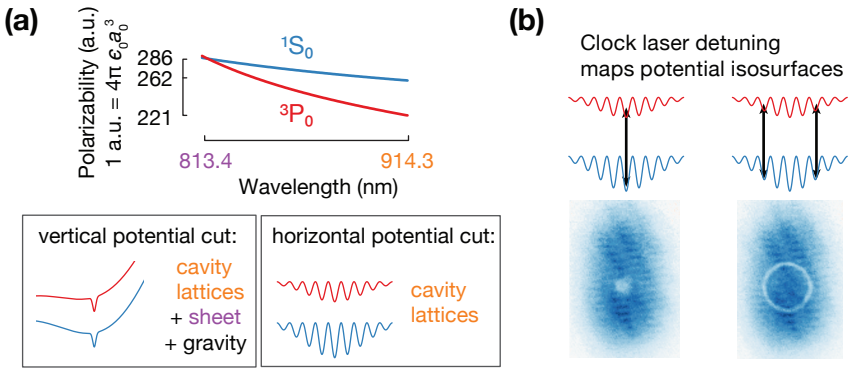

Figure 5.6 Spatially dependent clock spectroscopy in non-magic lattices. (a) Dynamic dipole polarizabilities of g and e states (top). At the light sheet wavelength of $813.4\ \mathrm{nm}$, g and e have the same polarizability (*magic* condition). In contrast, at the cavity lattice wavelength of $914.3\ \mathrm{nm}$, e experiences a polarizability reduced by $15\ \%$ compared to g (*non-magic* condition). For this reason, the light sheet creates identical traps for g and e, while the cavity beams create a slightly stronger potential for g than for e. Vertical and horizontal cuts through the trapping potential created by the light sheet and cavity lattice are sketched below (polarizability difference between g and e is exaggerated for a clear illustration). (b) *In-situ* absorption images after probing the clock transition at different detunings indicated by the black arrows. The differential ac-Stark shifts of the non-magic cavity lattices allow local addressing, leading to ring structures that map the lattice envelope.

5.4.3 ^{88}Sr clock excitation

We take advantage of the ultra-narrow clock transition between $^1\mathrm{S}_0$ (g) and $^3\mathrm{P}_0$ (e) of strontium, shown in Fig. 5.3(b), to perform high resolution spectroscopy. Unlike in the fermionic isotope ^{87}Sr, where the clock transition is weakly electric-dipole-allowed [71] with a linewidth of $1.35(3)\ \mathrm{mHz}$ [54], accessing the transition of the bosonic isotope ^{88}Sr requires an external magnetic field [72]. Despite this, we use ^{88}Sr, because of its high natural abundance and simple electronic structure, which leads to simpler spectroscopic features.

To perform clock spectroscopy, we merge a $698\ \mathrm{nm}$ clock probe beam into the same optical path as the $689.4\ \mathrm{nm}$ sideband cooling beam, as sketched in Fig. 5.3(c). We apply clock laser light for $\sim 600\ \mathrm{ms}$ and a bias magnetic field of $\sim 45\ \mathrm{G}$ parallel to z, unless specified otherwise. The clock probe beam has a $1/e^2$ waist of $\sim 285\ \mu\mathrm{m}$ and a power of $21\ \mathrm{mW}$, where the waist was calibrated as in Ref. [40].

The cavity lattices are created at a wavelength of $914.332\ \mathrm{nm}$. At this wavelength, the differential polarizability of the clock states $\alpha_g - \alpha_e$ is $\simeq 0.15\alpha_g$, as evident from the polarizability plots of g and e shown in Fig. 5.6(a). Here, α_k specifies the polarizability

of a state k. The differential light shift is proportional to the light intensity and the differential polarizability. As a result, the clock transition frequency shifts, and the magnitude of the shift varies as a function of lattice intensity. Lattices in which the two clock states experience different light shifts are called *non-magic*. In contrast, we intentionally make the light sheet operate at the *magic* wavelength of $813.4\ \mathrm{nm}$, such that it does not shift the transition. Therefore, the local clock shift only originates from the cavity beams. The trapping potential for g and e created by the cavity beams and light sheet is illustrated in Fig. 5.6(a), where the illustration includes the effect of gravity. In the vertical potential cut, we see a dimple created by the $813.4\ \mathrm{nm}$ sheet, and its trap depth is identical for both g and e. The horizontal potential cut is dominated by the cavity beams, and e experiences a weaker lattice depth than g. Therefore, we see that only the cavity lattices determine the differential light shift in the horizontal plane.

We model the cavity light intensity as the sum of two orthogonal TEM_{00} Gaussian beams with $1/e^2$ waist w. We have assumed that the waist of both cavity modes is the same because the two cavities are constructed in the same way [41]. We also assume that the waist stays constant over the area of our interest, which is valid because of the long Rayleigh length of the beams, $z_R \sim 80\ \mathrm{cm}$. When the clock laser frequency is tuned close to the maximum differential ac-Stark shift, we excite g atoms in the center as illustrated in Fig. 5.6(b). In contrast, when the laser is red detuned from the maximum, we excite g to e in an equipotential region. This region takes the shape of a ring, reflecting the spatial cross section of the light intensity. Taking such cross sections at different detunings enables us to map out the lattice trap envelope created by the cavity beams.

In our experiments, the clock excitation dynamics are susceptible to two decoherence mechanisms due to elastic e-g collisions and fast inelastic e-e collisions in ^{88}Sr [141]. The elastic collisions reset the coherence between g and e, but the population stays constant. In contrast, inelastic collisions cause atom loss.

To distinguish between the two effects, we use a detection scheme that can image both g and e atoms separately. To image the in-trap density of g atoms, we use absorption imaging on the $^1\mathrm{S}_0$-$^1\mathrm{P}_1$ transition [39] as already explained in the main text. To image e atoms, we remove g atoms by applying light resonant with the $^1\mathrm{S}_0$-$^1\mathrm{P}_1$ transition and repump e back to g by applying $679\ \mathrm{nm}$ and $707\ \mathrm{nm}$ laser light resonant with the $^3\mathrm{P}_0$-$^3\mathrm{S}_1$ and $^3\mathrm{P}_2$-$^3\mathrm{S}_1$ transitions, respectively [141].

Using the above method, we excite atoms in the center of the lattices and take g and e images at different clock excitation durations. From these measurements, we study how the total atom number, *i.e.* $N_g + N_e$, and the excitation fraction, *i.e.* $N_e/(N_g + N_e)$, evolve as a function of the clock excitation duration, where N_s specifies the number of atoms in state s. Since we work with non-magic lattices and an imaging resolution of $5.40(8)\ \mu\mathrm{m}$, the excited state fraction derived from each pixel is averaged over many different clock laser detunings. For this reason, we study the clock excitation dynamics at the center of

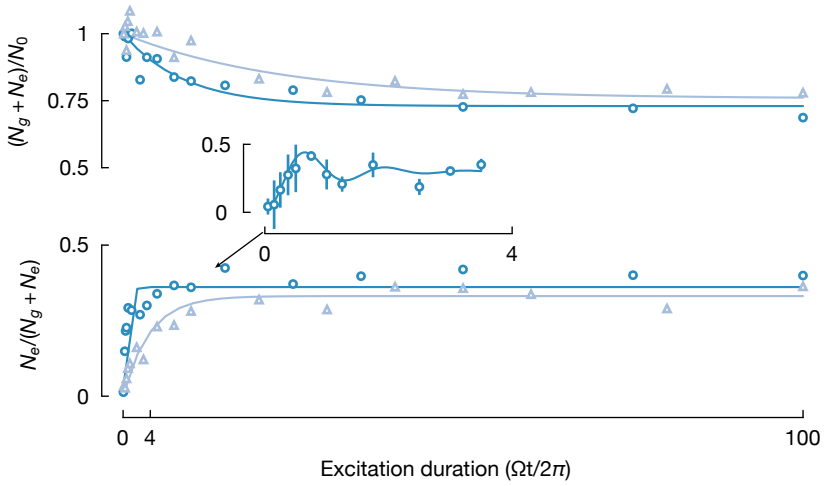

Figure 5.7 Clock excitation dynamics. Total atom number $N_g + N_e$ normalized to the initial total atom number N_0 (top) and excited fraction (bottom) as a function of clock excitation duration. The inset is a zoomed-in portion of the initial excitation fraction dynamics. The measurements are repeated an external magnetic field at $\sim$45 G (triangles) and $\sim$225 G (circles). The solid lines are fit to the exponential rise and decay functions.

the lattices, where the lattice envelope is flattest. The results obtained from averaging the central four pixels are plotted in Fig. 5.7, where we have repeated the measurement at two different magnetic fields, 45 G and 225 G, respectively. Following Ref. [72], the different magnetic field values proportionally scale the Rabi frequency Ω [72]. Therefore, we have rescaled the clock laser duration according to the strength of the magnetic field.

We observe a decay of the total number of atoms as shown in the bottom of Fig. 5.7, which is expected due to the inelastic e-e collisions [141]. At the center of the atomic cloud, we estimate $\sim$1 atom per lattice site on average from the in-situ images. Assuming a Poisson distribution and excluding the empty lattice sites, we expect that $\sim$40 % of the lattice sites are occupied by more than one atom. Therefore, the clock spectroscopy in our setup is susceptible to atom loss. Here, this loss is advantageous in characterizing the potential, because it enhances the signal-to-noise ratio of the ground state depletion images used for the technique. From the data shown in Fig. 5.7, we expect that the 40 % of the atoms lost from the trap and 60 % of the e atoms.

From the dynamics of the excited state fractions shown in Fig. 5.7 (top), we observe an exponential rise to a steady-state value, which resembles strongly dephased Rabi dynamics. At a high magnetic field of 225 G at which we expect $\Omega \sim 2\pi\times500$ Hz, we observe clear Rabi oscillations that quickly dephase as shown in the inset of Fig. 5.7 (top). Beside elastic collisions, there are several other mechanisms that can cause dephasing in our experiments, such as misalignment of the clock probe beam [73], the clock laser linewidth, the clock and lattice laser intensity noise, and the effect of averaging several pixels where

each pixel contains contributions from many clock laser detunings. Among these possibilities, our estimates show that the lattice intensity fluctuations are the most dominant dephasing mechanism. At a differential ac-Stark shift of ~ 400 kHz, a fractional lattice intensity stability of $\sim 10^{-3}$ causes inhomogeneity in δ of 400 Hz, which is already on the order of $2\pi \times \Omega$ at 225 G. Our setup is particularly susceptible to lattice intensity noise because the techniques described in the main text rely on a large differential ac-Stark shift. Such susceptibility to the lattice intensity noise can be removed by creating the lattices at the magic wavelength.

5.5 Characterizing the Lattice Envelope

We use the measured equipotential surfaces to characterize the waist and homogeneity of the potential. At each clock laser detuning δ, we take two absorption images, one without clock excitation, $\mathrm{OD}_{\mathrm{bg}}$, and one with clock excitation, $\mathrm{OD}_{\mathrm{clk}}$. From these two images, we extract a normalized difference image, $(\mathrm{OD}_{\mathrm{bg}}\text{-}\mathrm{OD}_{\mathrm{clk}})/\mathrm{OD}_{\mathrm{bg}}$, and reconstruct the potential map as illustrated in Fig. 5.8(a). This post-processed image reflects the fraction of g atoms that have been *depleted* by the clock excitation. Here, the *depleted atoms* include both those atoms that are still in e at the time of imaging and those that have been lost from the trap after the excitation due to inelastic excited state collisions [141, 142]. We use this post-processed image representing the depleted ground state fraction for further analysis to eliminate possible systematic errors originating from the initial density distribution.

From a series of post-processed images taken at different detunings δ, we determine each pixel's resonant detuning δ_{res}, which is proportional to the lattice envelope averaged over each pixel. Example traces of a pixel's fractional depleted g atoms are shown in Fig. 5.8(b). Each trace is individually fitted to a Lorentzian lineshape to extract δ_{res} for its pixel. The distribution of the reduced χ^2 of all the fits is centered around 0.9, and the statistical errors on δ_{res} from the fits is ~ 100 Hz. The image of δ_{res} maps the shape of the potential and is shown in Fig. 5.8(c). The variation of the potential depth across the whole image is ~ 10 % of the total ac-Stark shift, since we only load atoms into the central lattice region.

To quantify the waist and deviation of the measured δ_{res} from the expected values, we fit the image of δ_{res} to a fit function that models the potential given by the superposition of two orthogonal TEM_{00} cavity modes. The details of the fit function and fit parameters are described in Appendix. We perform a weighted least squares fit and obtain a cavity mode waist of $489(8)$ μm, where the uncertainty arises mostly from the uncertainty in the image system magnification. Although the fit captures the global Gaussian shape well, the residuals reveal that there are additional fringes shown in Fig. 5.8(d). Since the peak-to-peak amplitude of the most dominant fringe (~ 3 kHz) is an order of magnitude larger than the error on the δ_{res} estimates (~ 100 Hz), the fringes are well resolved. The statistical uncertainties show that our method can resolve structures as small as 300 ppm

of the total ac-Stark shift. Due to the additional inhomogeneous fringes, the reduced χ^2 of the lattice envelope fit to the δ_{res} data is $\sim$5, and the histogram of residuals shows an asymmetric distribution shown at the top right of Fig. 5.8(d).

We observe that the inhomogeneous fringes are well aligned with the cavity axes, and that they are more pronounced along the x_2 axis. To determine the frequencies of the fringes, we perform the 2D Fourier transform of the residuals, where the region outside of the circle (Fig. 5.8(d)) was zero-padded. The result shown at the bottom right of Fig. 5.8(d) reveals a factor of three larger fringe amplitude along x_2 compared to x_1, peaking at a fringe wavelength of $\sim 65\ \mu\text{m}$. Despite the different magnitudes, the Fourier transform shows similar spatial frequency components along both axes. This similarity in the frequency components strongly suggests that a common mechanism causes the fringes along both axes.

The presence of these fringes is surprising, since the mode-cleaning effect of the cavities is expected to lead to a very clean potential. The first obvious question is whether the fringes are truly present in the optical potential. We consider three possible scenarios in which the cavity modes can have such fringes: (1) defects or dust particles on the cavity mirrors, (2) leakage of higher order modes from imperfect input coupling [41], and (3) mode mixing due to imperfect cavity mirror surfaces. Based on the fringe frequencies we observe, we conclude that a dust particle attached to a mirror surface would have to be present about $\sim 350\ \mu\text{m}$ away from the mirror's center. However, our estimates show that a dust particle that incoherently scatters light into a solid angle of 2π would have to scatter tens of percent of the circulating power. Such a large scattering should have resulted in a very different cavity finesse compared to our in-situ measurements showing that both cavity finesses agree within $10\ \%$. Moreover, explaining the fringe spacing by a significant contribution of an imperfect coupling and mode mixing requires mixing a TEM_{0m} mode with $m \sim 100$. Therefore, we conclude that all three scenarios are highly unlikely. Other possible explanations include superradiant scattering of atoms in the cavity lattices or diffraction of the imaging beam from the periodic atom distribution. Determining whether the fringes are present in the cavity lattices or whether they originate from the artifacts of the method requires further investigation via other methods such as site-resolved fluorescence imaging. For the remainder of this work, we assume that the fringes are present in the potential and base our estimates on this worst-case assumption.

To our knowledge, we have created the largest far-off resonant 2D optical lattices for trapping ultracold atoms. Our cavity mode waists are more than five times larger than what can be created using the most powerful laser available at this wavelength while preserving the lattice depth, resulting in more than an order of magnitude improvement on the number of available lattice sites. From the measured intensity profile, we estimate an achievable Mott insulator size for the fermionic isotope ^{87}Sr, which has more suitable scattering properties than the bosonic isotope ^{88}Sr. For our estimates, we assume that the inhomogeneous fringes are also present in the cavity lattices. In two dimensions, the

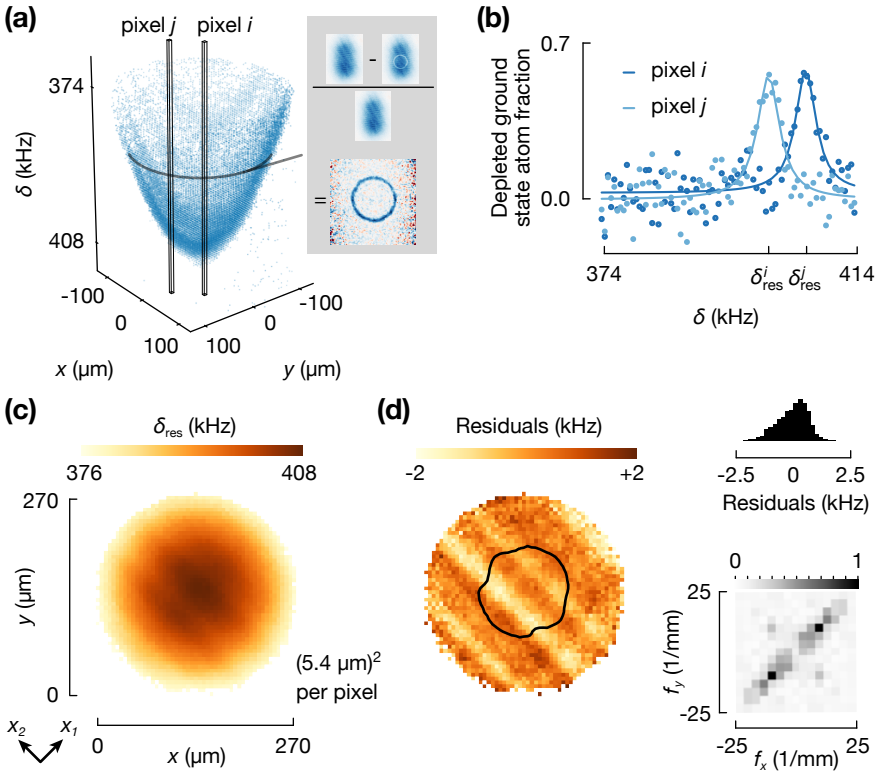

Figure 5.8 Lattice envelope characterization. (a) Envelope of the lattice potential reconstructed by stacking the images of depleted g fractions obtained at different clock laser detunings δ (left). To obtain these images, we take an image with (OD_{clk}) and without (OD_{bg}) clock excitations. For each detuning, we calculate the depleted g fraction (OD_{bg}-OD_{clk})/OD_{bg} (right). (b) For every pixel, we plot the depleted g fraction as a function of detuning δ and extract the peak frequency δ_{res} with a Lorentzian fit (solid lines). (c) Resulting image of δ_{res} for every pixel in panel (a). The cavity axes are labelled as x_1 and x_2. (d) When fitting the potential envelope predicted by ideal TEM_{00} modes to the data in Panel (c), we find fit residuals showing fringe patterns coaligned with the lattice axes. A histogram (peak-normalized spatial Fourier transform) of the residuals is shown in the top (bottom) right. The black contour line on the image of residuals shows the expected Mott-insulator shape, based on the envelope data in Panel (c). The resulting shape is shown as the shaded region in Fig. 5.1(b).

interaction energy U required to form a Mott insulator is approximately $8t$, where t is the tunneling rate [14]. For a fixed scattering length, the lattice depth can be tuned to satisfy the condition mentioned above. At a typical depth of $\sim$10 $h\nu_{\mathrm{rec}}$, a Mott insulator forms within the region where the energy shift due to the lattice envelope is smaller than the interaction energy between two atoms. We find that the peak-to-peak amplitude of the fringes is three times smaller than the interaction energy, which is $\sim$700 Hz for ^{87}Sr. Therefore, we expect a homogeneous Mott insulator extending up to the boundary set by the interaction energy. The fringes cause small distortions of the Mott insulator shape, as shown in Fig. 5.8(d). However, our results show that the size would not significantly differ from the ideal size created with perfectly homogeneous lattices.

From these estimates which are detailed in Section 2.5, we expect that the Mott insulator state will occupy a region with a diameter of $D \simeq 125\ \mu\mathrm{m}$ at a wavelength $\lambda = 914.3\ \mathrm{nm}$. This diameter corresponds to $N \simeq \pi(D/\lambda)^2 \simeq 6 \times 10^4$ lattice sites. The area of the region does not vary much as a function of wavelength λ, although the number of sites changes quadratically due to the change in lattice spacing. For this reason, our cavity assembly offers a solution to create large Mott insulators at any wavelength of interest [40, 94] supported by the cavity mirrors where the laser power is limited.

5.6 Local clock spectroscopy in non-magic lattices

In the previous Section, the discussion focused on driving the most dominant carrier transition between the lowest vibrational states of the g and e lattices. The carrier spectrum discussed in Fig. **??**(b) was modeled with a Lorentzian function. However, the spectrum can become more complex when transitions between higher vibrational states are considered. We now make use of the high spectral resolution of the clock laser to resolve spectral transitions between such higher vibrational states. This new capability enables us to precisely determine the polarizability ratio of the clock states without having to calibrate the lattice intensities. This ratio is an important quantity that determines the magnitude of the differential light shift and can be used to calibrate state-of-the-art atomic structure calculations [40]. Moreover, we find that we can use this method to locally measure temperature with a spatial resolution only limited by the imaging optics.

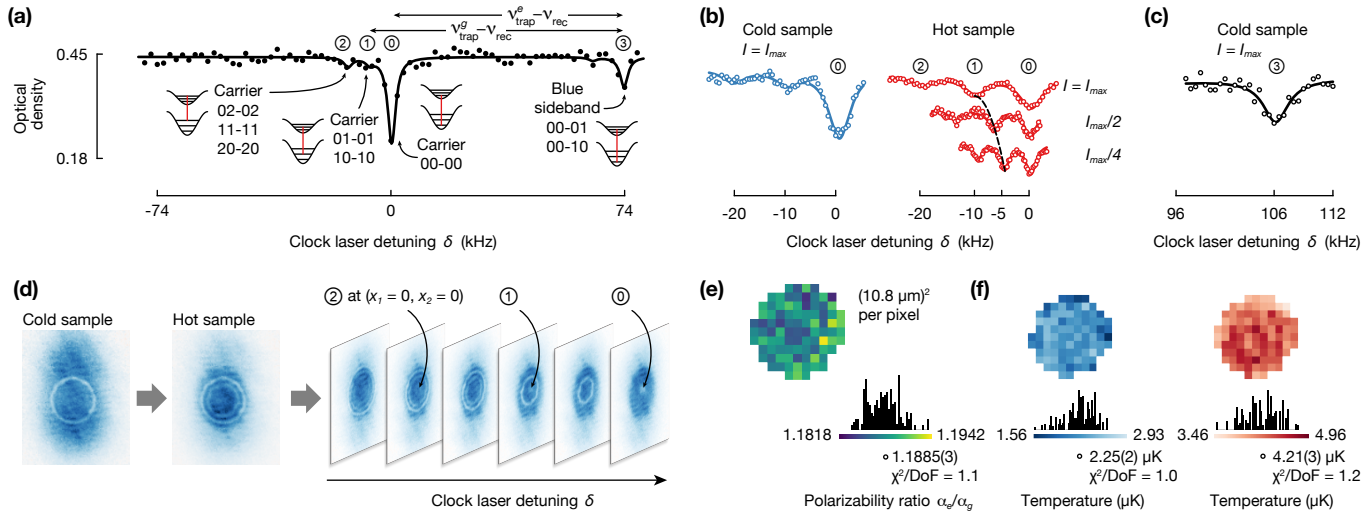

Figure 5.9 Local clock spectroscopy of carrier and sideband transitions in non-magic lattices. (a) A sparse clock sideband spectrum in a 2D non-magic optical lattice. The solid line is a fit to a multi-peak Lorentzian function, in which the peak locations were fixed at the expected detunings. (b) A finer spectrum covering a detuning range of the carrier transitions for the samples with two different temperatures, one colder (left) and the other, hotter (right). To maximize the splitting, we increased ν_t to $\sim$109 kHz from $\sim$77 kHz (at which (a) was taken). For the hotter samples, we vertically stack three spectra taken at different lattice intensities I, at which I_{max} results in $\nu_t \sim 109$ kHz. The dotted line is a guide to the eye for easier visualization of the carrier-splitting-frequency as a function of the lattice intensity. (c) A finer zoomed-in blue-sideband spectrum taken at $\nu_t \sim 109$ kHz (d) Comparison of the absorption images of the cold and hot samples after the clock excitation at a fixed detuning (left) and a series of images of the hot sample as a function detuning. (e) Polarizability ratio and weighted histogram. (f) Temperature maps of cold (left) and hot (right) samples with weighted histograms.

In Section 2.4, we have discussed the absorption spectrum in a 1D magic lattice. The spectrum becomes more complex in a non-magic lattice, where the trap potential is state-dependent. Thus, the trap frequencies of g and e lattices are different, and we use ν_t^s to denote the trap frequency of state s. In this case, the carrier transitions are no longer degenerate, but are split by $\nu_t^e - \nu_t^g$ according to Eqn. (2.24). Moreover, the first blue sideband is detuned by $\nu_t^e - \nu_{\text{rec}}$ from the carrier transition of the lowest vibrational state.

In 2D, the vibrational levels are labelled by two independent vibrational numbers n_1 and n_2, each corresponding to a vibrational band of one of the lattices. Since the two lattices are orthogonal and do not interfere, the energy spectrum is given by $E_{n_1} + E_{n_2}$. For simplicity, we consider the case when both lattices have an equal intensity (or depth), $I = I_1 = I_2$. In this case, the carrier transitions split according to the total vibrational number $n_T = n_1 + n_2$ of the states involved. Therefore, each carrier transition is (n_T+1)-fold degenerate. An example of a coarse scan over the clock excitation spectrum for $\nu_t^e \sim 77$ kHz in our non-magic 2D lattices is shown in Fig. 5.9(a).

We work in a resolved carrier regime that has not been previously explored. The frequency splitting between the two neighboring carrier transitions is $(\nu_t^g - \nu_t^e) \propto \sqrt{I}(\sqrt{\alpha_e} - \sqrt{\alpha_g})$. To maximize the splitting, we increase ν_t^e to ~ 109 kHz, and take a high-resolution spectrum, zooming into the carrier transitions as shown in the left part of Fig. 5.9(b). We observe up to three different carrier transitions, of which the one from the lowest vibrational state is the most blue-detuned. The amplitude of the three peaks becomes more comparable when we intentionally heat the sample by applying a beam resonant with the $^1S_0$-$^3P_1$ transition as shown in the right part of Fig. 5.9(b). As we decrease the lattice depth linearly, we observe that the splitting reduces quadratically as expected. Similar to the carrier transitions, the first blue sideband transitions split as well. However, here we focus on the first blue sideband of the lowest vibrational state, which is shown in Fig. 5.9(c).

The splitting of the carrier transitions is clearly visible in the ground state images as well. As described in the previous Section, we excite atoms in a ring shape, reflecting the equipotential surfaces of the cavity lattice envelope. When we increase the population of the higher vibrational states by heating the sample, we see additional smaller rings appearing in Fig. 5.9(d). Each ring results from driving the carrier transitions from different vibrational states, which are resonant at different locations. Similar to what we have seen in the previous Section, all three rings move inward as the detuning increases due to the spatially dependent ac-Stark shift. The dominant carrier transition, which involves the lowest vibrational states, arrives at the center last because it is the most blue-detuned transition. Moreover, the spacing between two neighboring rings increases as the rings approach the center since the potential becomes flatter.

With the resolved carrier and blue-sideband spectrum, we first extract the polarizability ratio α_g/α_e, which is one of the parameters that determine the magnitude of the

differential ac-Stark shift. Since $\alpha_k \propto \nu_t^k$, the polarizability ratio $\alpha_g/\alpha_e = (\nu_t^g/\nu_t^e)^2$. To measure ν_t^e and ν_t^g, we use an analysis method similar to the one used in the previous Section. For every two-by-two averaged pixel, we determine the frequency difference between the lowest carrier and first blue sideband peaks, which is $\nu_t^e - \nu_{\text{rec}}$. To measure ν_t^g, we heat the sample to better observe the different carrier peaks. For each spectrum of the averaged pixel, we fit a three peak Lorentzian function with the frequency difference between the peaks constrained to be the same. From the fit, we determine the frequency splitting $\Delta\delta$ between the carriers for each averaged pixel, and combine this value with ν_t^e to obtain ν_t^g for every pixel, $\nu_t^g = \nu_t^e + \Delta\delta$. The error bars of the parameter estimates from the fits are rescaled according to the reduced χ^2 of the fits to compensate for the non-Gaussian noise of the absorption images.

In Fig. 5.9(e), we show the polarizability ratio estimated from the pixel-to-pixel ν_g and ν_e maps. The weighted mean of the ratio $\alpha_g/\alpha_e = 1.1885 \pm (3\times10^{-4})_{\text{stat}} \pm (1\times10^{-3})_{\text{sys}}$, which is in good agreement with the theory described in Appendix B. The systematic uncertainty arises from the experimental drifts between the hot and cold data sets that are used to extract ν_e and $\Delta\delta$, respectively. This uncertainty can be greatly reduced by further minimizing the elapsed time between the data sets. The variance of the ratio across the sample can be explained by the variance of each pixel because the reduced χ^2 is 1.14. Therefore, we conclude that we do not observe a systematic variation of the ratio across the sample. Our method provides improved robustness compared to a similar method explored in Ref. [143] because we can make use of the resolved carrier spectrum combined with spectral imaging.

Finally, we extract the local temperatures of the sample using the carrier spectrum. In the temperature regime that we are considering, the vibrational populations are Boltzmann-distributed. In this case, the temperature T can be estimated by measuring the relative population p_0/p_1 of the first two non-degenerate levels and the energy spacing between them, using $k_B T = h(\nu_t^g - \nu_{\text{rec}})/\ln(2p_0/p_1)$. We estimate $\nu_t^g - \nu_{\text{rec}}$ for each pixel using the same method as described above. Next, we use a hotter sample and determine the peak locations and amplitudes by fitting a three-peak Lorentzian function with equal frequency difference between the peaks to each averaged pixel, and we compare the amplitudes of the two most blue-detuned carrier peaks to estimate p_1/p_0. For the colder sample, we repeat the same procedure but keep the peak locations fixed to those determined from the hotter sample.

The extracted temperature maps and weighted histograms are shown in Fig. **??**(e). We clearly observe a temperature difference between the cold and hot samples at $2.25(2)$ μK and $4.21(3)$ μK, respectively. The temperature variation across the samples are within the temperature uncertainty of each pixel because the reduced χ^2 is 1.01 and 1.2 for cold and hot samples, respectively. The temperatures of the cold sample correspond to $\sim$80% vibrational ground state fraction.

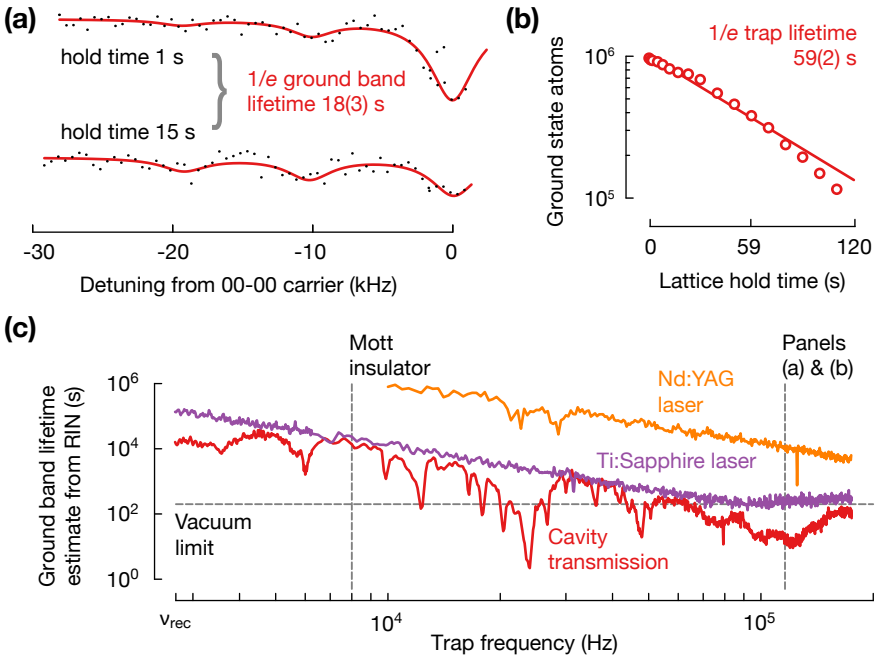

Figure 5.10 Lifetime in the cavity lattices. (a) Resolved carrier spectra in the cavity lattices at a trap depth (frequency) of 457 $E_{\mathrm{rec}}(116\ \mathrm{kHz})$. The spectrum on top (bottom) was taken after holding atoms for $1\ \mathrm{s}$ $(15\ \mathrm{s})$ in the lattices. We extract a $1/e$ lattice ground band lifetime of $\sim 18(3)\ \mathrm{s}$. (b) Number of g atoms as a function of lattice hold time. We extract an overall $1/e$ trap lifetime of $59(2)\ \mathrm{s}$. (c) Estimated ground band lifetime as a function of lattice depth. The estimation was performed by rescaling the relative intensity noise (RIN) of a Ti:Sapphire laser transmitted through cavity 2. For reference, we show the same estimates obtained from the RIN of the cavity input light and the RIN of a highly intensity-stable Nd:YAG laser.

Our local thermometry assumes that the induced atom losses during the clock excitation do not influence the temperature estimates. This assumption is corroborated by repeating the temperature measurements with shorter clock excitation durations and negligible loss, where we did not observe temperature differences. The thermometry technique based on the carrier spectrum has been proven to be more precise than methods based on time-of-flight or sideband spectrum due to its high signal-to-noise ratio [143, 144]. We have improved the technique's robustness by resolving the carriers and extended it to probe local temperatures. When combined with higher numerical aperture imaging, this technique will open opportunities to spectroscopically measure motional band populations with single-site resolution.

5.7 Lifetime

In optical traps, heating induces excitation to higher motional bands, leading to motional state decoherence and subsequent atom loss. To characterize the heating sources in our setup, we measure the lifetimes of the ground band population and the overall lifetime of atoms trapped in the cavity lattices.

We characterize the ground band lifetime using the resolved carrier spectrum technique presented in the previous section. This technique offers a new way to probe the motional ground band populations in the high-lattice-depth regime with high signal-to-noise. In Fig. 5.10(a), we take two carrier spectra after holding the atoms in the lattices at a modulation depth (frequency) of 457 E_{rec} ($116\ \mathrm{kHz}$) for $1\ \mathrm{s}$ and for $15\ \mathrm{s}$. By comparing the populations in the ground band at these times and assuming an exponential heating rate, we extract a ground band lifetime of $18(3)\ \mathrm{s}$, which is comparable to state-of-the-art free space lattice experiments [53] at similar depths in units of the recoil energy.

In addition to the ground band lifetime, we also measure the overall trap lifetime at the same lattice modulation depth. The overall trap lifetime serves as a good benchmark to compare with other setups where the ground band lifetime is not accessible. In Fig. 5.10(b), we show the number of g atoms trapped in the cavity lattices and light sheet as a function of the trap hold time, and we extract a trap $1/e$ lifetime of $59(2)\ \mathrm{s}$.

The heating mechanisms in optical traps include collisions with background gas, incoherent scattering of trap light, and laser-noise-induced heating [53]. Based on the longest trap lifetime we have measured, we project a vacuum limited lifetime $>180\ \mathrm{s}$. The expected lifetime due to incoherent light scattering is also more than two orders of magnitude longer than the observed ground-band lifetime, leaving laser noise as the main source of heating. Moreover, we observe that the lifetime changes depending on the parameters of the laser's intensity and frequency stabilization control loops.

Laser-noise-induced heating arises due to laser beam intensity and pointing fluctuations. In deep optical lattices, where each lattice site can be approximated as a harmonic trap, the laser intensity (pointing) noise power spectral density at $2\nu_t$ (ν_t) causes parametric heating [126] that results in transitions between lattice bands that are two (one) motional quanta apart. In traps enhanced by optical cavities, we expect the intensity fluctuations to dominate for two reasons. First, heating from pointing fluctuations is strongly suppressed due to the resonator's mechanical stability [145]. Second, locking a laser to a cavity resonance converts laser frequency noise into amplitude noise, increasing the latter beyond that in free-space optical lattices [97]. Thus, we focus on the relative intensity noise (RIN) of the laser transmitted by the cavities. Combining the RIN and ground band lifetime measurements, we estimate expected lifetimes for different lattice depths as shown in Fig. 5.10(c). Here, we use the parametric heating rate $\propto \nu_t^2 S(2\nu_t)$ to scale the lifetimes to the measurement shown in Fig 5.10(a), based on the model in Ref. [53].

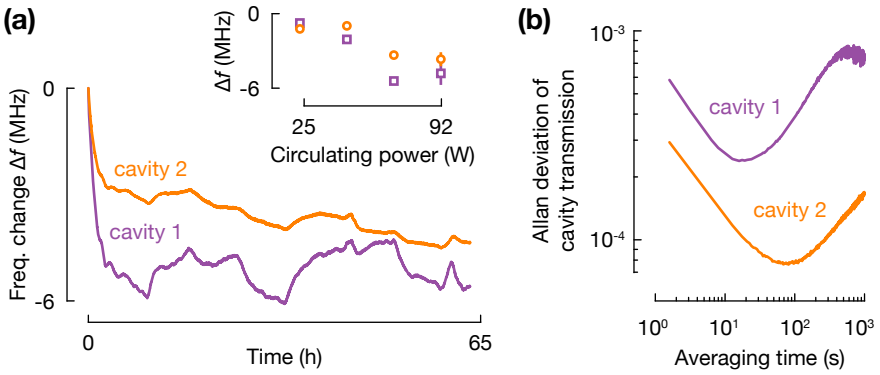

Figure 5.11 Stability of the cavity lattices (a) Cavity resonance frequency change Δf as a function of time for both cavities. At $t = 0$, we couple the laser beams into the cavities, which create a circulating power of ~ 92 W per cavity. We see a rapid initial decrease of 6 MHz, which corresponds to an expansion of the cavity length by 1 nm. Then, Δf settles and fluctuates with a peak-to-peak amplitude of ~ 2 MHz. Inset: Δf as a function of circulating power for caivty 1 (squares) and 2 (circles). Here, Δf is extracted by fitting the trace of the first hour to an exponential function. (b) Fractional intensity variation of the cavity transmission plotted as a function of time.

However, based on the rescaled RIN of the transmission, we conclude that the ground band lifetime will be vacuum-limited in most regions, even at wavelengths where very low noise non-planar-ring oscillator [146] lasers are not available.

5.8 Long-term Stability

Finally, we characterize the long-term frequency and intensity stability of the lattice beams. In our setup, the lattice laser is stabilized to a resonant frequency of the cavity, which slowly changes as the cavity shrinks or expands. Since we do not actively stabilize the cavity length, any length change directly influences the laser frequency. Although we actively stabilize the input beam power before coupling it into the cavity, we do not additionally stabilize the power of the transmitted light. Therefore, the beam power inside the cavity is susceptible to mechanical drifts of the incoupling optical components and the performance of the input intensity servo. In this Section, we quantify the frequency and intensity drifts of our setup and discuss the consequences for optical lattice clocks and quantum simulators using our cavity lattices.

To estimate the laser frequency drift due to the cavity length change, we continuously measure two parameters: (i) the laser frequency by beating it with a femtosecond optical frequency comb and (ii) the frequency of the double-pass AOM used to stabilize the laser to the cavity resonance frequency. By subtracting the two numbers, we obtain the cavity's resonance frequency drift independently of the laser frequency drift. In Fig. 5.11(a), we plot the change of the resonance frequencies for both cavities as a function of time,

starting with the moment we couple light into the cavities. We use a circulating power of $\sim$92 W in each cavity, matching the conditions of the previous measurements. Within the first hour, we observe a rapid decrease in the resonance frequency of $\sim$6 MHz. Subsequently, the resonance frequencies settle but fluctuate with a peak-to-peak amplitude of $\sim$2 MHz.

The decrease by 6 MHz corresponds to a cavity expansion of 1 nm compared to the nominal cavity length of 50 mm. When repeating this measurement at different power levels, we see that the expansion reduces proportionally (see inset). We conclude that the cavity mirrors scatter and absorb part of the circulating light due to the cavity mirror losses, which are $\sim$100 ppm based on our finesse and transmission measurements. These losses deposit heat on the cavity which therefore expands. We attribute the fluctuations on the long time scales to slow environmental temperature changes, which could be further reduced by stabilizing the temperature of the vacuum chamber.

We use the measured resonance stability to estimate a lower bound of the accuracy of an optical lattice clock based on our cavities. Compared to cavities that are tunable in length [145, 93, 147, 148, 138], we will have to overcome the obstacle of constructing a fully monolithic cavity with resonances as close to the magic wavelength as possible. This problem could be solved by adapting our optical contacting methods [82] to tune the resonance frequency with an accuracy of 10 MHz. The cavity resonance frequency can be further fine-tuned by placing it in a temperature-controlled enclosure that is also required to create a well-defined blackbody-radiation environment [56]. To estimate the clock inaccuracy due to detuning from the magic wavelength condition, we assume a lattice depth of 100 E_{rec} [149], which will lead to a cavity frequency variation of $\sim$1.3 MHz caused by coupling light into the cavity. With these assumptions, we obtain a clock frequency variation of 2 mHz [150], corresponding to a fractional clock accuracy of $\approx 5 \times 10^{-18}$. We believe that the largest contribution to the cavity frequency variation is the mirror loss, which can be reduced by more than an order of magnitude when using mirrors with $<$10 ppm loss. This reduction would improve the frequency stability by an order of magnitude better, assuming that reducing the mirror loss would proportionally reduce the cavity frequency variation. The necessary temperature control to minimize the black body shift uncertainty reduces the frequency fluctuations caused by environmental changes to the same level. With these improvements, we project a possible clock accuracy below 10^{-18}, which would let state-of-the-art 2D or 3D optical lattice clocks make use of the scaling advantage provided by our cavity lattices.

Finally, we characterize the long-term stability of the cavity lattice depth by measuring the cavity transmission. The Allan deviation of the transmitted power as a function of the averaging time is shown in Fig. 5.11(b). We observe a fractional stability below 10^{-3} for typical $\sim$20 s cycle times of quantum gas microscope experiments. Furthermore, the transmission of cavity 2 is more stable than the one of cavity 1, which is consistent with the lower input power sensitivity observed in Fig. 5.11(a). By measuring the transmission

and implementing a slow feedback loop on the cavity input powers, we could preserve the stability over many experimental runs which would result in long-term-stable quantum simulation parameters. The fractional stability of the tunneling rate t and the interaction energy U roughly scale as $(3/4)(\sigma_V/V)$, where σ_V/V is the fractional uncertainty of the lattice depth V. Therefore, we expect that it is feasible to achieve a long-term stability of 10^{-3} for t and U.

5.9 Conclusion

We have presented a new cavity-based experimental platform for scaling quantum simulators, quantum computers, and clocks based on neutral atoms trapped in optical lattices. Our lattices increase the number of available lattice sites by more than an order of magnitude compared to state-of-the-art free-space lattices [53]. Currently, most far-off-resonant optical lattices are created using high-power Nd:YAG lasers. Here, our solution opens new possibilities to create large and deep lattices at any desired wavelength supported by the cavity mirror coatings.

As a demonstration, we loaded strontium atoms into two-dimensional optical lattices generated at $914.332\ \mathrm{nm}$, which is well-adapted for narrow-line laser cooling of strontium atoms. The lattice laser beams have waists of $489(8)\ \mu\mathrm{m}$ and operate at a circulating power of $92\ \mathrm{W}$. This circulating power is more than an order of magnitude larger than commercially available laser power at this wavelength. Despite the large beam waist, atoms are trapped in lattices as deep as 457 E_{rec}, corresponding to trap frequencies of $116\ \mathrm{kHz}$. In these non-magic optical lattices, we perform high-resolution clock spectroscopy. Extending the work of Refs. [151, 152], we show a highly sensitive method to reconstruct the lattice intensity envelope from the local clock shift. The statistical uncertainty of our reconstruction method shows that intensity deviations as small as $300\ \mathrm{ppm}$ of the peak intensity can be resolved. From the reconstructed intensity map, we estimate the size and shape of a future Mott insulator state and conclude that the state will consist of 6×10^4 atoms.

This atom number is more than an order of magnitude larger than in state-of-art 2D optical lattices generated from free space laser beams [53]. The combination of high resolution laser spectroscopy and deep non-magic lattices allows us to resolve different motional carrier transitions of the lattices for the first time.

We use this capability to locally measure the sample temperature with high spatial resolution. The resolved carrier spectrum also provides a method to directly measure the ground-band lifetime.

We observe ground-band and lattice lifetimes of $18(3)\ \mathrm{s}$ and $59(2)\ \mathrm{s}$ respectively, and a long-term lattice frequency (depth) stability on the MHz (0.1%) level. Our results demonstrate that there are no disadvantages of cavity-based far-off resonant optical lat-

tices compared to free space, while allowing the creation of deep and large optical lattices at wavelengths where the available laser power is limited.

These cavity lattices open up many new possibilities for analog and digital quantum simulation, including controlled collisional phase gates [21, 27, 28], quantum simulations of light-matter interfaces [17, 32, 33, 31] and quantum chemistry [34]. Moreover, the strong reduction in harmonic confinement will reduce the finite size effects for any optical lattice quantum simulator and will reduce the experimental time required for measuring quantum many-body correlations.

The cavity lattices can also be used to improve the precision of lattice-based atom interferometers and optical lattice clocks by providing more identical particles to reduce the quantum projection noise. Our compact and stable cavity design will enable near-future applications of optical atomic clocks that require hands-off operation outside of laboratories such as in satellites and airplanes [153–156]. Finally, neutral atom arrays in optical tweezers interacting via Rydberg states have become a promising candidate for quantum computing [157, 158], but current array sizes have been limited to $\sim$400 sites partly due to the high power requirement associated with creating larger arrays [159]. Our optical cavity lattice can be used to scale neutral-atom quantum computers to tens of thousands of lattice sites.

Chapter 6

Conclusion and Outlook

In this thesis, we started by describing the basics of light matter interactions, with a focus on the unique properties of strontium as an alkaline earth metal atom, and then described how these properties can be used to create new tools for quantum simulation. These tools include an improved method for fast and robust laser cooling, the creation of state-dependent lattices for the strontium clock states, and the development of a novel cavity-based architecture for scaling optical lattices. In the main chapters of this thesis, we reported on the construction of a strontium quantum simulator that combines all of these tools. With these advancements, our strontium quantum simulator is now uniquely equipped to implement several new proposals for quantum simulation, including the simulation of nanophotonics and quantum chemistry, as well as collisional phase gates in quantum computation. To finish this thesis, we now describe the future of our quantum simulator.

The next piece to complete our quantum simulator a quantum gas microscope to implement single-site imaging and manipulation. A necessary step for quantum gas microscopy is to prepare atoms in a single layer of a 3D optical lattice. If this process, known as slicing, is not performed, then the finite focal depth of the quantum gas microscope, which is larger than the spacing between the 2D layers, would result in a blurred image. We plan to implement slicing using the metastable and magnetically sensitive $^3P_2$ state. Starting with a 1D optical lattice in the z-direction, we will apply a magnetic field gradient in the same direction, such that driving the $^1S_0$-$^3P_2$ transition will excite the atoms only in within a certain range of z-coordinate. The excited $^3P_2$ states will then be lost from the trap due to inelastic collisions. In this way, we can excite all but a single layer of atoms, and then turn on the lattice in the x-y plane to prepare a 2D lattice. This procedure has already been successfully used to achieve single-site imaging of ytterbium [98], and it is expected to work similarly well for strontium.

At the time of writing this thesis, all the necessary components such as magnetic coil systems and $^3P_2$ laser systems have been incorporated into our setup, and the spectroscopy of the $^1S_0$-$^3P_2$ transition in both bosonic and fermionic components is currently being performed. Apart from our goals, the spectroscopy of these states is interesting on its own, as it is relatively poorly understood despite the use of these states in proposed schemes for quantum computation. The other key component of the quantum gas microscope, the high resolution objective, has also been characterized [109], and the mount

design has been finished. Upon completing the preparation and final installation of the microscope, our setup will be the first demonstration of the ability to image and address individual strontium atoms, which will have a significant impact on future realizations of atomic clocks, quantum computation, and quantum simulation schemes.

After adding the quantum gas microscope to the set of tools described in this thesis, the experiment can take on many different directions. An especially suitable one is simulating nanophotonic physics by creating an analog of a single emitter coupled to a bath, as described in Chapter 2. A near-term goal in this direction is studying bound state physics. When coupling the emitter into the band gap (where the density of states is zero), the existence of a bound state [160] is expected. In such a state, the bath particle remains at the emitter position, with its probability density decreasing exponentially away from the position of the emitter. Bound states in 1D have recently been realized both in a photonic crystals [161] and in a cold atom analog using rubidium [19]. However, our simulator will enable direct spatially-resolved imaging of the bound state, pushing the limits of what can be observed in experiments with bound states. Moreover, bound states in 2D can be realized for the first time, paving the way to realize strong and controllable long-range dispersive atom-atom interactions in 2D [162]. These bound states will considerably enrich the quantum simulation toolbox, and will enable novel scenarios in quantum many-body simulation, such as the simulation of quantum chemistry [34]. In the long-term, unprecedentedly long-lived subradiant states may be engineered by tailoring the emission direction and dynamics of multiple emitters in 1D and 2D. Such extremely long-lived subradiant states have many potential applications in both metrology and quantum computation [163] because of the extremely low decoherence rates that they enable.

Appendix A

Cavity lattice potential - fit function derivation

In this Section, we derive the fit function used in Chapter 5, describing the spatially dependent detuning that is resonant with the clock transition.

The energy shift of each clock state can be decomposed into two parts: a shift induced by the ac-Stark effect and the zero-point vibrational energy in each lattice site. The former is given by $-\alpha_k I(x_1, x_2)/2\epsilon_0 c$, where ϵ_0 is the vacuum permittivity, $I(x_1, x_2)$ is the total lattice intensity from the both lattices, and k labels the state e or g. In orthogonal 2D optical lattices where the two lattices have an identical beam waist w, we can write the lattice envelope as $I(x_1, x_2) = I_0[e^{-2(x_1-x_1^0)^2/w^2} + (1+\varepsilon)e^{-2(x_2-x_2^0)^2/w^2}]$, where ε specifies the intensity balance between the two lattices, I_0 is the peak intensity, and x_j^0 specifies the position of the lattice intensity maximum. The second cause of the energy shift is the zero-point vibrational energy of each state. Assuming that the atoms occupy the vibrational ground state, the zero-point energy experienced by each state is given by $h\nu_t^s(x_j)/2$ per lattice axis, where $\nu_t^s(x_j)$ specifies the on-site lattice trap frequency that state s experiences along the lattice axis x_j. The lattice trap frequency also depends on polarizability and light intensity. Following the above definitions, $\nu_t^s(x_1) = 2\sqrt{\nu_{\text{rec}}\alpha_k I(x_1)/(2c\epsilon_0 h)}$ and $\nu_t^s(x_2) = 2\sqrt{\nu_{\text{rec}}(1+\varepsilon)\alpha_k I(x_2)/(2c\epsilon_0 h)}$.

The resonant condition occurs when the detuning with respect to the free space resonance matches the additional shifts,

$$\begin{aligned}\delta_{\text{res}} = &\frac{1}{2\epsilon_0 ch}(\alpha_g - \alpha_e)I(x_1, x_2) \\ &+ \sqrt{\frac{\nu_{\text{rec}} I(x_1)}{2c\epsilon_0 h}}(\sqrt{\alpha_e} - \sqrt{\alpha_g}) \\ &+ \sqrt{\frac{\nu_{\text{rec}}(1+\varepsilon) I(x_2)}{2c\epsilon_0 h}}(\sqrt{\alpha_e} - \sqrt{\alpha_g}).\end{aligned} \tag{A.1}$$

In our experiments, we spectroscopically measure the peak trap frequency of g or e to calibrate the peak lattice intensity, I_0, and the polarizability ratio, α_g/α_e. We rewrite the above expression with respect to these quantities, where the peak trap frequency is

$\nu_t = 2\sqrt{\nu_{\text{rec}}\alpha I_0/(2c\epsilon_0 h)}$. Then, we can rewrite δ_{res} as

$$\begin{aligned}\delta_{\text{res}} = \frac{1}{\nu_{\text{rec}}}\left(\frac{\nu_t^e}{2}\right)^2\left(\frac{\alpha_g}{\alpha_e}-1\right)\Big[&e^{-2(x_1-x_1^0)^2/w^2} \\ &+ (1+\varepsilon)e^{-2(x_2-x_2^0)^2/w^2}\Big] \\ &+ \frac{\nu_t^e(e^{-(x_1-x_1^0)^2/w^2})}{2}\left(1-\sqrt{\frac{\alpha_g}{\alpha_e}}\right) \\ &+ \frac{\nu_t^e\sqrt{1+\varepsilon}(e^{-(x_2-x_2^0)^2/w^2})}{2}\left(1-\sqrt{\frac{\alpha_g}{\alpha_e}}\right),\end{aligned} \tag{A.2}$$

where we have chosen the e trap frequency ν_t^e rather than g, for convenience.

We fit the data described in Section 5.5 to the fit function shown in Eqn. (A.2) with an additional fit parameter, which is a frequency offset f_0. The fitted parameters are x_1^0, x_2^0, f_0, w, and ε. We obtain the cavity mode waist of $489(8)\ \mu\text{m}$ with a reduced χ^2 of $\sim$5, as discussed in the main text.

Appendix B

Clock state polarizabilities

The polarizability of an electronic state is determined by contributions from the core and valence electrons. The core part of the polarizability can be calculated in the single-electron approximation, including random-phase approximation corrections [122]. The valence part of the atomic state i is given by the sum of contributions over all electric-dipole coupled states k. This part can be decomposed further into scalar, vector, and tensor parts. For the clock states of ^{88}Sr where both states have $J = 0$, only the scalar part contributes [40], and the polarizability can be calculated according to [164]

$$\alpha_k = \frac{2}{3\hbar} \sum_l \frac{|\langle l|D|k\rangle|^2 \omega_{kl}}{\omega_{kl}^2 - \omega^2}. \tag{B.1}$$

Here $\langle l|D|k\rangle$ is the reduced dipole matrix element between the clock state k and state l. We use ω_{kl} to denote the corresponding transition frequency. The valence part depends as well on the frequency ω of the light field interacting with the atom.

We calculate the polarizability of the states $5s5p\ ^1\mathrm{S}_0$ and $5s^2\ ^3\mathrm{P}_0$ at $914.332\ \mathrm{nm}$ in Tab. B.1. From the total polarizabilities, we extract $\alpha_g/\alpha_e = 1.18 \pm 0.01$, where g (e) refers to $^1\mathrm{S}_0$ ($^3\mathrm{P}_0$).

l	ΔE	$\langle l\|D\|k\rangle$	α_k
		$k = 5s^2\ {}^1\mathrm{S}_0$	
$5s5p\,{}^3\mathrm{P}_1$	14504	0.1510	0.53
$5s5p\,{}^1\mathrm{P}_1$	21698	5.248	248.98
$5s6p\,{}^3\mathrm{P}_1$	33868	0.034	0.01
$5s6p\,{}^1\mathrm{P}_1$	34098	0.282	0.38
Other			5.8
Core			5.3
Total			261.0 ± 1.2
		$k = 5s5p\ {}^3\mathrm{P}_0$	
$5s4d\,{}^3\mathrm{D}_1$	3842	2.671	-38.25
$5s6s\,{}^3\mathrm{S}_1$	14721	1.968	85.92
$5s5d\,{}^3\mathrm{D}_1$	20689	2.450	58.91
$5p^2\,{}^3\mathrm{P}_1$	21083	2.605	64.44
$5s7s\,{}^3\mathrm{S}_1$	23107	0.515	2.16
Other			42.07
Core			5.55
Total			220.8 ± 2.3

Table B.1 Contributions to scalar polarizability α_k of the states $5s^2\ {}^1\mathrm{S}_0$ and $5s5p\,{}^3\mathrm{P}_0$ at $914.332\ \mathrm{nm}$. The transition energies ΔE are listed in cm^{-1} and the reduced electric-dipole matrix elements $\langle l|D|k\rangle$ are shown in atomic units. The energies and matrix elements are taken from Refs. [165] and [121, 166], respectively. Here, *Other* refers to contribution from states which are not listed explicitly and *Core* to the core polarizability. Uncertainties for individual contributions are the result from propagating uncertainties in the matrix elements and are not shown here.

Acknowledgements

My Ph.D. work, of course, would not have been possible with the support and guidance from *many* people.

First and foremost, I would like to thank Dr. Sebastian Blatt for his continuous guidance throughout my Ph.D. He has taught me from the very basics of laboratory work to building a *very* complicated machine, where one has to keep track of every little component correctly. Outside the laboratory, he taught me how to simplify my problems and find the optimal solutions. His vast knowledge and dedication to physics have always inspired me to push my limits. I admire his leadership deeply because he takes full responsibility for anyone he works with and treats everyone equally and fairly. On top of all these, he never forgets to bring a sense of humor to the table.

I would also like to thank Prof. Immanuel Bloch for guiding our group on a regular basis in the group, even with his very busy schedule. When we were too focused on details, he constantly reminded us of the bigger goals so that we stayed on track. Moreover, his continuous efforts to foster a vibrant and successful research group have always been inspiring. It was a great blast to have the opportunity to work in his group, where everyone is very focused, motivated, and is willing to help and discuss.

I am also very grateful that I shared two years of lab time with Neven Šantić. I learned a great deal of physics from him as together we ran our experiment day and night. He transferred his expert knowledge in feedback loops and laser frequency stabilization to me. More importantly, he introduced me to the frequency comb, untouched expensive equipment that I had never thought of using until Neven came along. He never got tired of answering all my physics questions and taught me how to get the experiments running on the "cheap" by assembling necessary parts with whatever was available in the lab instead of just waiting for the commercial replacements. His initiative and motivation to produce the best work and his great virtue of helping others have inspired me and all of us in the laboratory.

I would like to thank Stepan Snigirev and André Heinz, the first members with whom I built the experiment. Stepan is *the* software wizard. He would teach me tricks to simplify my code and introduced me to Javascript for the first time. Moreover, he has an amazing ability to make any figures *just right*; I thank him for giving me basic guidance on how to get started on making figures. He is also filled with positive energy, which made me truly enjoy working with him. When my focus and enthusiasm were flagging, his positive attitude and calm approach remotivated me. André is the colleague with whom I shared

the most lab time. We shared many ups and downs while building the experiments together. Although we have very different characters, we stayed as a team together, and I thank him for always putting the experiment first and making it easy for us to leave our egos aside. Moreover, I thank him for his hard work in designing and manufacturing the cavity, and I have relied upon his many other areas of expertise during my PhD. Lastly, I would like to thank him for all his heavy lifting workouts so that he could lift equipment that I just *couldn't* lift.

Jan Trautmann joined the team about three years after we had started the experiment. He quickly unloaded tasks from our hands, getting a new Ti:sapphire laser ready, preparing coil systems, performing detailed analysis as soon as I took data, and taking care of all the tasks related to upgrading the system. I am very grateful for his self-initiative, which made the experiments progress at a much faster pace. Especially, I thank him greatly for his help during my thesis time. He took care of all the nitty-gritty details from the experiments and mentored undergraduates and interns in our lab so that I could focus solely on my thesis writing. Moreover, I thank him for being the *bad guy* in the lab when it came down to voicing any complaints to companies or any other people on behalf of our lab (which I had a very hard time doing!). I should also thank his girlfriend, Sarah, for her delicious pastries! Her Christmas cookies were something I looked forward to at the end of every year.

The lab work was even more enjoyable when Valentin Klüsener and Dimitry Yankelev joined the team. I thank Valentin for always showing his enthusiasm for physics, discussing his new ideas about the experiments and research articles he read. His fascination kept my motivation going during the last stretch of my PhD years when I was exhausted. Moreover, I thank him for maintaining the frequency comb and quickly getting it going when I needed it, and I also thank him for the new clock laser systems that I have enjoyed using during my last project. I would also like to express my appreciation to Dimitry, who has always been willing to help and discuss physics. In particular, I thank him for his quick and insightful comments about my thesis and paper manuscripts.

I also thank Dimitris Tsevas for always being ready to help and being a very supportive lab and office mate. He was always available to discuss any problems I was having and showed me some coding tricks. During my thesis writing, he also took care of almost all the visitors who came to our office asking for any help! Moreover, I admire his work ethic, and he genuinely cares that his work is helpful for the future development of the field in general. These characteristics made me reflect on my behavior when my motivation and work ethic flagged. Not only that, I thank him for all the fun breaks we had together, making me feel better when I ate too many ice-creams and sweets, taking care of all the stuff I have left behind in my office, and printing and delivering this thesis to the university!

I would also like to mention my best buddies during my early years in the strontium

lab, Nejc JanŠa and Rodrigo González Escudero. They taught me from the basics of working in an optics laboratory to working with both mechanical and electronic software programs. Moreover, they became my truly long-term friends, and I thank both of them for making a trip to Munich to visit me, which gave me highly needed breaks during my PhD. Moreover, I especially thank Rodrigo for always being available online to listen to me rehearse presentations, voice to my beefs, and engage in discussions related to my PhD work.

I would also like to thank many Master's and intern students who worked in our lab: Stephan Wissenberg, Fabian Finger, Rudi Haindl, Etienne Staub, Florian Wallner, Eva Casotti, and Matteo Kruljac. Each of them built indispensable lab equipment that was important for this project. In particular, I thank Rudi for the excellent ultra-stable cavity he left us, which gave my everyday task of optimizing the detuning of the cooling laser much easier.

A special thanks go to the group's mechanical and electrical technicians Anton Mayer and Karsten Förster, respectively, for their invaluable work. They both have limitless knowledge and experience in their areas of expertise, which became the backbone of our experiments. Not only did they manufacture what I needed for the experiments, but they also took their time to teach me the underlying principles so that I could choose the best tools for my projects. What is also very incredible is that they rarely make mistakes! They are both prudent in their work and made the products that I could trust 100%. Also, I also thank them for genuinely caring for my well-being and reminding me to take breaks. I cherish the supportive relationships I have made with them, which made me feel at home even at work.

I also appreciate the support from the Natural Sciences and Engineering Research Council of Canada (NSERC) for funding my PhD, and thank my previous advisor, Raymond Laflamme, for always greeting my updates from Munich and providing reference letters promptly.

Sincere thanks are also due to my other colleagues in the Bloch group for always being willing to lend their equipment, debug problems and discuss physics together. In particular, I became great friends with Jaya Vijayan, Lorenzo Festa, Toni Rubio Abadal, and Simon Hollerith. Jaya helped me through my preparation for the Ph.D. interview presentation: waking me up early in the morning, helping me make figures, and listening to my rehearsals. I was extremely nervous and intimidated about this presentation, and without Jaya's support, I would never have dared to give the talk and would have blown away this wonderful opportunity to be able to do a PhD here. I thank Lorenzo for listening to all my beefs during my thesis writing time, even when he was also in a stressful situation, and for being a great flatmate. Toni has always been a person who is full of stories to tell and much enthusiasm about physics. I learned a great deal of physics while discussing it with him, and I always enjoyed having him around because of

his positive energy and enthusiasm. I also thank him and Sarah Hirthe for giving me a tour of Barcelona, which I thought would not be possible due to the pandemic! I thank Simon for the weekly "jogging-and-studying" sessions and for bringing up topics that I can reflect upon! He is one of the most-motivated and self-driven persons I have ever met, and I learned not only about physics, but also about many other topics–from politics to music to culture–from the discussions . More importantly, our conversations also kept me motivated and I thank him for always begin candid and sincere. I am also indebted to Roman Bause, Niko Lorenz, Fabian Schmidt for taking the time to listen to any of my preparatory talks for conferences and job interviews.

I would like to thank the group secretaries Kristina Schuldt and Ildiko Kecskesi for the incredible organization of group activities and for taking care of all my administrative-related works so that I could focus on my research. They were always full of creative ideas for the group activities, and they went far beyond their defined job duties. Thanks to Kristina, I was able to find my housing in Munich easily and get settled quickly. Moreover, she always strived to foster the best group atmosphere, recognizing what group members needed even before we mentioned our needs and problems. I also thank her for being patient and understanding with my last-minute requests, especially toward the end of my PhD. I also greatly appreciate Idiko's help in organizing my PhD defense and greeting me with a smile whenever I went to her office–despite all my last-minute requests. Without her help, it would have been very challenging for me to graduate in time. I have no doubt that they are the best secretaries in the world!

Another great thank you goes to my dearest friends. I thank Henrik Dryer for helping me settle in from the very beginning, introducing me to new people, and inviting me to his parties. Now that I am all by myself here in Boston after my PhD, I realized how much help that was. In particular, from him, I got to know a very special person who became my flatmate and best friend, Caroline De Groot. She accompanied throughout my PhD journey, and because of her, I was always happy to come back home after exhausting lab days. I thank Caroline for always being there to listen to my beefs, taking me out of the lab for long walks, organizing fun activities such as movie, game, and dinner nights, and camping events, and decorating the house so that I felt the comfort of home. She enriched my life in Munich, and I thank her for providing me with a social circle that I can count on anytime. I also thank Ritika Dagar for being a great friend, for her awesome chai tea, and for not minding me peeking through her window to check whether she was around for a chat (especially when David left!). Moreover, thank her for joining my writing sessions in Soulmade on weekends. In particular, I loved how we would both say we would wake up early and go to Soulmade together, but we both would end up sleeping in until noon. This always gave me the laughter I needed during stressful writing times. Moreover, I enjoyed Albert Gasull's visits to Riemerfeldring and giving me an excuse to make lots of chicken nuggets. I also thank Dom Wild for completing our gang in my last year and enriching our group atmosphere with his wittiness. Lastly, I thank Caroline, Ritika, and Albert for taking care of all the belongings I have had to leave behind in the house and

for shipping everything to Boston!

A great thanks also go to my friends in Canada: Anffany Chen, Tamiko Masuda, and Anna Lee. Even though I was far away, they were always ready on online chats to support me despite the time differences and busy schedules, especially when I was settling into a foreign country. In particular, I would like to thank Anna for proofreading this thesis. She gave me the suggestions so quickly. I would send her my writing, and the next morning, I would have the feedback (thanks to the time difference!) In addition, I would also like to thank my undergraduate thesis supervisor, Stefan A. Reinsberg, for teaching me the passion for research for the first time, which rooted my drive to achieve this work. Moreover, I thank him for always greeting me with a big smile when I visited Vancouver.

I would like to also thank the Performing Arts Studio (PAS) for having classes taught by very passionate teachers throughout the day, sometimes even on holidays, so that I can keep both my mind and body healthy.

Finally, I would like to thank my family for their love and for supporting me to come to this point. I know that me going so far away from home wasn't too easy for them, especially when the journey took longer than I anticipated. However, regardless, they never cast doubt on my decisions.

Last but certainly not least, a special thanks go to David T. Stephen for countless things– the support that cannot be described in words. He not only gave me practical advice and helped me through my PhD work, always happy to discuss my project and proofread any of my writing, including this thesis, but also was the main source who kept me sane throughout my work. He was extremely patient and understanding when my frustration level peaked and his warmth and support gave me the strength to finish my PhD strong. Most importantly, I thank him for all the wonderful memories, being present at all aspects of my life, and for showing me that there is more to life than my work.

Bibliography

[1] Gross, C. and I. Bloch. *Quantum simulations with ultracold atoms in optical lattices*, Science **357**, 995 (2017). DOI: 10.1126/science.aal3837.

[2] Buluta, I., S. Ashhab, and F. Nori. *Natural and artificial atoms for quantum computation*, Rep. Prog. Phys. **74**., 104401 (2011). DOI: 10.1088/0034-4885/74/10/104401.

[3] Ludlow, A. D., M. M. Boyd, J. Ye, E. Peik, and P. O. Schmidt. *Optical atomic clocks*, Rev. Mod. Phys. **87**, 637 (2015). DOI: 10.1103/RevModPhys.87.637.

[4] Cronin, A. D., J. Schmiedmayer, and D. E. Pritchard. *Optics and interferometry with atoms and molecules*, Rev. Mod. Phys. **81**, 1051 (2009). DOI: 10.1103/RevModPhys.81.1051.

[5] Anderson, M. H., J. R. Ensher, M. R. Matthews, C. E. Wieman, and E. A. Cornell. *Observation of Bose-Einstein Condensation in a Dilute Atomic Vapor*, Science **269**., 198–201 (1995). DOI: 10.1126/science.269.5221.198. URL: https://www.science.org/doi/abs/10.1126/science.269.5221.198.

[6] Davis, K. B., M. .-.-O. Mewes, M. R. Andrews, N. J. van Druten, D. S. Durfee, D. M. Kurn, and W. Ketterle. *Bose-Einstein Condensation in a Gas of Sodium Atoms*, Phys. Rev. Lett. **75**, 3969–3973 (Nov. 1995). DOI: 10.1103/PhysRevLett.75.3969. URL: https://link.aps.org/doi/10.1103/PhysRevLett.75.3969.

[7] Jessen, P. S. and I. H. Deutsch. *Optical Lattices*, Adv. Mol. Opt. Phys. **37**, 95 (1996). DOI: 10.1016/S1049-250X(08)60099-3.

[8] Bloch, I., J. Dalibard, and S. Nascimbène. *Quantum simulations with ultracold quantum gases*, Nature Physics **8**, 267 (2012). DOI: 10.1038/nphys2259.

[9] Greiner, M., O. Mandel, T. Esslinger, T. W. Hänsch, and I. Bloch. *Quantum phase transition from a superfluid to a Mott insulator in a gas of ultracold atoms*, Nature **415**, 39 (2002). DOI: 10.1038/415039a.

[10] Jördens, R., N. Strohmaier, K. Günter, H. Moritz, and T. Esslinger. *A Mott insulator of fermionic atoms in an optical lattice*, Nature **455**., 204–207 (Sept. 2008). ISSN: 1476-4687. DOI: 10.1038/nature07244. URL: https://doi.org/10.1038/nature07244.

[11] Schneider, U., L. Hackermüller, S. Will, T. Best, I. Bloch, T. A. Costi, R. W. Helmes, D. Rasch, and A. Rosch. *Metallic and Insulating Phases of Repulsively Interacting Fermions in a 3D Optical Lattice*, Science **322**., 1520–1525eprint: https://www.science.org/doi/pdf/10.1126/science.1165449 (2008). DOI: 10.1126/science.1165449. URL: https://www.science.org/doi/abs/10.1126/science.1165449.

[12] Greif, D., T. Uehlinger, G. Jotzu, L. Tarruell, and T. Esslinger. *Short-Range Quantum Magnetism of Ultracold Fermions in an Optical Lattice*, Science **340**., 1307–1310eprint: https://www.science.org/doi/pdf/10.1126/science.1236362 (2013). DOI: 10.1126/science.1236362. URL: https://www.science.org/doi/abs/10.1126/science.1236362.

[13] Hart, R. A., P. M. Duarte, T.-L. Yang, X. Liu, T. Paiva, E. Khatami, R. T. Scalettar, N. Trivedi, D. A. Huse, and R. G. Hulet. *Observation of antiferromagnetic correlations in the Hubbard model with ultracold atoms*, Nature **519**., 211–214 (Mar. 2015). ISSN: 1476-4687. DOI: 10.1038/nature14223. URL: https://doi.org/10.1038/nature14223.

[14] Esslinger, T. *Fermi-Hubbard Physics with Atoms in an Optical Lattice*, Annual Review of Condensed Matter Physics **1**, 129 (2010). DOI: 10.1146/annurev-conmatphys-070909-104059.

[15] Brennen, G. K., D. Song, and C. J. Williams. *Quantum-computer architecture using nonlocal interactions*, Phys. Rev. A **67**, 050302 (May 2003). DOI: 10.1103/PhysRevA.67.050302. URL: https://link.aps.org/doi/10.1103/PhysRevA.67.050302.

[16] Pachos, J. K. and P. L. Knight. *Quantum Computation with a One-Dimensional Optical Lattice*, Phys. Rev. Lett. **91**, 107902 (Sept. 2003). DOI: 10.1103/PhysRevLett.91.107902. URL: https://link.aps.org/doi/10.1103/PhysRevLett.91.107902.

[17] Vega, I. de, D. Porras, and J. I. Cirac. *Matter-Wave Emission in Optical Lattices: Single Particle and Collective Effects*, Phys. Rev. Lett. **101**, 260404 (2008). DOI: 10.1103/PhysRevLett.101.260404.

[18] Navarrete-Benlloch, C., I. de Vega, D. Porras, and J. I. Cirac. *Simulating quantum-optical phenomena with cold atoms in optical lattices*, **13**., 023024 (Feb. 2011). DOI: 10.1088/1367-2630/13/2/023024. URL: https://doi.org/10.1088/1367-2630/13/2/023024.

[19] Krinner, L., M. Stewart, A. Pazmiño, J. Kwon, and D. Schneble. *Spontaneous emission of matter waves from a tunable open quantum system*, Nature **559**, 589 (2018). DOI: 10.1038/s41586-018-0348-z.

[20] Stewart, M., J. Kwon, A. Lanuza, and D. Schneble. *Dynamics of matter-wave quantum emitters in a structured vacuum*, Phys. Rev. Research **2**, 043307 (Dec. 2020). DOI: 10.1103/PhysRevResearch.2.043307. URL: https://link.aps.org/doi/10.1103/PhysRevResearch.2.043307.

[21] Daley, A., M. Boyd, J. Ye, and P. Zoller. *Quantum Computing with Alkaline-Earth-Metal Atoms*, Phys. Rev. Lett. **101**, 170504 (2008). DOI: 10.1103/PhysRevLett.101.170504.

[22] Takamoto, M., F.-L. Hong, R. Higashi, and H. Katori. *An optical lattice clock*, Nature **435**, 321 (2005). DOI: 10.1038/nature03541.

[23] Abdel-Hafiz, M. *et al. Guidelines for developing optical clocks with* 10^{-18} *fractional frequency uncertainty*, arXiv: 1906.11495 (2019).

[24] Oelker, E. *et al. Demonstration of* 4.8×10^{-17} *stability at 1 s for two independent optical clocks*, Nature Photonics **13**., 714–719 (Oct. 2019). ISSN: 1749-4893. DOI: 10.1038/s41566-019-0493-4. URL: https://doi.org/10.1038/s41566-019-0493-4.

[25] Ye, J., H. J. Kimble, and H. Katori. *Quantum state engineering and precision metrology using state-insensitive light traps*, Science **320**, 1734 (2008). DOI: 10.1126/science.1148259.

[26] Katori, H., K. Hashiguchi, E. Y. Il'inova, and V. D. Ovsiannikov. *Magic Wavelength to Make Optical Lattice Clocks Insensitive to Atomic Motion*, Phys. Rev. Lett. **103**, 153004 (Oct. 2009). DOI: 10.1103/PhysRevLett.103.153004. URL: https://link.aps.org/doi/10.1103/PhysRevLett.103.153004.

[27] Daley, A. J., J. Ye, and P. Zoller. *State-dependent lattices for quantum computing with alkaline-earth-metal atoms*, Eur. Phys. J. D **65**, 207 (2011). DOI: 10.1140/epjd/e2011-20095-2.

[28] Daley, A. J. *Quantum computing and quantum simulation with group-II atoms*, Quantum Inf. Process. **10**, 865 (2011). DOI: 10.1007/s11128-011-0293-3.

[29] Gorshkov, A. V., A. M. Rey, A. J. Daley, M. M. Boyd, J. Ye, P. Zoller, and M. D. Lukin. *Alkaline-Earth-Metal Atoms as Few-Qubit Quantum Registers*, Phys. Rev. Lett. **102**, 110503 (2009). DOI: 10.1103/PhysRevLett.102.110503.

[30] Herold, C. D., V. D. Vaidya, X. Li, S. L. Rolston, J. V. Porto, and M. S. Safronova. *Precision Measurement of Transition Matrix Elements via Light Shift Cancellation*, Phys. Rev. Lett. **109**, 243003 (2012). DOI: 10.1103/PhysRevLett.109.243003.

[31] González-Tudela, A. and J. I. Cirac. *Non-Markovian quantum optics with three-dimensional state-dependent optical lattices*, Quantum **2**, 97 (2018). DOI: 10.22331/q-2018-10-01-97.

[32] González-Tudela, A. and J. I. Cirac. *Quantum Emitters in Two-Dimensional Structured Reservoirs in the Nonperturbative Regime*, Phys. Rev. Lett. **119**, 143602 (2017). DOI: 10.1103/PhysRevLett.119.143602.

[33] González-Tudela, A. and J. I. Cirac. *Markovian and non-Markovian dynamics of quantum emitters coupled to two-dimensional structured reservoirs*, Phys. Rev. A **96**, 043811 (2017). DOI: 10.1103/PhysRevA.96.043811.

[34] Argüello-Luengo, J., A. González-Tudela, T. Shi, P. Zoller, and J. I. Cirac. *Analogue quantum chemistry simulation*, Nature **574**, 215 (2019). DOI: 10.1038/s41586-019-1614-4.

[35] Katori, H., T. Ido, Y. Isoya, and M. Kuwata-Gonokami. *Magneto-Optical Trapping and Cooling of Strontium Atoms down to the Photon Recoil Temperature*, Phys. Rev. Lett. **82**, 1116 (1999). DOI: 10.1103/PhysRevLett.82.1116.

[36] Raab, E. L., M. Prentiss, A. Cable, S. Chu, and D. E. Pritchard. *Trapping of Neutral Sodium Atoms with Radiation Pressure*, Phys. Rev. Lett. **59**, 2631–2634 (Dec. 1987). DOI: 10.1103/PhysRevLett.59.2631. URL: https://link.aps.org/doi/10.1103/PhysRevLett.59.2631.

[37] Stellmer, S., R. Grimm, and F. Schreck. *Production of quantum-degenerate strontium gases*, Phys. Rev. A **87**, 013611 (2013). DOI: 10.1103/PhysRevA.87.013611.

[38] Stellmer, S., B. Pasquiou, R. Grimm, and F. Schreck. *Laser Cooling to Quantum Degeneracy*, Phys. Rev. Lett. **110**, 263003 (2013). DOI: 10.1103/PhysRevLett.110.263003.

[39] Snigirev, S., A. J. Park, A. Heinz, I. Bloch, and S. Blatt. *Fast and dense magneto-optical traps for strontium*, Phys. Rev. A **99**, 063421 (2019). DOI: 10.1103/PhysRevA.99.063421.

[40] Heinz, A., A. J. Park, N. Šantić, J. Trautmann, S. G. Porsev, M. S. Safronova, I. Bloch, and S. Blatt. *State-dependent optical lattices for the strontium optical qubit*, Phys. Rev. Lett. **124**, 203201 (2020).

[41] Heinz, A., J. Trautmann, N. Šantić, A. J. Park, I. Bloch, and S. Blatt. *Crossed optical cavities with large mode diameters*, Opt. Lett. **46**, 250 (2021). DOI: 10.1364/OL.414076.

[42] Park, A. J., J. Trautmann, N. Šantić, V. Klüsener, A. Heinz, I. Bloch, and S. Blatt. *Cavity-enhanced optical lattices for scaling neutral atom quantum technologies*, arXiv: 2109.02243 (2021).

[43] Metcalf, H. J. and P. van der Straten. *Laser cooling and Trapping*. Ed. by Birman, J. L., J. W. Lynn, H. E. Stanley, M. P. Silverman, and M. Voloshin. Springer Science and Business Media, 1999. ISBN: 0387987479, 9780387987477.

[44] Steane, A. M. and C. J. Foot. *Laser Cooling below the Doppler Limit in a Magneto-Optical Trap*, **14**., 231–236 (Feb. 1991). DOI: 10.1209/0295-5075/14/3/008. URL: https://doi.org/10.1209/0295-5075/14/3/008.

[45] Shang, S.-Q., B. Sheehy, H. Metcalf, P. van der Straten, and G. Nienhuis. *Velocity-selective resonances and sub-Doppler laser cooling*, Phys. Rev. Lett. **67**, 1094–1097 (Aug. 1991). DOI: 10.1103/PhysRevLett.67.1094. URL: https://link.aps.org/doi/10.1103/PhysRevLett.67.1094.

[46] Modugno, G., Benk ő, P. Hannaford, G. Roati, and M. Inguscio. *Sub-Doppler laser cooling of fermionic ^{40}K atoms*, Phys. Rev. A **60**, R3373–R3376 (Nov. 1999). DOI: 10.1103/PhysRevA.60.R3373. URL: https://link.aps.org/doi/10.1103/PhysRevA.60.R3373.

[47] Lett, P. D., R. N. Watts, C. I. Westbrook, W. D. Phillips, P. L. Gould, and H. J. Metcalf. *Observation of Atoms Laser Cooled below the Doppler Limit*, Phys. Rev. Lett. **61**, 169–172 (July 1988). DOI: 10.1103/PhysRevLett.61.169. URL: https://link.aps.org/doi/10.1103/PhysRevLett.61.169.

[48] Dalibard, J. and C. Cohen-Tannoudji. *Laser cooling below the Doppler limit by polarization gradients: simple theoretical models*, J. Opt. Soc. Am. B **6**., 2023–2045 (Nov. 1989). DOI: 10.1364/JOSAB.6.002023. URL: http://www.osapublishing.org/josab/abstract.cfm?URI=josab-6-11-2023.

[49] Loftus, T. H., T. Ido, M. M. Boyd, A. D. Ludlow, and J. Ye. *Narrow line cooling and momentum-space crystals*, Phys. Rev. A **70**, 063413 (2004). DOI: 10.1103/PhysRevA.70.063413.

[50] Grimm, R., M. Weidemüller, and Y. B. Ovchinnikov. *Optical dipole traps for neutral atoms*, Adv. At. Mol. Opt. Phys. **42**, 95 (2000). DOI: 10.1016/S1049-250X(08)60186-X.

[51] Pichler, H., A. J. Daley, and P. Zoller. *Nonequilibrium dynamics of bosonic atoms in optical lattices: Decoherence of many-body states due to spontaneous emission*, Phys. Rev. A **82**, 063605 (2010). DOI: 10.1103/PhysRevA.82.063605.

[52] Trotzky, S., L. Pollet, F. Gerbier, U. Schnorrberger, I. Bloch, N. Prokof'Ev, B. Svistunov, and M. Troyer. *Suppression of the critical temperature for superfluidity near the Mott transition*, Nat. Phys. **6**., 998 (2010). DOI: 10.1038/nphys1799.

[53] Blatt, S., A. Mazurenko, M. F. Parsons, C. S. Chiu, F. Huber, and M. Greiner. *Low-noise optical lattices for ultracold ^{6}Li*, Phys. Rev. A **92**, 021402(R) (2015). DOI: 10.1103/PhysRevA.92.021402.

[54] Muniz, J. A., D. J. Young, J. R. K. Cline, and J. K. Thompson. *Cavity-QED measurements of the ^{87}Sr millihertz optical clock transition and determination of its natural linewidth*, Phys. Rev. Research **3**, 023152 (May 2021). DOI: 10.1103/PhysRevResearch.3.023152. URL: https://link.aps.org/doi/10.1103/PhysRevResearch.3.023152.

[55] Heinz, A. "Ultracold strontium in state-Dependent optical lattices." PhD thesis. Ludwig-Maximilians-Universität München, Department of Physics, 2020. URL: 10.5282/edoc.26329.

[56] Nicholson, T. *et al. Systematic evaluation of an atomic clock at 2 × 1018 total uncertainty*, Nat. Commun. **6**, 6896 (2015). DOI: 10.1038/ncomms7896.

[57] Cooper, A., J. P. Covey, I. S. Madjarov, S. G. Porsev, M. S. Safronova, and M. Endres. *Alkaline-Earth Atoms in Optical Tweezers*, Phys. Rev. X **8**, 041055 (2018). DOI: 10.1103/PhysRevX.8.041055.

[58] Xu, X., T. H. Loftus, J. L. Hall, A. Gallagher, and J. Ye. *Cooling and trapping of atomic strontium*, J. Opt. Soc. Am. B **20**., 968–976 (May 2003). DOI: 10.1364/JOSAB.20.000968. URL: http://www.osapublishing.org/josab/abstract.cfm?URI=josab-20-5-968.

[59] Nosske, I., L. Couturier, F. Hu, C. Tan, C. Qiao, J. Blume, Y. H. Jiang, P. Chen, and M. Weidemüller. *Two-dimensional magneto-optical trap as a source for cold strontium atoms*, Phys. Rev. A **96**, 053415 (Nov. 2017). DOI: 10.1103/PhysRevA.96.053415. URL: https://link.aps.org/doi/10.1103/PhysRevA.96.053415.

[60] Yasuda, M. and H. Katori. *Lifetime Measurement of the $^3P_2$ Metastable State of Strontium Atoms*, Phys. Rev. Lett. **92**, 153004 (Apr. 2004). DOI: 10.1103/PhysRevLett.92.153004. URL: https://link.aps.org/doi/10.1103/PhysRevLett.92.153004.

[61] Stellmer, S. "Degenerate quantum gases of strontium." PhD thesis. University of Innsbruck, Faculty of Mathematics, Computer Science and Physics, 2013. URL: 10.5282/edoc.26329.

[62] Stellmer, S., M. K. Tey, B. Huang, R. Grimm, and F. Schreck. *Bose-Einstein Condensation of Strontium*, Phys. Rev. Lett. **103**, 200401 (Nov. 2009). DOI: 10.1103/PhysRevLett.103.200401. URL: https://link.aps.org/doi/10.1103/PhysRevLett.103.200401.

[63] Chanelière, T., L. He, R. Kaiser, and D. Wilkowski. *Three dimensional cooling and trapping with a narrow line*, Eur. Phys. J. D **46**, 507 (2008). DOI: 10.1140/epjd/e2007-00329-8.

[64] Mukaiyama, T., H. Katori, T. Ido, Y. Li, and M. Kuwata-Gonokami. *Recoil-Limited Laser Cooling of ^{87}Sr Atoms near the Fermi Temperature*, Phys. Rev. Lett. **90**, 113002 (2003). DOI: 10.1103/PhysRevLett.90.113002.

[65] Boyd, M. M. "High Precision Spectroscopy of Strontium in an Optical Lattice: Towards a New Standard for Frequency and Time." PhD thesis. University of Colorado, Department of Physics, 2007. URL: https://jila.colorado.edu/publications/theses.

[66] Norcia, M. A., J. R. K. Cline, J. P. Bartolotta, M. J. Holland, and J. K. Thompson. *Narrow-line laser cooling by adiabatic transfer*, N. J. Phys. **20**, 023021 (2018). DOI: 10.1088/1367-2630/aaa950.

[67] Muniz, J. A., M. A. Norcia, J. R. K. Cline, and J. K. Thompson. *A Robust Narrow-Line Magneto-Optical Trap using Adiabatic Transfer*, arXiv: 1806.00838v1 (2018).

[68] Bartolotta, J. P., M. A. Norcia, J. R. K. Cline, J. K. Thompson, and M. J. Holland. *Laser Cooling by Sawtooth Wave Adiabatic Passage*, Phys. Rev. A **98**, 023404 (2018). DOI: 10.1103/PhysRevA.98/023404.

[69] Petersen, N., F. Mühlbauer, L. Bougas, A. Sharma, D. Budker, and P. Windpassinger. *Sawtooth-wave adiabatic-passage slowing of dysprosium*, Phys. Rev. A **99**, 063414 (June 2019). DOI: 10.1103/PhysRevA.99.063414. URL: https://link.aps.org/doi/10.1103/PhysRevA.99.063414.

[70] Ido, T. and H. Katori. *Recoil-Free Spectroscopy of Neutral Sr Atoms in the Lamb-Dicke Regime*, Phys. Rev. Lett. **91**, 053001 (2003). DOI: 10.1103/PhysRevLett.91.053001.

[71] Boyd, M., T. Zelevinsky, A. Ludlow, S. Blatt, T. Zanon-Willette, S. Foreman, and J. Ye. *Nuclear spin effects in optical lattice clocks*, Phys. Rev. A **76**, 022510 (2007). DOI: 10.1103/PhysRevA.76.022510.

[72] Taichenachev, A. V., V. I. Yudin, C. W. Oates, C. W. Hoyt, Z. W. Barber, and L. Hollberg. *Magnetic Field-Induced Spectroscopy of Forbidden Optical Transitions with Application to Lattice-Based Optical Atomic Clocks*, Phys. Rev. Lett. **96**, 083001 (2006). DOI: 10.1103/PhysRevLett.96.083001.

[73] Blatt, S., J. W. Thomsen, G. K. Campbell, A. D. Ludlow, M. D. Swallows, M. J. Martin, M. M. Boyd, and J. Ye. *Rabi spectroscopy and excitation inhomogeneity in a one-dimensional optical lattice clock*, Phys. Rev. A **80**, 052703 (2009). DOI: 10.1103/PhysRevA.80.052703.

[74] Kuhr, S. *Quantum-gas microscopes: a new tool for cold-atom quantum simulators*, National Science Review **3**., 170–172eprint: https://academic.oup.com/nsr/article-pdf/3/2/170/31565423/nww023.pdf (Apr. 2016). ISSN: 2095-5138. DOI: 10.1093/nsr/nww023. URL: https://doi.org/10.1093/nsr/nww023.

[75] Gross, C. and W. S. Bakr. *Quantum gas microscopy for single atom and spin detection*, arXiv: 2010.15407v1 (2020).

[76] Gorshkov, A. V., M. Hermele, V. Gurarie, C. Xu, P. S. Julienne, J. Ye, P. Zoller, E. Demler, M. D. Lukin, and A. M. Rey. *Two-orbital SU(N) magnetism with ultracold alkaline-earth atoms*, Nat. Phys. **6**, 289 (2010). DOI: 10.1038/nphys1535.

[77] Zhang, X., M. Bishof, S. L. Bromley, C. V. Kraus, M. S. Safronova, P. Zoller, A. M. Rey, and J. Ye. *Spectroscopic observation of SU(N)-symmetric interactions in Sr orbital magnetism*, Science **345**, 1467 (2014). DOI: 10.1126/science.1254978.

[78] Porsev, S. G. and A. Derevianko. *Hyperfine quenching of the metastable* $^3P_{0,2}$ *states in divalent atoms*, Phys. Rev. A **69**, 042506 (Apr. 2004). DOI: 10.1103/PhysRevA.69.042506. URL: https://link.aps.org/doi/10.1103/PhysRevA.69.042506.

[79] Yamaguchi, A. "Metastable State of Ultracold and Quantum Degenerate Ytterbium Atoms: High-Resolution Spectroscopy and Cold Collisions." PhD thesis. Kyoto University, 2008. URL: yagura.scphys.kyoto-u.ac.jp/publications/thesis/PhD_yamaguchi.pdf.

[80] Onishchenko, O., S. Pyatchenkov, A. Urech, C.-C. Chen, S. Bennetts, G. A. Siviloglou, and F. Schreck. *Frequency of the ultranarrow* $^1S_0 - ^3P_2$ *transition in* ^{87}Sr, Phys. Rev. A **99**, 052503 (May 2019). DOI: 10.1103/PhysRevA.99.052503. URL: https://link.aps.org/doi/10.1103/PhysRevA.99.052503.

[81] Yamaguchi, A., S. Uetake, S. Kato, H. Ito, and Y. Takahashi. *High-resolution laser spectroscopy of a Bose–Einstein condensate using the ultranarrow magnetic quadrupole transition*, **12.**, 103001 (Oct. 2010). DOI: 10.1088/1367-2630/12/10/103001. URL: https://doi.org/10.1088/1367-2630/12/10/103001.

[82] Heinz, A. "Ultracold strontium in state-dependent optical lattices." PhD thesis. Ludwig-Maximilians-Universität München, Department of Physics, 2020. URL: edoc.ub.uni-muenchen.de/26329/.

[83] Lundblad, N., M. Schlosser, and J. V. Porto. *Experimental observation of magic-wavelength behavior of* ^{87}Rb *atoms in an optical lattice*, Phys. Rev. A **81**, 031611 (Mar. 2010). DOI: 10.1103/PhysRevA.81.031611. URL: https://link.aps.org/doi/10.1103/PhysRevA.81.031611.

[84] Leonard, R. H., A. J. Fallon, C. A. Sackett, and M. S. Safronova. *High-precision measurements of the* ^{87}*Rb* D*-line tune-out wavelength*, Phys. Rev. A **92**, 052501 (2015). DOI: 10.1103/PhysRevA.92.052501.

[85] Blatt, S. *et al. New Limits on Coupling of Fundamental Constants to Gravity Using* ^{87}*Sr Optical Lattice Clocks*, Phys. Rev. Lett. **100**, 140801 (2008). DOI: 10.1103/PhysRevLett.100.140801.

[86] Blatt, S. "Ultracold Collisions and Fundamental Physics with Strontium." PhD thesis. University of Colorado, Department of Physics, 2011. URL: https://jila.colorado.edu/publications/theses.

[87] Leibfried, D., R. Blatt, C. Monroe, and D. Wineland. *Quantum dynamics of single trapped ions*, Rev. Mod. Phys. **75**, 281 (2003). DOI: 10.1103/RevModPhys.75.281.

[88] Bloch, I., J. Dalibard, and W. Zwerger. *Many-body physics with ultracold gases*, Rev. Mod. Phys. **80**, 885 (2008). DOI: 10.1103/RevModPhys.80.885.

[89] Campbell, G. K. *et al. Probing Interactions Between Ultracold Fermions*, Science **324.**, 360–363 (2009). DOI: 10.1126/science.1169724.

[90] Lemke, N. D., J. von Stecher, J. A. Sherman, A. M. Rey, C. W. Oates, and A. D. Ludlow. *p-Wave Cold Collisions in an Optical Lattice Clock*, Phys. Rev. Lett. **107**, 103902 (Aug. 2011). DOI: 10.1103/PhysRevLett.107.103902. URL: https://link.aps.org/doi/10.1103/PhysRevLett.107.103902.

[91] Martin, M. J., M. Bishof, M. D. Swallows, X. Zhang, C. Benko, J. von-Stecher, A. V. Gorshkov, A. M. Rey, and J. Ye. *A Quantum Many-Body Spin System in an Optical Lattice Clock*, Science **341**, 632 (2013). DOI: 10.1126/science.1236929.

[92] Swallows, M. D., M. Bishof, Y. Lin, S. Blatt, M. J. Martin, A. M. Rey, and J. Ye. *Suppression of Collisional Shifts in a Strongly Interacting Lattice Clock*, Science **331**., 1043–1046 (2011). DOI: 10.1126/science.1196442.

[93] Akatsuka, T., M. Takamoto, and H. Katori. *Three-dimensional optical lattice clock with bosonic ^{88}Sr atoms*, Phys. Rev. A **81**, 023402 (2010). DOI: 10.1103/PhysRevA.81.023402.

[94] Campbell, S. L. *et al. A Fermi-degenerate three-dimensional optical lattice clock*, Science **358**, 90 (2017). DOI: 10.1126/science.aam5538.

[95] Wei, D. *et al. Quantum gas microscopy of Kardar-Parisi-Zhang superdiffusion*, arXiv: 1806.00838v1 (2021).

[96] Gall, M., N. Wurz, J. Samland, C. F. Chan, and M. Köhl. *Competing magnetic orders in a bilayer Hubbard model with ultracold atoms*, Nature **589**, 40 (2021). DOI: 10.1038/s41586-020-03058-x.

[97] Lodewyck, J., P. G. Westergaard, A. Lecallier, L. Lorini, and P. Lemonde. *Frequency stability of optical lattice clocks*, New Journal of Physics **12**, 065026 (2010). DOI: 10.1088/1367-2630/12/6/065026.

[98] Yamamoto, R., J. Kobayashi, T. Kuno, K. Kato, and Y. Takahashi. *An ytterbium quantum gas microscope with narrow-line laser cooling*, **18**., 023016 (Feb. 2016). DOI: 10.1088/1367-2630/18/2/023016. URL: https://doi.org/10.1088/1367-2630/18/2/023016.

[99] Greiner, M. "Ultracold quantum gases in three-dimensional optical lattice potentials." PhD thesis. Ludwig-Maximilians-Universität München, Department of Physics, 2003. URL: https://edoc.ub.uni-muenchen.de/968/1/Greiner_Markus.pdf.

[100] Will, S. "Interacting bosons and fermions in three-dimensional optical lattice potentials: from atom optics to quantum simulation." PhD thesis. Johannes Gutenberg-Universität Mainz, Department of Physics, 2011. URL: https://pdfs.semanticscholar.org/e081/b3dad5eb6cb849aa9eb38dc358d09ec198c4.pdf.

[101] Kwon, J., Y. Kim, A. Lanuza, and D. Schneble. *Formation of Matter-Wave Polaritons in an Optical Lattice*, arXiv: 2109.02243 (2021).

[102] Staub, E. "Developing a High-Flux Atomic Beam Source for Experiments with Ultracold Strontium Quantum Gases." PhD thesis. Ludwig-Maximilians-Universität München, Department of Physics, 2019. URL: ultracold.sr/publications.

[103] Casotti, E. "A Two-dimensional Magneto-optical Trap for Strontium." PhD thesis. Ludwig-Maximilians-Universität München, Department of Physics, 2020. URL: ultracold.sr/publications.

[104] Raj, R. K., D. Bloch, J. J. Snyder, G. Camy, and M. Ducloy. *High-Frequency Optically Heterodyned Saturation Spectroscopy Via Resonant Degenerate Four-Wave Mixing*, Phys. Rev. Lett. **44**, 1251–1254 (May 1980). DOI: 10.1103/PhysRevLett.44.1251. URL: https://link.aps.org/doi/10.1103/PhysRevLett.44.1251.

[105] Miyake, H., N. C. Pisenti, P. K. Elgee, A. Sitaram, and G. K. Campbell. *Isotope shift spectroscopy of the* $^1\mathrm{S}_0 \rightarrow {}^3\mathrm{P}_1$ *and* $^1\mathrm{S}_0 \rightarrow {}^3\mathrm{P}_0$ *transitions in strontium*, Phys. Rev. Research **1**, 033113 (2019). DOI: 10.1103/PhysRevResearch.1.033113.

[106] Janša, N. "A frequency-stable diode laser system for spectroscopy and trapping of Sr atoms." PhD thesis. Ludwig-Maximilians-Universität München, Department of Physics, 2016. URL: ultracold.sr/publications.

[107] Martin, M. J. "Quantum Metrology and Many-Body Physics: Pushing the Frontier of the Optical Lattice Clock." PhD thesis. University of Colorado, Department of Physics, 2013. URL: https://jila.colorado.edu/publications/theses.

[108] Haindl, R. "A Clock Laser System for Quantum Simulations with Ultracold Strontium Atoms." PhD thesis. Ludwig-Maximilians-Universität München, Department of Physics, 2019. URL: ultracold.sr/publications.

[109] Wallner, F. "New tools for controlling strontium atoms with high spectral and spatial resolution." PhD thesis. Technischen Universität München, Department of Physics, 2020. URL: ultracold.sr/publications.

[110] Barker, D. S., B. J. Reschovsky, N. C. Pisenti, and G. K. Campbell. *Enhanced magnetic trap loading for atomic strontium*, Phys. Rev. A **92**, 043418 (Oct. 2015). DOI: 10.1103/PhysRevA.92.043418. URL: https://link.aps.org/doi/10.1103/PhysRevA.92.043418.

[111] Zelevinsky, T., M. Boyd, A. Ludlow, T. Ido, J. Ye, R. Ciuryło, P. Naidon, and P. Julienne. *Narrow Line Photoassociation in an Optical Lattice*, Phys. Rev. Lett. **96**, 203201 (2006). DOI: 10.1103/PhysRevLett.96.203201.

[112] Yang, T., K. Pandey, M. S. Pramod, F. Leroux, C. C. Kwong, E. Hajiyev, Z. Y. Chia, B. Fang, and D. Wilkowski. *A high flux source of cold strontium atoms*, Eur. Phys. J. D **69** (2015).

[113] Nagel, S., P. Mickelson, A. Saenz, Y. Martinez, Y. Chen, T. Killian, P. Pellegrini, and R. Côté. *Photoassociative Spectroscopy at Long Range in Ultracold Strontium*, Phys. Rev. Lett. **94**, 083004 (2005). DOI: 10.1103/PhysRevLett.94.083004.

[114] Mickelson, P. G., Y. N. Martinez, A. D. Saenz, S. B. Nagel, Y. C. Chen, T. C. Killian, P. Pellegrini, and R. Côté. *Spectroscopic Determination of the s-Wave Scattering Lengths of ^{86}Sr and ^{88}Sr*, Phys. Rev. Lett. **95**, 223002 (2005). DOI: 10.1103/PhysRevLett.95.223002.

[115] Kien, F. L., P. Schneeweiss, and A. Rauschenbeutel. *Dynamical polarizability of atoms in arbitrary light fields: general theory and application to cesium*, Eur. Phys. J. D **67**, 92 (2013). DOI: 10.1140/epjd/e2013-30729-x.

[116] Manakov, N. L., V. D. Ovsiannikov, and L. P. Rapoport. *Atoms in a laser field*, Phys. Rep. **141**, 320 (1986). DOI: 10.1016/S0370-1573(86)80001-1.

[117] Rosenbusch, P., S. Ghezali, V. A. Dzuba, V. V. Flambaum, K. Beloy, and A. Derevianko. *ac Stark shift of the Cs microwave atomic clock transitions*, Phys. Rev. A **79**, 013404 (Jan. 2009). DOI: 10.1103/PhysRevA.79.013404. URL: https://link.aps.org/doi/10.1103/PhysRevA.79.013404.

[118] Boyd, R. W. *Nonlinear Optics, Third Editio*. Academic Press, Inc, 2008. ISBN: 0128110027.

[119] Steck, D. A. *Quantum and Atom Optics*. Apr. 2019. URL: http://steck.us/teaching.

[120] Kozlov, M. G. and S. G. Porsev. *Polarizabilities and hyperfine structure constants of the low-lying levels of barium*, Eur. Phys. J. D **5**, 59 (1999). DOI: 10.1007/s100530050229.

[121] Safronova, M. S., S. G. Porsev, U. I. Safronova, M. G. Kozlov, and C. W. Clark. *Blackbody-radiation shift in the Sr optical atomic clock*, Phys. Rev. A **87**, 012509 (2013). DOI: 10.1103/PhysRevA.87.012509.

[122] Safronova, M. S., W. R. Johnson, and A. Derevianko. *Relativistic many-body calculations of energy levels, hyperfine constants, electric-dipole matrix elements, and static polarizabilities for alkali-metal atoms*, Phys. Rev. A **60**, 4476 (1999). DOI: 10.1103/PhysRevA.60.4476.

[123] Sansonetti, J. E. and G. Nave. *Wavelengths, transition probabilities, and energy levels for the spectrum of neutral strontium (Sr I)*, J. Phys. Chem. Ref. Data **39**, 033103 (2010). DOI: 10.1063/1.3449176.

[124] Ferrari, G., P. Cancio, R. Drullinger, G. Giusfredi, N. Poli, M. Prevedelli, C. Toninelli, and G. M. Tino. *Precision Frequency Measurement of Visible Intercombination Lines of Strontium*, Phys. Rev. Lett. **91**, 243002 (2003). DOI: 10.1103/PhysRevLett.91.243002.

[125] Yasuda, M., T. Kishimoto, M. Takamoto, and H. Katori. *Photoassociation spectroscopy of ^{88}Sr: Reconstruction of the wave function near the last node*, Phys. Rev. A **73**, 011403(R) (2006). DOI: 10.1103/PhysRevA.73.011403.

[126] Savard, T. A., K. M. O'Hara, and J. E. Thomas. *Laser-noise-induced heating in far-off resonance optical traps*, Phys. Rev. A **56**, R1095 (1997). DOI: 10.1103/PhysRevA.56.R1095.

[127] Lamporesi, G., J. Catani, G. Barontini, Y. Nishida, M. Inguscio, and F. Minardi. *Scattering in Mixed Dimensions with Ultracold Gases*, Physical Review Letters **104**, 153202 (2010). DOI: 10.1103/PhysRevLett.104.153202.

[128] Holmgren, W. F., R. Trubko, I. Hromada, and A. D. Cronin. *Measurement of a Wavelength of Light for Which the Energy Shift for an Atom Vanishes*, Phys. Rev. Lett. **109**, 243004 (2012). DOI: 10.1103/PhysRevLett.109.243004.

[129] Trubko, R., M. D. Gregoire, W. F. Holmgren, and A. D. Cronin. *Potassium tune-out wavelength measurement using atom interferometry and a multipass optical cavity*, Phys. Rev. A **95**, 052507 (2017). DOI: 10.1103/PhysRevA.95.052507.

[130] Copenhaver, E., K. Cassella, R. Berghaus, and H. Müller. *Measurement of a ^{7}Li tune-out wavelength by phase-patterned atom interferometry*, Phys. Rev. A **100**, 063603 (2019). DOI: 10.1103/PhysRevA.100.063603.

[131] Schmidt, F., D. Mayer, M. Hohmann, T. Lausch, F. Kindermann, and A. Widera. *Precision measurement of the ^{87}Rb tune-out wavelength in the hyperfine ground state $F = 1$ at 790 nm*, Phys. Rev. A **93**, 022507 (2016). DOI: 10.1103/PhysRevA.93.022507.

[132] Kao, W., Y. Tang, N. Q. Burdick, and B. L. Lev. *Anisotropic dependence of tune-out wavelength near Dy 741-nm transition*, Opt. Express **25**, 3411 (2017). DOI: 10.1364/OE.25.003411.

[133] Bothwell, T., D. Kedar, E. Oelker, J. M. Robinson, S. L. Bromley, W. L. Tew, J. Ye, and C. J. Kennedy. *JILA SrI optical lattice clock with uncertainty of 2.0×10^{-18}*, Metrologia **56**, 065004 (2019). DOI: 10.1088/1681-7575/ab4089.

[134] Brinkmann, U. *Lebensdauern und Oszillatorstärken im Sr I- und Ca I-Spektrum*, Z. Phys. **228**, 440 (1969). DOI: 10.1007/BF01558342.

[135] Havey, M. D., L. C. Balling, and J. J. Wright. *Direct measurements of excited-state lifetimes in Mg, Ca, and Sr*, J. Opt. Soc. Am. **67**, 488 (1977). DOI: 10.1364/JOSA.67.000488.

[136] Jönsson, G., C. Levinson, A. Persson, and C.-G. Wahlström. *Natural radiative lifetimes in the $^1P_1$ and $^1F_3$ sequences of Sr I*, Z. Phys. A **316**, 255 (1984). DOI: 10.1007/BF01439897.

[137] Weitenberg, C., M. Endres, J. F. Sherson, P. Schauß, T. Fukuhara, I. Bloch, and S. Kuhr. *Single-spin addressing in an atomic Mott insulator*, Nature **471**, 319 (2011). DOI: 10.1038/nature09827.

[138] Bowden, W., R. Hobson, I. R. Hill, A. Vianello, M. Schioppo, A. Silva, H. S. Margolis, P. E. G. Baird, and P. Gill. *A pyramid MOT with integrated optical cavities as a cold atom platform for an optical lattice clock*, Scientific Reports **9**, 11704 (2019). DOI: 10.1038/s41598-019-48168-3.

[139] Cai, Y., D. G. Allman, J. Evans, P. Sabharwal, and K. C. Wright. *Monolithic bowtie cavity traps for ultracold gases*, J. Opt. Soc. Am. B **37**, 3596 (2020). DOI: 10.1364/JOSAB.401262.

[140] Léonard, J., M. Lee, A. Morales, T. M. Karg, T. Esslinger, and T. Donner. *Optical transport and manipulation of an ultracold atomic cloud using focus-tunable lenses*, N. J. Phys. **16**, 093028 (2014). DOI: 10.1088/1367-2630/16/9/093028.

[141] Lisdat, C., J. S. R. V. Winfred, T. Middelmann, F. Riehle, and U. Sterr. *Collisional Losses, Decoherence, and Frequency Shifts in Optical Lattice Clocks with Bosons*, Phys. Rev. Lett. **103**, 090801 (2009). DOI: 10.1103/PhysRevLett.103.090801.

[142] Bishof, M., M. Martin, M. Swallows, C. Benko, Y. Lin, G. Quéméner, A. Rey, and J. Ye. *Inelastic collisions and density-dependent excitation suppression in a ^{87}Sr optical lattice clock*, Phys. Rev. A **84**, 052716 (2011). DOI: 10.1103/PhysRevA.84.052716.

[143] McDonald, M., B. H. McGuyer, G. Z. Iwata, and T. Zelevinsky. *Thermometry via Light Shifts in Optical Lattices*, Phys. Rev. Lett. **114**, 023001 (2015). DOI: 10.1103/PhysRevLett.114.023001.

[144] Han, C., M. Zhou, X. Zhang, Q. Gao, Y. Xu, S. Li, S. Zhang, and X. Xu. *Carrier thermometry of cold ytterbium atoms in an optical lattice clock*, Scientific Reports **8**, 7927 (2018). DOI: 10.1038/s41598-018-26367-8.

[145] Mosk, A., S. Jochim, H. Moritz, T. Elsässer, M. Weidemüller, and R. Grimm. *Resonator-enhanced optical dipole trap for fermionic lithium atoms*, Opt. Lett. **26**, 1837 (2001). URL: http://ol.osa.org/abstract.cfm?URI=ol-26-23-1837.

[146] Harry, G. M. and the LIGO Scientific Collaboration. *Advanced LIGO: the next generation of gravitational wave detectors*, Classical and Quantum Gravity **27**., 084006 (Apr. 2010). DOI: 10.1088/0264-9381/27/8/084006. URL: https://doi.org/10.1088/0264-9381/27/8/084006.

[147] Le Targat, R. *et al. Experimental realization of an optical second with strontium lattice clocks*, Nature communications **4**, 1 (2013). DOI: 10.1038/ncomms3109.

[148] Schiller, S. *et al.* "The space optical clocks project: Development of high-performance transportable and breadboard optical clocks and advanced subsystems," *2012 European Frequency and Time Forum*. IEEE. 2012, p. 412. DOI: 10.1109/EFTF.2012.6502414.

[149] Lemonde, P. and P. Wolf. *Optical lattice clock with atoms confined in a shallow trap*, Phys. Rev. A **72**, 033409 (2005). DOI: 10.1103/PhysRevA.72.033409.

[150] Shi, C., J.-L. Robyr, U. Eismann, M. Zawada, L. Lorini, R. Le Targat, and J. Lodewyck. *Polarizabilities of the ^{87}Sr clock transition*, Phys. Rev. A **92**, 012516 (2015). DOI: 10.1103/PhysRevA.92.012516.

[151] Shibata, K., R. Yamamoto, Y. Seki, and Y. Takahashi. *Optical spectral imaging of a single layer of a quantum gas with an ultranarrow optical transition*, Phys. Rev. A **89**, 031601 (2014). DOI: 10.1103/PhysRevA.89.031601.

[152] Marti, G. E., R. B. Hutson, A. Goban, S. L. Campbell, N. Poli, and J. Ye. *Imaging Optical Frequencies with 100 μHz Precision and 1.1 μm Resolution*, Phys. Rev. Lett. **120**, 103201 (2018). DOI: 10.1103/PhysRevLett.120.103201.

[153] Koller, S. B., J. Grotti, S. Vogt, A. Al-Masoudi, S. Dörscher, S. Häfner, U. Sterr, and C. Lisdat. *Transportable Optical Lattice Clock with 7×10^{-17} Uncertainty*, Physical Review Letters **118**, 073601 (2017).

[154] Grotti, J. *et al. Geodesy and metrology with a transportable optical clock*, Nature Physics **14**, 437 (2018).

[155] Wolf, P. *et al. Quantum physics exploring gravity in the outer solar system: the SAGAS project*, Experimental Astronomy **23**, 651 (2009).

[156] Origlia, S. *et al. Towards an optical clock for space: Compact, high-performance optical lattice clock based on bosonic atoms*, Physical Review A **98**, 053443 (2018).

[157] Saffman, M., T. G. Walker, and K. Mølmer. *Quantum information with Rydberg atoms*, Rev. Mod. Phys. **82**, 2313–2363 (Aug. 2010). DOI: 10.1103/RevModPhys.82.2313. URL: https://link.aps.org/doi/10.1103/RevModPhys.82.2313.

[158] Browaeys, A. and T. Lahaye. *Many-body physics with individually controlled Rydberg atoms*, Nature Physics **16**., 132–142 (Feb. 2020). ISSN: 1745-2481. DOI: 10.1038/s41567-019-0733-z. URL: https://doi.org/10.1038/s41567-019-0733-z.

[159] Wang, Y., S. Shevate, T. M. Wintermantel, M. Morgado, G. Lochead, and S. Whitlock. *Preparation of hundreds of microscopic atomic ensembles in optical tweezer arrays*, npj Quantum Information **6**., 54 (June 2020). ISSN: 2056-6387. DOI: 10.1038/s41534-020-0285-1. URL: https://doi.org/10.1038/s41534-020-0285-1.

[160] John, S. and J. Wang. *Quantum electrodynamics near a photonic band gap: Photon bound states and dressed atoms*, Phys. Rev. Lett. **64**, 2418–2421 (May 1990). DOI: 10.1103/PhysRevLett.64.2418. URL: https://link.aps.org/doi/10.1103/PhysRevLett.64.2418.

[161] Hood, J. D., A. Goban, A. Asenjo-Garcia, M. Lu, S.-P. Yu, D. E. Chang, and H. J. Kimble. *Atom–atom interactions around the band edge of a photonic crystal waveguide*, Proceedings of the National Academy of Sciences **113**., 10507–10512eprint: https://www.pnas.org/content/113/38/10507.full.pdf (2016). ISSN: 0027-8424. DOI: 10.1073/pnas.1603788113. URL: https://www.pnas.org/content/113/38/10507.

[162] González-Tudela, A., C.-L. Hung, D. E. Chang, J. I. Cirac, and H. J. Kimble. *Subwavelength vacuum lattices and atom–atom interactions in two-dimensional photonic crystals*, Nature Photonics **9**., 320–325 (May 2015). ISSN: 1749-4893. DOI: 10.1038/nphoton.2015.54. URL: https://doi.org/10.1038/nphoton.2015.54.

[163] Plankensteiner, D., L. Ostermann, H. Ritsch, and C. Genes. *Selective protected state preparation of coupled dissipative quantum emitters*, Scientific Reports **5**., 16231 (Nov. 2015). ISSN: 2045-2322. DOI: 10.1038/srep16231. URL: https://doi.org/10.1038/srep16231.

[164] Safronova, M. S., Z. Zuhrianda, U. I. Safronova, and C. W. Clark. *Extracting transition rates from zero-polarizability spectroscopy*, Phys. Rev. A **92**, 040501 (2015). DOI: 10.1103/PhysRevA.92.040501.

[165] A. Kramida, Yu. Ralchenko, J. Reader, and and NIST ASD Team. NIST Atomic Spectra Database (ver. 5.8), [Online]. Available: `https://physics.nist.gov/asd` [10/30/2020]. National Institute of Standards and Technology, Gaithersburg, MD. 2020. DOI: 10.18434/T4W30F.

[166] Safronova, M. S. *private communication*.